JOHANNES KEPLER
UNIVERSITY LINZ

Screening of the electrocatalytic activity of novel metal-organic frameworks (MOFs) towards carbon dioxide and oxygen reduction

Submitted by

Dominik Böhm, BSc

Submitted at

Institute of Physical Chemistry and Linz Institute for Organic Solar Cells (LIOS)

Supervisor

o. Univ. Prof. Niyazi Serdar Sariciftci

Co-Supervisor

DI Elisabeth Leeb

June 2024

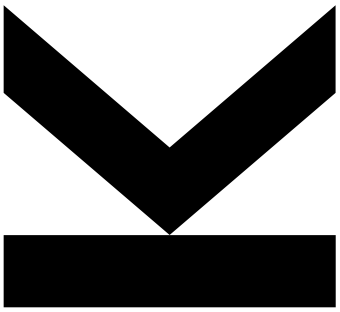

Master thesis

to obtain the academic degree of

Diplom-Ingenieur

in the Master's program

Chemistry and Chemical Technology

JOHANNES KEPLER UNIVERSITY LINZ

Altenberger Straße 69

4040 Linz

Austria

Statutory declaration

I hereby declare that the thesis submitted is my own unaided work, that I have not used other than the sources indicated and that all direct and indirect sources are acknowledged as references.

Tünelkam, 16.06.2024	
Date and place	Signature

Abstract

Electrocatalytic techniques for the activation of small, thermodynamically stable molecules, like carbon dioxide, oxygen, water or nitrogen exhibit increasing interest in the scientific community. These techniques are envisioned for integration into future energy conversion and storage systems. Electrochemical utilisation of carbon dioxide could provide carbon feedstock for chemical industry, thus decoupling it from its dependence on fossil resources. Current research focuses on developing suitable electrocatalysts for these purposes. Here, metal-organic frameworks could offer a unique possibility as platforms to perform electrochemical reactions, owing their inherent porosity and large surface area.

This thesis reports the successful synthesis of a nickel(II)-glyoximate-linker and its corresponding metal-organic frameworks. Among the 21 prepared metal-organic frameworks, 19 are a novelty to literature. The electrocatalytic activities of these metal-organic frameworks were evaluated for carbon dioxide and oxygen reduction reactions. Several metal-organic frameworks exhibited promising performance. Additionally, a novel electrochemical deposition method for metal-organic framework was developed. The electrodeposited films were subjected to electrochemical impedance spectroscopy measurements.

Exzerpt

Elektrokatalytische Technologien zur Aktivierung kleiner, thermodynamisch stabiler Moleküle wie Kohlendioxid, Sauerstoff, Wasser oder Stickstoff erfreuen sich zunehmender Beliebtheit unter Wissenschaftlern. Mögliche Einsatzgebiete umfassen beispielsweise zukünftige Energiespeichersysteme. Das elektrochemische Recycling von Kohlendioxid könnte als Kohlenstoffquelle für die chemische Industrie dienen und sie so von ihrer Abhängigkeit von fossilen Ressourcen entkoppeln. Die aktuelle Forschung konzentriert sich auf die Entwicklung geeigneter Elektrokatalysatoren für diese Zwecke. Metallorganische Gerüstverbindungen könnten sich aufgrund ihrer inhärenten Porosität und großen inneren Oberfläche als geeignete Materialklasse zur Durchführung dieser elektrochemischen Reaktionen erweisen.

Diese Arbeit beschreibt die Synthese eines Nickel(II)-Glyoximat-Linkers und davon abgeleiteter metallorganischer Gerüstverbindungen. Von den 21 hergestellten Gerüstverbindungen, sind 19 bislang nicht in der Literatur beschrieben worden. Die elektrokatalytischen Aktivitäten dieser metallorganischen Gerüstverbindungen wurden für Kohlendioxid- und Sauerstoffreduktionsreaktionen untersucht. Mehrere metallorganische Gerüstverbindungen zeigten vielversprechende elektrokatalytische Aktivitäten. Darüber hinaus wurde eine neuartige elektrochemische Abscheidungsmethode für metallorganische Gerüstverbindungen entwickelt. Die elektrochemisch abgeschiedenen Filme wurden Impedanzspektroskopiemessungen unterzogen.

Acknowledgements

First and foremost, I would like to express my deepest gratitude to o.Univ.-Prof. Niyazi Serdar Sariciftci for his unwavering support, motivation and encouragement throughout my research. Thank you, for offering me the opportunity to work in the laboratory and provide the necessary materials and scientific instruments.

I am deeply thankful to my co-supervisor DI Elisabeth Leeb. Your continuous guidance throughout this project and your inputs regarding hands-on experience in the lab were invaluable. You always had an open ear in case I faced difficulties during my practical work. Thank you for this great support!

A special thanks is due to Prof. Heinz Langhals and Dr. Christoph Ulbricht for the fruitful discussions on organic syntheses.

Furthermore, I want to thank Assoz. Prof. Uwe Monkowius for providing me access to the Corey UV-Vis spectrophotometer to conduct spectroelectrochemical measurements.

I want to especially thank Birgit Paulik for always helping me with administrative concerns and bureaucratic paperwork.

I am profoundly grateful to my friends and dear institute members for their camaraderie and support. You always stood by me and supported me, thank you all!

Lastly, I want to thank my parents and my brother for their unconditional support and love. Thank you for everything!

Contents

1

Objective

The objective of this thesis is to explore the potential of novel metal-organic frameworks (MOFs) as electrocatalysts for the carbon dioxide as well as oxygen reduction reaction. Electrocatalysis is crucial for the development of sustainable energy solutions and the reduction of greenhouse gas emissions. By facilitating the reduction reactions of carbon dioxide and oxygen, electrocatalysis can help in the production of renewable fuels and chemicals, thereby minimising our reliance on fossil fuels. Furthermore, electrocatalysis may serve as a technique to decrease atmospheric concentrations of greenhouse gases, like carbon dioxide.

Why are MOFs considered a promising material class for electrocatalysis? MOFs are composed of metal ions coordinated to organic ligands, forming crystalline, nanoporous networks. These pores provide extensive surface areas, making MOFs highly suitable for electrocatalytic applications. The increased surface area enhances the accessibility of active sites, promoting more efficient interactions between reactants and the catalyst, thereby improving current density and overall catalytic performance. However, MOFs are typically insulating materials, which poses a challenge for efficient charge transport from the electrode through the MOF to the reactants. To address this issue, electrically conductive MOFs are required which are based on advanced organic ligand systems.

2

Introduction

One of the foremost challenges confronting humanity in the 21st century is climate change [1–3]. This phenomenon is primarily attributed to anthropogenic emissions of greenhouse gases, with carbon dioxide being the most significant contributor [4–6]. The burning of fossil fuels is the major factor responsible for the steady increase in atmospheric greenhouse gas concentrations [2]. Historically, the extensive utilisation of fossil fuels as energy sources commenced with the Industrial Revolution [7,8]. Since then, their consumption continuously increased [2]. Presently, coal, crude oil and natural gas remain crucial not only as primary energy sources for electricity generation but also as fuels for transportation and as raw materials for the chemical industry (*e.g.* polymers, lubricants, pharmaceuticals, dyestuff) [9].

A reduction of fossil fuel consumption to counteract global warming is inevitably connected with the search for alternative energy sources. The expansion of renewable energy sources may compensate for fossil fuels in generating electricity [10]. However, renewable energy sources have a major drawback. They are inherently fluctuating sources of energy, meaning the generated electricity output is not constant and varies over time due to factors beyond direct human control [11,12]. To ensure a stable and reliable energy supply from renewable sources, electricity storage units are required. During periods of high generation, *i.e.* high solar irradiance and strong wind conditions, these units could store excess electricity and release it again during times of low generation or high demand. Thus, electricity storage units prevent sudden supply disruptions in national grids. Additionally, they reduce the need for peaking power plants [13].

The concept of large-scale electricity storage has a long history that predates beyond the upturn of renewable energy. For instance, the world's first pumped hydroelectric energy storage facility was commissioned in Switzerland already in 1907 [14]. Advanced storage techniques include rechargeable battery systems [15–17] or supercapacitors [17,18]. Another promising approach is offered by electrocatalysis. Here, electricity storage would be facilitated by the conversion of electrical energy into chemical energy *via* electrolysis. This stored chemical energy could be converted back into electricity *via* fuel cells, if required. In current technical literature, this concept is commonly referred to as *energy conversion and storage* [17,19]. Presently, research in this field is focussing on the access of abundant, small and thermodynamically stable molecules, like water,

oxygen or carbon dioxide. Electrocatalytic water splitting could supply green hydrogen [20] whereas the idea behind electrochemical oxygen reduction is the generation of hydrogen peroxide [21].

Besides their utilisation to store electricity as chemical energy, these energy-rich products gained from electrolysis could also serve as renewable feedstock for chemical industry. Green hydrogen may provide an alternative to fossil fuels in high-temperature industrial processes such as steelmaking [22] or cement production [23]. Hydrogen peroxide could serve as a green oxidising agent for pulp and paper bleaching as well as textile and wastewater treatment [24]. Electrocatalysis is not necessarily restricted to access hydrogen or hydrogen peroxide. For example, electrocatalytic nitrogen fixation could produce ammonia or urea, which are necessary feedstock for fertilisers [25]. Much attention is devoted to the electrocatalytic carbon dioxide reduction which could address two issues simultaneously. Firstly, this technique offers a possibility to capture and convert carbon dioxide into useful products, combating climate change. Secondly, the supply of chemical industry with carbon feedstock could be decoupled from fossil resources [26]. Hydrogen or hydrocarbons produced *via* electrocatalytic routes could also serve as synthetic fuels ("e-fuels") for the transportation sector [27]. All these strategies are summarised in **Figure 1**.

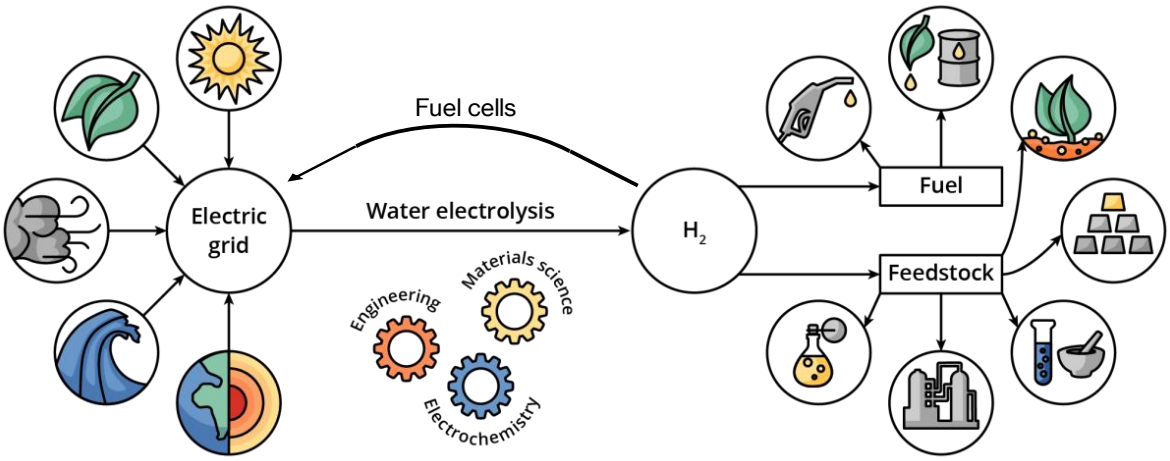

Figure 1. Overview of the strategies for energy conversion and storage systems using the example of water electrolysis to obtain green hydrogen. Taken and adapted from ref. [28].

2.1. Electrocatalysis

As outlined, electrocatalysis could evolve as an important tool to combat global warming. Like all forms of catalysis, electrocatalysis enhances the rate of a reaction under investigation by lowering its activation energy barrier. Electrocatalysis specifically involves reactions at the interface between an electrode and the electrolyte where electron transfer occurs [29,30]. The field of electrocatalysis may be differentiated into heterogeneous and homogeneous electrocatalysis. In the case of heterogeneous electrocatalysis, the electrode itself or a surface modification on the

electrode represents the catalytically active species. The catalyst and the reactants are not located in the same phase [31,32]. Contrary, in homogeneous electrocatalysis, the electrode just functions as a donor or acceptor of electrons. The catalyst is a redox active species dissolved in the electrolyte causing the conversion of the reactant through a redox reaction. To reach its initial redox state again, the catalyst is re-oxidised or re-reduced in the vicinity of the electrode. Consequently, these redox active species function as electron shuttles between the electrode and the reactant. Typical homogeneous electrocatalysts are organometallic compounds or various other metal-complexes [32,33]. Industrially, heterogeneous electrocatalysis is of much more relevance owing the ease of catalyst separation [32]. Consequently, energy conversion and storage systems should be developed following the design principles of heterogeneous electrocatalysis to reach marketability [34].

The design of electrocatalysts is dictated by three performance indicators, namely activity, selectivity and stability. A catalysts activity is a measure of the rate with which it accelerates a chemical reaction. Selectivity, on the other hand, refers to the ability of the electrocatalyst to favour the formation of a specific product over others in reactions that have multiple possible outcomes. Stability characterises the property of the catalyst to maintain its activity under operating conditions over prolonged periods of time [32]. The selectivity of an electrocatalyst may be assessed by qualitative determination and quantification of its products generated during electrolysis experiments. Similarly, the stability may be assessed by optical inspection of the electrode whilst performing cyclic voltammetry or electrolysis. If the electrocatalytic film is disintegrating or delaminating from the electrode during electrolysis, the electrocatalyst is not stable. During cyclic voltammetry, a stable electrocatalyst should exhibit consistent peak currents and peak potentials as well as reproducible shapes. Furthermore, a stable electrocatalyst will show a constant current trace in chronoamperometric electrolysis experiments, indicating sustained catalytic activity over time under operational conditions [29,35]. The determination of the activity of an electrocatalyst shall be outlined in the next chapter.

At a first glance it may seem counterintuitive, but a catalysts selectivity as well as its stability are more important than its activity [32]. Up to now, major restrictions of the implementation of novel electrocatalysts for energy conversion and storage systems are to be attributed to their lack of stability and selectivity under application-related industrial conditions. Both properties crucially affect the efficiency, cost-effectiveness and practical applicability of electrocatalysts. This lack of stability causes a quick drop in their activity, resulting in a lower productivity than predicted from laboratory experiments. On a log run, it is better to use a less active but nevertheless stable catalyst, because less investment is needed to maintain a certain threshold productivity. Stable catalysts provide consistent performance, which is essential for reliable operation. The economic implications of stability are significant, as reducing the frequency of catalyst replacement lowers operational costs and minimises downtime, enhancing the overall profitability of a process [32,36].

Owing the ever-growing requirements regarding the efficient use of resources, industry is craving for highly selective catalysts [32]. High selectivity is crucial for ensuring that the desired product is synthesised in high yields, which reduces the need for extensive purification processes. This not only simplifies the downstream processing but also improves the overall efficiency of the reaction, as less energy and resources are needed to isolate the desired product. A highly selective catalyst produces less byproducts, reducing the amount of waste generated and increasing the profitability of the process [32,36]. Selectivity poses a significant challenge in electrochemical carbon dioxide reduction due to the diverse array of potential products that can be generated, such as carbon monoxide, formate, alcohols and hydrocarbons, among others [29]. Consequently, both stability and selectivity of a catalyst are to be prioritised over its activity because these properties crucially affect the efficiency, cost-effectiveness and practical application of catalytic processes. If a catalyst lacks activity, the productivity of the whole plant may be easily increased by increasing the catalyst loading or the total electrode surface area, *i.e.* building more electrolysis baths. Therefore, a lack in activity may be counterbalanced by a scale-up of the chemical plant. Another possibility is provided by designing rough or porous electrodes [36,37]. Increasing the roughness or porosity of electrodes enhances the electroactive surface area, providing more active sites for electrochemical reactions. This directly boosts the catalytic activity by allowing more reactants to interact with the catalyst simultaneously, increasing the overall current and, consequently, the reaction rate [29,35]. Here, metal-organic frameworks offer unique possibilities in enhancing electroactive surface area as shall be explained in chapter 2.2.

One of the primary issues with current electrocatalyst development is the disproportionate emphasis on catalytic activity [36]. Researchers often prioritise discovering materials with exceptional catalytic performance, driven by the need to demonstrate significant improvements over existing technologies. However, this activity-centric approach often leads to the underestimation of stability and selectivity until later stages of development. This sequential approach – focusing first on activity and then on stability and selectivity – can be problematic for several reasons. Firstly, it can lead to significant delays and increased costs, as materials that show promise in terms of activity may later be found unsuitable due to poor stability or selectivity. Secondly, it can create a bias in research outputs, where high-activity materials are frequently reported, but fewer studies address improvements associated with stability and selectivity. The optimum technique for electrocatalyst development should adopt a more holistic and integrated approach from the outset. This involves simultaneous consideration of activity, stability and selectivity during the initial stages of research and development [36,37]. Additionally, computational methods and machine learning can play a crucial role in predicting and optimising the properties of electrocatalysts prior to experimental validation [36].

2.1.1. Assessment of electrocatalytic activity

Descriptive parameters are essential for reporting activities of novel electrocatalysts. Activity is dictated by the relationship between the driving force of an electrochemical reaction, the applied overpotential and the resulting reaction rate, manifested as current or current density response. The overpotential is the difference between the applied bias potential and the equilibrium potential. The general aim is to design electrocatalysts showing high activities, *i.e.* high current densities, at no or only low overpotentials [35]. So far, no uniform guidelines exist on reporting electrocatalytic activities. As a result, comparing electrocatalysts based on their reported performance parameters is challenging due to the differing standards employed by various research groups [36].

One parameter for reporting electrocatalytic activities is represented by the turnover frequency (TOF). The TOF indicates the number of reactant molecules converted to products per active site per unit time:

$$\text{TOF} = \frac{j_\eta}{z\Gamma F} \quad \textbf{(1)}$$

In **equation 1**, j_η, z, Γ and F represent the current density at a certain overpotential (η), the number of transferred electrons per turnover, the substance amount of active centres on the catalysts surface and the Faraday constant (96485 C mol^{-1}), respectively. TOF is particularly useful for comparing catalysts with varying active site densities or loadings [35]. Similarly to the TOF, the specific activity relates the kinetic current (i_k) to the geometric surface area (A) of the electrode, as shown in **equation 2**. The kinetic current is the current attributed to an electrochemical reaction at a certain overpotential, excluding contributions from mass-transfer limitations. It may be determined *via* the rotating disk electrode technique.

$$\text{Specific activity} = \frac{i_k}{A} \quad \textbf{(2)}$$

Reporting TOF as well as specific activity as performance parameters is problematic, because both are inherently dependent on the applied overpotential [35]. An ideal quantity to measure electrocatalytic activity is the exchange current density (j_0). It indicates the rate of electron transfer at equilibrium (zero overpotential) [29,35]. The current density-overpotential relationship is represented by the Butler-Volmer equation near equilibrium potential:

$$j = j_0 \left[\exp\left(\frac{\alpha_a z F \eta}{RT}\right) - \exp\left(\frac{\alpha_c z F \eta}{RT}\right)\right] \quad \textbf{(3)}$$

In **equation 3**, j, α_a or α_c, η, R and T describe the measured current density of the electrode, the anodic or cathodic charge transfer coefficients (note that $\alpha_a + \alpha_c = 1$), the overpotential, the universal gas constant (8.314 J K^{-1} mol^{-1}) and the absolute temperature. The Butler-Volmer equation describes the total current density as sum of the anodic and cathodic contributions. Near the equilibrium potential, *i.e.* at low overpotentials, the anodic as well as the cathodic current density contributions are almost balanced, resulting in no net current density. Consequently, the observed reaction is in equilibrium. Upon application of either an anodic or a cathodic overpotential, the respective exponential term gets dominant and a net current density may be measured, *i.e.* an electrochemical reaction occurs [29,35]. For overpotentials larger than ±120 mV, typically encountered in electrocatalysis, the Tafel-equation is applied to describe the current density-overpotential relationship (**equation 4**).

$$\ln(j) = \ln(j_0) - \frac{\alpha z F}{RT}\,\eta \qquad \textbf{(4)}$$

By plotting ln(j) *vs.* η, the exchange current density may be determined from the intercept of the graph [29]. Summarising, comparing the activities of electrocatalysts reported in the literature is challenging due to the use of diverse performance parameters. Besides the three performance parameters described above, numerous other activity indicators are reported throughout literature, *e.g.* the standard reaction rate constant. This makes it difficult to compare activities of different electrocatalysts.

2.2. Metal-organic frameworks

Metal-organic frameworks (MOFs) represent a class of organic-inorganic hybrid materials. As shown in **Figure 2 a**, they consist of two important building blocks: Metal ions or metal clusters, the so-called secondary building units (SBUs), and ligands, often termed linkers. As their name suggests, the linkers connect the individual metal clusters, thus forming extended coordination networks. Owing their chemical constitution, MOFs are therefore frequently categorised as coordination polymers, since they consist of discrete repeating units [38,39]. The linkers must possess at least two coordination sites per molecule, to be able to form coordinating structures. Depending on the type of linkers and metal clusters employed for MOF synthesis, one- (chain-coordination), two- (layered-coordination) or three-dimensional (cross-linked) networks are obtained [40]. The field that focuses on the synthesis and study of MOFs is known as *reticular chemistry*. This term is derived from the Latin word *reticulum*, meaning "net" or "network". Reticular chemistry is dedicated to the rational design and construction of coordination networks, to create materials with tailored properties for various applications [41].

The first MOF ever to be reported was MOF-5, discovered by O. M. Yaghi and coworkers in 1999 [42]. MOF-5 consists of zinc ions and terephthalic acid as metal ions and linkers, respectively [42,43]. An illustration of the structure of MOF-5 is depicted in **Figure 2 b**. This illustration highlights one important property of MOFs. They are nanoporous materials comprised of a high surface area [41]. The yellow sphere in **Figure 2 b** is representing one pore. The unique porous structure of MOFs is a key reason why researchers in the field of electrocatalysis are interested in this material class. The pores in MOFs, typically ranging between 10 to 20 nm in size, provide ideal platforms for conducting electrocatalytic experiments [39]. Small reactants, such as carbon dioxide or oxygen, can easily penetrate these pores and undergo reactions inside the pores when a potential is applied. Unfavourably, most MOFs are insulators and thus unsuited as electrocatalysts [44]. Research on electrically conductive MOFs is targeting this issue.

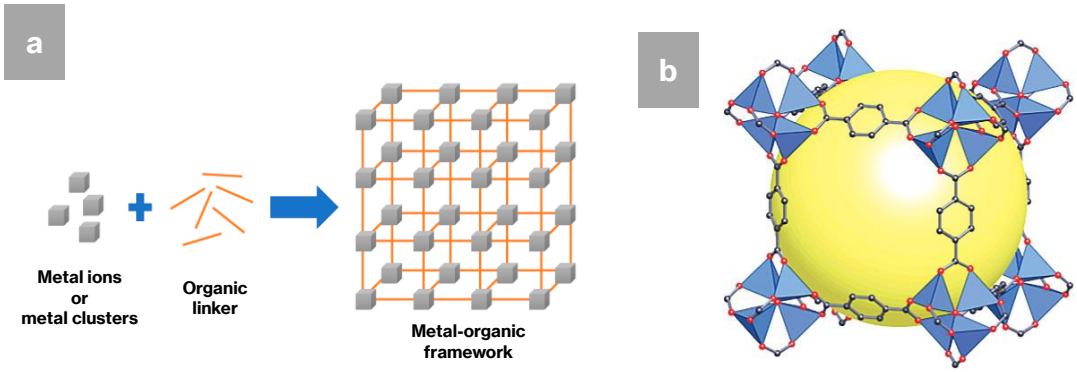

Figure 2. a) General structure of MOFs, which are composed of metal clusters connected *via* linkers. Taken from ref. [45]. **b)** Structure of MOF-5, the yellow sphere indicates one pore of the MOF. The blue tetrahedra and grey benzene moieties represent the zinc(II) clusters and the terephthalic acid linkers, respectively. Taken and adapted from ref. [43].

2.2.1. Electrically conductive metal-organic frameworks

A recent and rapidly expanding area of reticular chemistry focuses on the development of electrically conductive metal-organic frameworks (cMOFs). Most MOFs are insulators, which may be attributed to their chemical composition. Typically, MOFs feature carboxylate linkers and high-valency metal clusters, resulting in interactions between hard Lewis bases and hard Lewis acids. These interactions do not promote charge transport, because of the localised electronic states within the ionic bonds [44]. To address this, strategies for designing cMOFs include the use of linkers with soft Lewis bases, such as hydroxy, amino, or mercapto groups. They would provide better orbital overlap with soft metal clusters, thereby reducing band gaps [46]. Another approach involves the incorporation of redox-active linkers facilitating charge transport through space [44]. Despite these efforts, the conductivities of cMOFs generally remain within the range of 10^{-4} to 10^{-3} S cm^{-1}, with only a few exceptions [44,46,47]. Notably, in 2015, a copper(II) MOF linked by benzenehexathiol was reported to exhibit a benchmark conductivity of 1580 S cm^{-1}, a record that remains unsurpassed to this day [48].

cMOFs are particularly suitable for electrocatalysis due to their unique combination of electrical conductivity and high porosity. The intrinsic electrical conductivity of these MOFs facilitates efficient electron transfer to and from the active sites, thereby improving the efficiency and kinetics of the catalytic reactions. Additionally, the high porosity of MOFs significantly boosts their electrocatalytic activity. The porous nature of MOFs provides a large electrochemical surface area, offering numerous active sites for the electrochemical reactions to occur. This extensive surface area enhances the interaction between the reactants and the catalyst, leading to higher reaction rates. The pores also facilitate the diffusion of reactants and products to and from the active sites, reducing mass-transfer limitations and further enhancing catalytic efficiency. Furthermore, the modular design of MOFs enables the integration of various catalytic components within a single framework. This can include multiple metal sites or co-catalysts that work synergistically to improve overall performance. For instance, bimetallic MOFs can combine the properties of different metals to achieve superior catalytic activity and stability compared to monometallic systems [44,47,49].

This thesis investigated MOFs based on a tetrathiafulvalene-analogous linker system, as shall be explained in the following paragraphs. In a recent study, a tetrathiafulvalene-based linker (tetrathiafulvalene-tetrabenzoic acid, linker **A**, **Figure 3**) was incorporated into an indium(III)-MOF [50]. MOFs comprising linker **A** are known to exhibit electrical conductivity due to the π-π stacking propensities of the tetrathiafulvalene-unit. The synthesised indium(III)-MOFs showed promising electrocatalytic activity towards carbon dioxide reduction. Interestingly, replacing linker **A** with its inorganic analogue bis(dithiolene dibenzoic acid)nickel(II) (linker **B**, **Figure 3**), boosted faradaic efficiency, peak current density as well as selectivity towards formate production. The authors attributed this increase in performance to the bimetallic nature of the indium(III)-MOF based on linker **B** [50].

The synthesis of another linker, isostructural to linker **A**, was published by S. Ott and coworkers. They prepared a cobaloxim-linker (bis(dibenzoic acid glyoximato)cobalt(III), linker **C**, **Figure 3**) and the derived zirconium(IV)-MOF. This MOF showed superior electrocatalytic performance towards the hydrogen evolution reaction [51].

In 2020, the research group of M. Dincă first reported the synthesis and successful implementation of a nickel(II) glyoximate-linker (bis(dibenzoic acid glyoximato)nickel(II), linker **D**, **Figure 3**) for the preparation of the respective zinc(II)-, manganese(II)- and cadmium(II)-MOFs. Their motivation was to show that isoreticular linker substitution of linker **A** with the isostructural linker **D** would yield MOFs exhibiting comparable electrical conductivities. Indeed, the conductivities

between the linker **A**- and linker **D**-based MOFs differed by only two orders of magnitude, emphasising the powerful concepts of reticular chemistry for isostructural linker design [i] [53].

Despite the known electrocatalytic activity of MOFs based on the three isoreticular linkers **A**, **B** and **C**, no comparable studies have been conducted for MOFs utilising linker **D**. Furthermore, only three MOFs based on linker **D** are reported in literature [53], although the scope of MOF-synthesis may be readily expanded to include other SBUs. Hence, the primary objective of this thesis was the synthesis of bimetallic MOFs comprising linker **D** and a proof-of-concept that these MOFs exhibit a potential electrocatalytic activity towards the carbon dioxide (CO_2RR) as well as oxygen reduction reaction (ORR). A total of 21 MOFs were successfully prepared and subjected to electrocatalytic screening. Owing the chemical nature of linker **D**, incorporating a nickel(II) centre, mixed-metal MOFs were synthesised through variation of the SBUs. This allowed for tuning the catalytic properties of the MOFs. Additionally, attempts were made to synthesise other linkers; however, these attempts were not yet successful and require further investigation, as outlined in the following chapters.

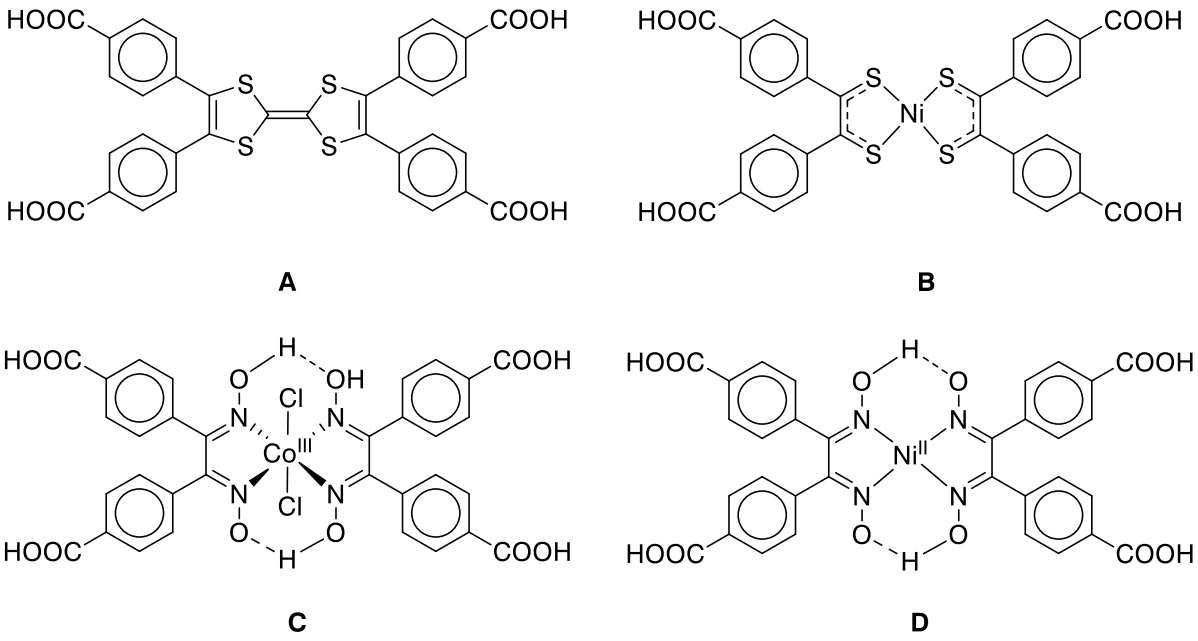

Figure 3. Chemical structures of tetrathiafulvalene or tetrathiafulvalene-analogous linkers. **a)** tetrathiafulvalene-tetrabenzoic acid, linker **A**; **b)** bis(dithiolene dibenzoic acid)nickel(II), linker **B**; **c)** bis(dibenzoic acid glyoximato)cobalt(III), linker **C**; **d)** bis(dibenzoic acid glyoximato)nickel(II), linker **D**, the primary objective of this thesis.

[i] The conductivities of the cadmium MOFs based on linkers **A** and **D** were reported to be $2.9 \cdot 10^{-4}$ S cm^{-1} [52] and $2.7 \cdot 10^{-6}$ [53], respectively.

3

Experimental

The experimental chapter is structured as follows: Initially, an overview of the chemicals and reagents used in this study is provided. Then, the spectroscopic techniques employed for the characterisation of the synthesised compounds are presented. Next, the individual synthesis protocols are explained in detail. The chapter concludes with a description of the electrochemical techniques utilised. All reagents and chemicals used within this study are listed in **Table 1**, They were applied without any further purification.

Table 1. Summary of the chemicals and materials utilised to perform the experiments presented in this thesis. This table is continued on the next pages.

Chemical / reagent	Supplier	Purity
Ammonium nitrate	Sigma-Aldrich	≥98 %
Acetic acid (glacial)	Merck	100 %
Aluminium chloride	Aldrich	99 %
Ammonium sulphate	Fluka	99.0 %
Barium nitrate	Sigma-Aldrich	99+%
Bismuth(III) nitrate pentahydrate	Sigma-Aldrich	98 %
Boric acid	Alfa Aesar	99.99 %
Calcium chloride	Roth	≥98 %
Chloroform	VWR	99.0 - 99.4 %
Cobalt(II) bromide	Alfa Aesar	97 %
Cobalt(II) chloride	Honeywell	≥98.0 %
Cobalt(II) nitrate hexahydrate	Sigma-Aldrich	98+%
Copper(II) acetate monohydrate	Thermo Scientific	98+%
Copper(II) sulphate pentahydrate	Sigma-Aldrich	99.0 %
Deuterium oxide (99.9 atom % D)	Sigma-Aldrich	/
Deuterochloroform (99.80 atom % D)	Eurisotop	/
Deuterodimethyl sulfoxide (99.9 atom % D)	Sigma-Aldrich	/
Diethyl ether	Riedel-de Haen	≥99.8 %
Dimethyl sulfoxide	VWR	100.0 %

Continuation of **Table 1**.

Chemical / reagent	Supplier	Purity
Dimethylformamide	VWR	100.0 %
DL-Tartaric acid	Thermo Scientific	99.5 %
Erbium(III) oxide	Aldrich	99.9 %
Ethanol	Sigma-Aldrich	absolute p. A.
Ethyl acetate	VWR	99.8 %
Europium(III) chloride hexahydrate	Aldrich	99.9 %
Ferrocene	Aldrich	98 %
Hydrobromic acid (48 %)	Thermo Scientific	/
Hydroxylamine (50 wt. % in water)	Sigma-Aldrich	/
Hydroxylamine hydrochloride	Sigma-Aldrich	99 %
Indium chloride	Aldrich	99.999 %
Iodine	Sigma-Aldrich	99.8 %
Iron(II) sulphate heptahydrate	Thermo Scientific	99.5 %
Isopropanol	VWR	100.0 %
Lead(II) acetate trihydrate	/	/
Magnesium chloride	Sigma-Aldrich	99.0 - 102.0 %
Manganese(II) sulphate monohydrate	Sigma-Aldrich	98+%
Methanol	VWR	100.0 %
Methyl 4-formyl benzoate	Sigma-Aldrich	for synthesis
Methylene chloride	Chem-Lab	99.8+%
Nafion (solution in alcohols)	Aldrich	/
Neodymiun(III) chloride hexahydrate	Aldrich	99.9 %
Nickel(II) acetate tetrahydrate	Thermo Scientific	99+%
Nickel(II) chloride hexahydrate	Alfa Aesar	99.95 %
Nitric acid (65 %)	VWR	69.3 %
n-Pentane	Roth	≥99 %
p-Benzoquinone	Thermo Scientific	98+%
Phosphorous pentasulfide	Sigma-Aldrich	99 %
p-Nitrophenylboronic acid	Alfa Aesar	95 %
Potassium cyanide	Sigma-Aldrich	≥98.0 %
Potassium hexacyanoferrate(II) trihydrate	Merck	p. A.
Pyridine	Sigma-Aldrich	≥99.9 %
Sea sand for column chromatography	Fisher Sientific	/
Silica (Geduran Si 60) for column chromatography	Merck	/
Sodium carbonate	Fluka	≥99.5 %
Sodium dihydrogenphosphate	Sigma-Aldrich	≥99.0 %
Sodium hydrogenphosphate	Sigma	≥99.0 %
Sodium hydroxide	Merck	p. A.
Sodium tungstate dihydrate	Fluka	≥99 %

Continuation of **Table 1**.

Chemical / reagent	Supplier	Purity
Strontium nitrate	Sigma-Aldrich	≥99.0 %
Sulphuric acid (95-97 %)	Sigma-Aldrich	/
Tetrabutylammonium tetrafluoroborate	Fluka	purum
Tetrahydrofurane	VWR	100.0 %
Tin(II) chloride dihydrate	Acros Organics	98+%
Toluene	VWR	100.0 %
Vanadium(IV) oxide sulfate hydrate	Sigma-Aldrich	97 %
Veratraldehyde	Fluka	≥98 %
Ytterbium(III) chloride hexahydrate	Aldrich	99.9 %
Zinc nitrate hexahydrate	Aldrich	98 %

3.1. Spectroscopic characterisation

3.1.1. ^{1}H-NMR spectroscopy

^{1}H-NMR spectra were recorded on a 300 MHz FT-NMR spectrometer (Bruker, Advance III) at 298 K. All spectra were referenced to the respective solvent signals. 32 spectra were averaged for data acquisition.

3.1.2. FT-IR spectroscopy

Infrared spectra were acquired using an FT-IR spectrometer (Bruker, Vertex 80) in the attenuated total reflectance (ATR)-mode under nitrogen atmosphere. Background correction was performed from the nitrogen atmosphere within the measurement chamber. Data were recorded from 4000 to 500 cm^{-1} by averaging 256 spectra with a resolution of 2 cm^{-1}. ATR operates by directing an IR beam into an ATR crystal at an angle that causes total internal reflection. This creates an evanescent wave that extends a few micrometres beyond the crystal surface. When a sample is placed in contact with the crystal, the evanescent wave penetrates the sample. The sample absorbs some of the IR radiation at specific wavelengths, depending on its molecular composition. The reflected radiation, now containing absorption information, is detected and analysed by means of Fourier transformation to yield an IR spectrum. The experimental setup of an ATR-unit is schematically illustrated in **Figure 4**.

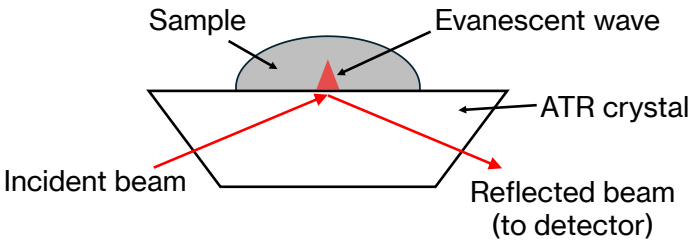

Figure 4. Illustration of the ATR-mode working principle.

3.1.3. UV-Vis spectroscopy

UV-Vis measurements were conducted on a double-beam UV-Vis spectrophotometer (Perkin Elmer, UV-Vis-NIR Lambda 1050) using quartz glass cuvettes (Hellma, 111-QS) with a thickness of 10 mm. Background correction was performed without cuvettes in the beam path. Data was collected from 350 to 700 nm (1000 nm for **8**) at increments of 2 nm. Transmittance (*T*) was converted into absorbance (*A*) according to **equation 5**, as recommended by IUPAC guidelines [54].

$$A = -\log_{10}(T) \qquad \textbf{(5)}$$

3.2. Synthesis of linkers and MOFs

All syntheses were performed under ambient atmosphere, unless otherwise stated.

3.2.1. Synthesis of 4,4'-benzoindicarboxylic acid dimethyl ester (2)

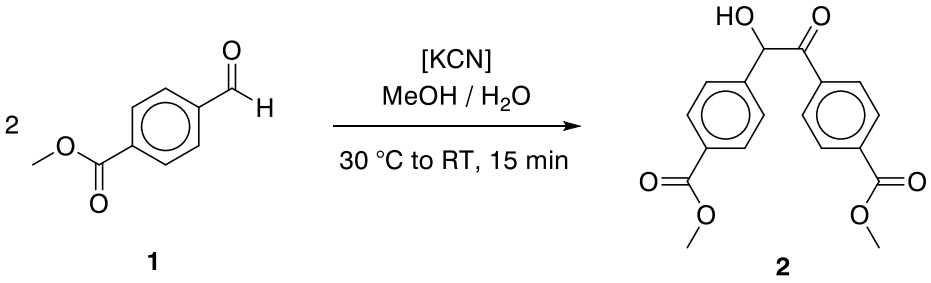

Scheme 1. Synthesis of **2** *via* benzoin condensation of **1**.

Following procedure [53], a 250 mL high-form beaker, charged with methyl 4-formyl-benzoate (**1**, 16.42 g, 100 mmol) and methanol (70 mL), was placed in a lukewarm water bath to dissolve the reactant under stirring. The resulting colourless, clear solution was diluted with water (18 mL) and removed from the water bath. Prior to the subsequent step, it is recommended to assess the temperature of the reaction solution to range between 28 and 32 °C to maximise the yield of the benzoin condensation. Next, solid potassium cyanide (1.954 g, 30 mmol) was added as

a catalyst apace to the vigorously stirred reaction solution. Immediately, the solution turned yellow, indicating the induction of the reaction. Within the following minute, the colour strength intensified from orange to bright red and wine red. After one to two minutes, the salmon-coloured crude product precipitated from the deeply red coloured solution, forcing the stir bar to halt. To complete the benzoin condensation, the suspension was stirred manually with a glass rod for further 13 minutes. The reaction mixture was diluted with water (100 mL) and filtered *via* a Buchner funnel. The crude product was washed with water (12 × 100 mL) and recrystallised from methanol (approximately 320 mL [ii]). After cooling to room temperature, the product was isolated by filtration, washed with methanol (2 × 50 mL) and dried at 80 °C *in vacuo* overnight.

Yield: 73 – 81 % (11.98 – 13.30 g, 36.5 – 40.5 mmol) of 4,4'-benzoindicarboxylic acid dimethyl ester (**2**), bright white solid, odourless [iii].

^{1}H-NMR (300 MHz, $CDCl_3$, 298 K, δ in ppm): δ = 8.05 (d, J = 8.64 Hz, 2 H, Ar-**H**), 7.98 (d, J = 8.43 Hz, 2 H, Ar-**H**), 7.92 (d, J = 8.64 Hz, 2 H, Ar-**H**), 7.40 (d, J = 8.31 Hz, 2 H, Ar-**H**), 6.01 (d, J = 4.65 Hz, 1 H, HCO**H**), 4.52 (d, J = 5.49 Hz, 1 H, **H**COH), 3.91 (s, 3H, -COOC**H**$_3$), 3.87 (s, 3H, -COOC**H**$_3$).

FT-IR (ATR, ν in cm^{-1}): ν = 3462, 3005, 2955, 1720, 1678, 1611, 1572, 1504, 1439, 1406, 1275, 1186, 1096, 1018, 964, 881, 814, 766, 719, 613, 536.

UV-Vis (CH_2Cl_2): No signal.

[ii] Towards the end of the recrystallisation, complete dissolution of the crude product proceeds slowly such that further methanol shall be added only in small amounts of maximum 10 mL at intervals of approximately one to two minutes. Thereby, methanol consumption is minimised and the overall yield of the reaction increased.

[iii] An aldehyde or almond odour indicates trace impurities of reactants that can be removed by prolonged drying in the vacuum oven.

3.2.2. Synthesis of 4,4'-benzildicarboxylic acid dimethyl ester (3)

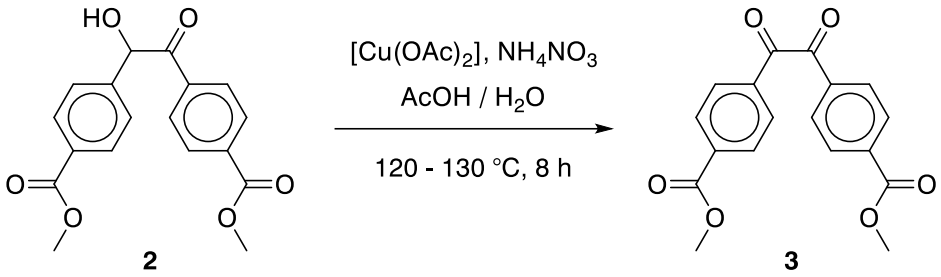

Scheme 2. Synthesis of **3** from catalytic oxidation of **2**.

According to literature [55], a 100 mL round-bottom flask was charged with **2** (12.00 g, 36.5 mmol [iv]), copper(II) acetate monohydrate (0.12 g, 0.6 mmol), ammonium nitrate (5.99 g, 74.8 mmol) and aqueous acetic acid (42 mL, 80 vol-% in water). The mixture was gently heated for 15 to 20 minutes at 120 to 130 °C to dissolve **2** in boiling aqueous acetic acid. Once the benzoin was dissolved, the resulting bright green reaction solution was refluxed under intense stirring for eight hours [v]. Afterwards, the reaction mixture was cooled to room temperature and filtered *via* a Buchner funnel. The collected product was washed thrice with little amounts of each water, methanol as well as diethyl ether and dried at 80 °C *in vacuo* overnight.

Yield: 92 – 97 % (10.97 – 11.57 g, 33.6 – 35.5 mmol) of 4,4'-benzildicarboxylic acid dimethyl ester (**3**), canary yellow needles, fluorescent under UV-light (365 nm), odourless.

^{1}H-NMR (300 MHz, $CDCl_3$, 298 K, δ in ppm): δ = 8.18 (d, J = 8.64 Hz, 4H, Ar-**H**), 8.04 (d, J = 8.67 Hz, 4H, Ar-**H**), 3.96 (s, 6H, -COOC**H**$_3$).

FT-IR (ATR, ν in cm^{-1}): ν = 2964, 1719, 1663, 1570, 1501, 1435, 1406, 1279, 1188, 1101, 1014, 950, 890, 860, 782, 730, 685, 629, 533.

UV-Vis (CH_2Cl_2, λ in nm): $\lambda_{abs,\,max}$ = 398.

[iv] For a successful reaction, the benzoin must be thoroughly dried.

[v] Prolonged reaction times considerably decrease the yield of the oxidation below 80 %.

3.2.3. Synthesis of 4,4'-benzildicarboxylic acid (4)

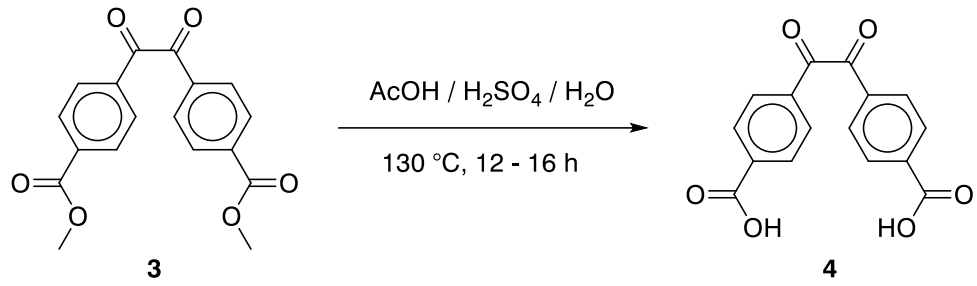

Scheme 3. Acidic deesterification of **3** to afford **4**.

Following [56], a 250 mL round-bottom flask was charged with **3** (3.00 g, 9.2 mmol) and glacial acetic acid (110 mL). Under vigorous stirring, an aqueous solution of sulphuric acid (50 mL, 20 vol-% in water) was added at room temperature over a time course of ten minutes. The resulting yellow suspension was stirred at 130 °C for 12 to 16 hours [vi]. After cooling to room temperature, water (40 mL) was added and the yellow reaction mixture was filtered *via* a sintered glass funnel (POR-4). The product was washed with water until the filtrate was pH-neutral by lackmus and dried at 80 °C *in vacuo* overnight.

Yield: 97 – 99 % (2.66 – 2.71 g, 8.9 – 9.1 mmol) of 4,4'-benzildicarboxylic acid (**4**), pale-yellow solid, not fluorescent under UV-light (365 nm), odourless.

^{1}H-NMR (300 MHz, DMSO-d_6, 298 K, δ in ppm): δ = 13.51 (br. s, ~2 H, -COO**H**), 8.15 (d, J = 8.61 Hz, 4 H, Ar-**H**), 8.07 (d, J = 8.61 Hz, 4 H, Ar-**H**).

FT-IR (ATR, ν in cm^{-1}): ν = 3200 to 2500, 3061, 2822, 2669, 2550, 1688, 1665, 1568, 1504, 1425, 1296, 1202, 1119, 1015, 930, 889, 860, 814, 781, 731, 702, 521.

UV-Vis (DMSO, λ in nm): $\lambda_{abs,\,max}$ = 392.

[vi] The synthesised product is voluminous and may cause the stirrer to halt. If this event occurs, no urgent actions are required, the reaction can be proceeded without stirring.

3.2.4. Synthesis of dibenzoic acid glyoxime (5)

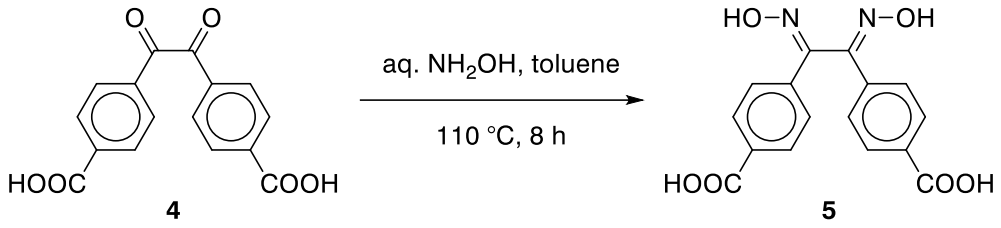

Scheme 4. Synthesis of **5** from oximation of **4**.

Following literature procedure [53], a 250 mL round-bottom flask was charged with **4** (2.00 g, 6.7 mmol), toluene (100 mL) and aqueous hydroxylamine (3.3 mL, 50 wt-% in water, 53.9 mmol, 8 eq.). The resulting yellow suspension was refluxed at 110 °C for eight hours [vii]. Toluene was removed *in vacuo* and the yellow-white residue was suspended in methanol (100 mL). The suspension was sonicated for 40 minutes and filtered *via* a sintered glass funnel (POR-4). Without washing, the residue was stirred in aqueous acetic acid (200 mL, 10 vol-% in water) at 110 °C for 30 minutes. After cooling to room temperature, the white suspension was filtered *via* a sintered glass funnel (POR-4) and the residue was washed with water (4 × 30 mL) as well as methanol (2 × 10 mL). The product was dried at 80 °C *in vacuo* overnight.

Yield: 57 – 65 % (1.25 – 1.43 g, 3.8 – 4.4 mmol) of dibenzoic acid glyoxime (**5**), white powder, odourless.

^{1}H-NMR (300 MHz, DMSO-d_6, 298 K, δ in ppm): δ = 12.99 (br. s, ~2 H, -COO**H**), 11.74 (s, 2 H, =N-O**H**), 7.99 (d, J = 8.43 Hz, 4 H, Ar-**H**), 7.49 (d, J = 8.43 Hz, 4 H, Ar-**H**).

FT-IR (ATR, ν in cm^{-1}): ν = 3300 to 2500, 3277, 3103, 2799, 2621, 2502, 1684, 1612, 1506, 1385, 1261, 1123, 999, 893, 845, 806, 766, 687, 569, 525.

UV-Vis (DMSO): No signal.

[vii] During the first ten minutes of the reaction, the pale-yellow reactant is converted into a creamy white precipitate that adheres to the inner wall of the reaction flask.

3.2.5. Synthesis of bis(dibenzoic acid glyoximato)nickel(II) tetrasodium salt (6)

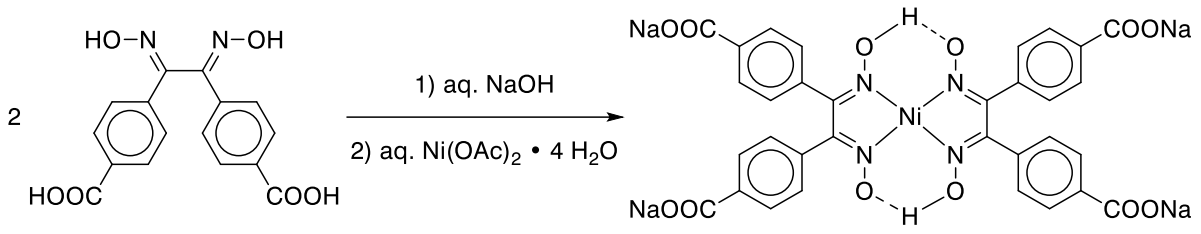

5 **6**

Scheme 5. Complexation of **5** to yield **6**.

In analogy to [53], an aqueous sodium hydroxide solution (60 mL, 0.1 M, 6.00 mmol) in a 500 mL round-bottom flask was purged with nitrogen for 30 minutes [viii]. Therein, solid **5** (0.66 g, 2.01 mmol, 2 eq.) was dissolved under stirring. Complexation was performed by rapid addition of a solution of nickel(II) acetate tetrahydrate (0.25 g, 1.00 mmol, 1 eq.) in water (2 mL) [ix], yielding a deeply red coloured mixture that was heated at 60 °C for one hour. Then, isopropanol (240 mL) was slowly poured into the flask to precipitate the complex. Stirring was continued at 60 °C for another hour before the suspension was allowed to cool to approximately 30 °C. The suspension was filtered *via* a sintered glass funnel (POR-4) and the isolated complex was washed with isopropanol (3 × 15 mL) as well as methylene chloride (2 × 10 mL). The product was dried at 80 °C *in vacuo* overnight.

Yield: 97 – 99 % (0.78 – 0.80 g, 0.98 – 1.00 mmol) of bis(dibenzoic acid glyoximato)nickel(II) tetrasodium salt (**6**), fir green solid that rapidly turns fiery red upon exposure to atmosphere, probably due to formation of a hydrated species, odourless.

^{1}H-NMR (300 MHz, D_2O, 298 K, δ in ppm): δ = 7.61 (d, J = 7.98 Hz, 8 H, Ar-**H**), 7.13 (d, J = 7.83 Hz, 8 H, Ar-**H**).

FT-IR (ATR, ν in cm^{-1}): ν = 3600 to 2600, 3630, 3288, 1589, 1543, 1391, 1294, 1132, 912, 841, 779, 706, 667, 584.

UV-Vis (H_2O, λ in nm): $\lambda_{abs,\,max}$ = 404.

[viii] Purging with nitrogen is being continued until the very end of the synthesis, when the product complex is being filtered off, to prevent formation of nickel oxyhydroxide.

[ix] The vial containing the nickel(II) acetate solution was washed with little water.

3.2.6. Synthesis of bis(dibenzoic acid glyoximato)nickel(II) (7)

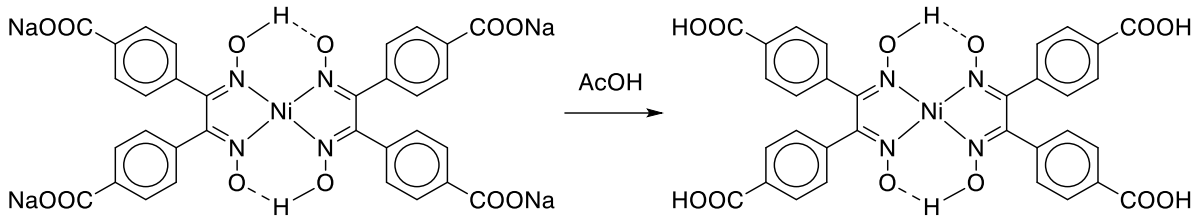

6 **7**

Scheme 6. Synthesis of linker **7** *via* protonation of **6**.

Following literature [53], **6** (0.40 g, 0.50 mmol) was distributed equally between two centrifuge tubes and suspended in glacial acetic acid (7.5 mL per vial). The red suspension was sonicated for 15 minutes, centrifuged and the supernatant was removed. Sonication in glacial acetic acid was repeated thrice. Afterwards, the protonated complex was washed with methylene chloride (4 × 7.5 mL per vial). The residue was suspended in little methylene chloride and transferred into a small beaker. Methylene chloride was allowed to evaporate at room temperature prior to drying the product at 80 °C *in vacuo* overnight.

Yield: 85 – 89 % (0.30 – 0.32 g, 0.42 – 0.44 mmol) of bis(dibenzoic acid glyoximato)-nickel(II) (**7**), orange-red solid with metallic luster, odourless.

^{1}H-NMR (300 MHz, DMSO-d_6, 298 K, δ in ppm): δ = 13.14 (br. s, ~4 H, -COO**H**), 11.74 (s, ~1 H, μ-**H**), 7.82 (d, J = 7.68 Hz, 8 H, Ar-**H**), 7.28 (d, J = 7.62 Hz, 8 H, Ar-**H**).

FT-IR (ATR, ν in cm^{-1}): ν = 3400 to 2400, 2993, 2671, 2544, 1734, 1697, 1609, 1570, 1526, 1404, 1290, 1096, 908, 860, 775, 754, 635, 542.

UV-Vis (DMF, λ in nm): $\lambda_{abs,\,max}$ = 410.

3.2.7. Synthesis of bis(dithiolene dibenzoic acid dimethyl ester)nickel(II) (8)

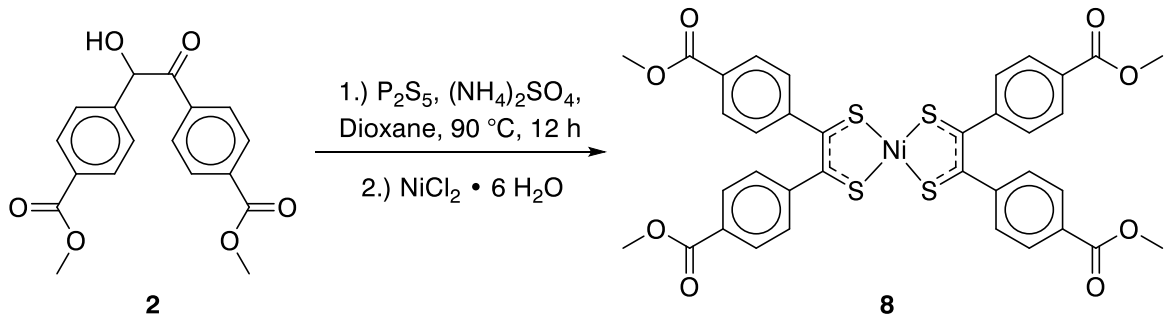

2 **8**

Scheme 7. Synthesis of **8** by a two-step complexation starting from **2**.

According to a modified procedure [57], a 50 mL round-bottom flask was charged with **2** (1.00 g, 3.05 mmol), phosphorous pentasulphide (0.68 g, 3.06 mmol), ammonium sulphate (0.15 g, 1.14 mmol) and dioxane (15 mL). The mixture was refluxed at 90 °C for twelve hours. After cooling to room temperature, a solution of nickel(II) chloride hexahydrate (0.36 g, 1.51 mmol) in ethanol (1 mL) was added to the yellow-orange reaction mixture, whereby a colour change to dark green occurred. The reaction mixture was stirred at 80 °C for further two hours, cooled to room temperature, diluted with chloroform (10 mL) and washed thrice with water (5 mL) [x]. The organic phase was dried over anhydrous calcium chloride, filtered and concentrated on a rotary evaporator to yield a viscous, green oil. Purification was afforded *via* column chromatography with a pentane-methylene chloride (1:1) eluent. First, a yellow impurity of unpleasant odour eluted whereupon the eluent was changed to a pentane-methylene chloride-methanol (5:5:1) mixture. The eluting dark green-black fraction was collected and concentrated to afford the product, which was dried at 80 °C *in vacuo* overnight.

Yield: 11 % (0.13 g, 0.17 mmol) of bis(dithiolene dibenzoic acid dimethyl ester)nickel(II) (**8**), dark green to black solid, odourless.

^{1}H-NMR (300 MHz, $CDCl_3$, 298 K, δ in ppm): δ = 7.94 (d, J = 8.10 Hz, 8 H, Ar-**H**), 7.41 (d, J = 8.10 Hz, 8 H, Ar-**H**), 3.93 (s, 12 H, -COOC**H**$_3$).

FT-IR (ATR, ν in cm^{-1}): ν = 2949, 1717, 1602, 1503, 1433, 1357, 1268, 1190, 1137, 1099, 1016, 962, 883, 762, 700.

UV-Vis (CH_2Cl_2, λ in nm): $\lambda_{abs,\,max}$ = 594, 844 (br.).

[x] It is recommended to employ a flashlight to observe the phase boundary during the washing step.

3.2.8. Synthesis of veratroin (11)

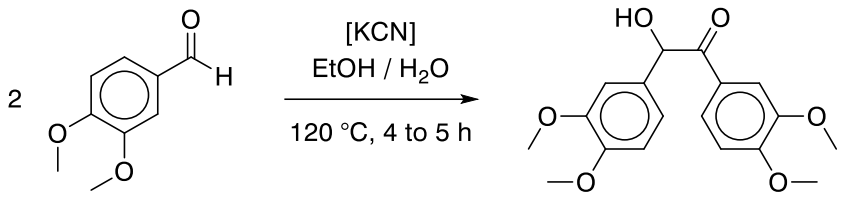

10 **11**

Scheme 8. Benzoin condensation of **10** to afford **11**.

In analogy to [58], a 250 mL round-bottom flask was charged with veratraldehyde (**10**, 30.02 g, 181 mol), potassium cyanide (7.51 g, 115 mmol), ethanol (50 mL) and water (50 mL). The reactants were dissolved by gentle heating on an oil bath under stirring. The resulting colourless solution was refluxed at 120 °C for four to five hours. After cooling to room temperature, the amber coloured solution was extracted thrice with chloroform (á 20 mL). The combined organic phases were washed with water (3 × 15 mL) [xi], dried over anhydrous calcium chloride, filtered and concentrated on a rotary evaporator. Prior to the next synthesis step, the crude product was not purified.

Yield: Crude veratroin (**11**, approximately 37 g), amber coloured, highly viscous liquid, contaminated with cyanide as evident by the strong almond smell.

Neither ^{1}H-NMR-, FT-IR- nor UV-Vis-spectra were recorded.

3.2.9. Synthesis of veratril (12)

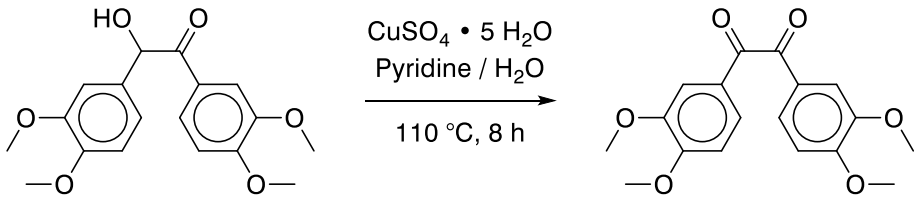

11 **12**

Scheme 9. Synthesis of **12** by oxidation of **11**.

[xi] If the phase separation during the washing step proceeds slowly, a small amount of water may be injected rapidly into the upper phase of the separating funnel. Thereby, the white foam decomposes faster into two phases. The application of a saturated brine solution instead of pure water for the washing step has not proven advantageously.

Following [58,59], a 500 mL round-bottom flask was charged with crude **11** (approximately 37 g) and copper(II) sulphate pentahydrate (80.00 g, 320 mmol) [xii]. Pyridine (150 mL) and water (150 mL) were added and the resulting dark blue solution was refluxed at 110 °C under stirring for eight hours. After cooling to room temperature, the reaction solution was diluted with water (150 mL), causing the precipitation of a yellow solid. The suspension was filtered *via* a sintered glass funnel (POR-3) and the isolated solid was washed with water [xiii], isopropanol (4 × 40 mL), methanol (3 × 30 mL) and diethyl ether (2 × 30 mL). Contrary to the reported procedures [58,59], claiming the product is sufficiently purified after washing, impurities were observed in the ^{1}H-NMR. Following a series of experiments, recrystallisation from ethyl acetate has proven most effective to purify the crude product (approximately 250 mL ethyl acetate per gram of crude product). The recrystallised product was dried at 80 °C *in vacuo* overnight.

Yield: 35 – 41 % (10.44 – 12.23 g, 31.6 – 37.0 mmol) of veratril (**12**) [xiv], pale yellow solid, small needle-shaped crystals, odourless.

^{1}H-NMR (300 MHz, $CDCl_3$, 298 K, δ in ppm): δ = 7.60 (d, J = 1.95 Hz, 2 H, Ar-**H**), 7.48 (dd, J_1 = 8.37 Hz, J_2 = 1.98 Hz, 2 H, Ar-**H**), 6.88 (d, J = 8.43 Hz, 2 H, Ar-**H**), 3.95 (two merged s, 12 H, -OC**H**$_3$).

FT-IR (ATR, ν in cm^{-1}): ν = 3018, 2936, 1651, 1582, 1510, 1449, 1416, 1352, 1265, 1229, 1138, 1011m 972, 870, 789, 721, 638, 575.

UV-Vis (CH_2Cl_2): No signal.

3.2.10. Attempted synthesis of 3,3',4,4'-tetrahydroxybenzil (13)

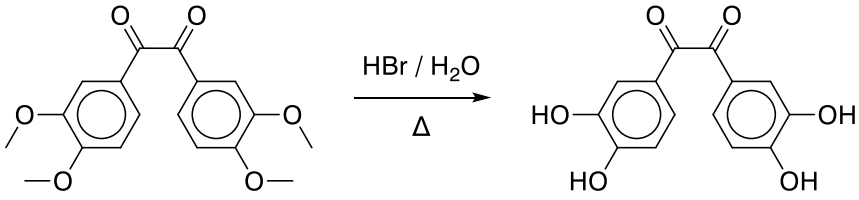

12 **13**

Scheme 10. Attempted synthesis of **13** by acidic deetherification of **12**.

[xii] In a set of separate experiments, the oxidation of crude **11** was conducted with a catalytic amount of copper(II) acetate monohydrate in analogy to the synthesis of **3**. However, even with stoichiometric amounts of copper(II) acetate monohydrate far inferior yields were obtained. Therefore, the excessive amounts of copper(II) sulphate pentahydrate were necessary.

[xiii] The crude product was washed with water until all traces of blue copper(II) sulphate were removed, yielding a yellow solid.

[xiv] The yield was referred to the substance amount of **10**.

In analogy to [58,59], **12** (0.50 g, 1.5 mmol, 1 eq.) was suspended in hydrobromic acid (8.6 mL, 48 wt-% in water, 76.0 mmol, 50 eq.) and glacial acetic acid (8.6 mL). The mixture was refluxed for defined time periods, cooled to room temperature and concentrated to approximately half of the original volume. Water (30 mL) was added and the mixture was stored at 0 °C for 24 hours. If precipitation occurred, the resulting yellow solid was filtered *via* a sintered glass funnel (POR-4), washed with little ice water and dried at 80 °C *in vacuo* overnight.

3.2.11. Preparation of MOFs based on linker D

MOFs were prepared following a standard solvothermal protocol. The respective amounts of metal salts (for masses consult **Table 2**, 84.0 µmol, 4 eq.) were dissolved in DMF (4 mL) and glacial acetic acid (18 µL) in 15 mL vials. Thereto, solutions containing **7** (15.0 mg, 21.0 µmol, 1 eq.) in DMF (500 µL) were added. To ensure quantitative transfer, the flask containing **7** was rinsed twice with DMF (250 µL). The vials were sealed and heated at 80 °C for 120 hours. After centrifuging the resulting suspensions, the residues were washed five times with DMF (2.5 mL), once with methylene chloride (2.5 mL) and twice with diethyl ether (2.5 mL). The collected MOFs were dried at 80 °C *in vacuo* overnight. Throughout this thesis, the MOFs will be denoted using the following nomenclature, **X-7**, where **X** represents the respective secondary building unit (metal) and **7** the linker **D**.

Table 2. Summarised amounts of the respective metal salts utilised for MOF synthesis, corresponding to substance amounts of 84.0 µmol.

Metal salt	$m_{\text{metal salt}}$ **/ mg**	**Metal salt**	$m_{\text{metal salt}}$ **/ mg**
$AgNO_3$	14.3	$InCl_3$	18.6
$AlCl_3$	11.2	$MgCl_2 \cdot 6\ H_2O$	17.1
$Ba(NO_3)_2$	22.0	$MnSO_4 \cdot H_2O$	14.2
$Bi(NO_3)_3 \cdot 5\ H_2O$	40.8	$NdCl_3 \cdot 6\ H_2O$	30.2
$CaCl_2$	9.3	$Ni(OAc)_2 \cdot 4\ H_2O$	20.9
$Co(NO_3)_2 \cdot 6\ H_2O$	24.5	$Pb(OAc)_2 \cdot 3\ H_2O$	31.9
CuCl	8.3	$SnCl_2$	16.0
$Cu(OAc)_2 \cdot H_2O$	16.8	$Sr(NO_3)_2$	17.8
$EuCl_3 \cdot 6\ H_2O$	30.8	$VOSO_4 \cdot 5\ H_2O$	21.3
$FeSO_4 \cdot 7\ H_2O$	23.4	$YbCl_3 \cdot 6\ H_2O$	32.6
$FeCl_3$ [xv]	13.6	$Zn(NO_3)_2 \cdot 6\ H_2O$	25.0

[xv] With iron(III) chloride, no MOF precipitated in the vial, even after a prolonged reaction time of additional 120 hours.

3.3. Electrochemical characterisation

3.3.1. Preparation of GC working electrodes for electrocatalytic activity tests

Commercial glassy carbon (GC) disk electrodes (PalmSens, ItalSens, diameter of 3 mm) were polished with a figure-eight motion on a polishing pad covered with alumina paste (Buehler, MicroPolish, particle size of 1.0 µm) for 30 seconds. Suspensions of the respective MOFs (1 mg) were prepared in ethanol (250 µL) and Nafion (50 µL, 5 wt-% in alkanes/alcohols) was added as a binder. Prior to drop casting, the suspensions were sonicated for 30 minutes. Then, 35 µL of the MOF-containing suspensions were drop cast onto the polished GC disk electrodes obtaining a catalyst loading of 1.65 mg cm^{-2}. The electrodes were allowed to dry in air for 30 minutes prior to electrochemical measurements.

3.3.2. CV study of the electrocatalytic activity of the prepared MOFs

The electrocatalytic activity of the prepared MOFs was studied using cyclic voltammetry (CV) and a standard three-electrode setup with a potentiostat (Ivium, V01218) controlled *via* a computer interface. As working (WE), counter (CE) and reference (RE) electrodes, the MOF-coated GC disk electrode, a platinum electrode as well as a Ag/AgCl (3 M KCl) electrode were applied, respectively. The platinum CE was cleaned flaming with a Bunsen burner until red glow. All experiments were conducted in 15 mL glass vials filled with a borate buffer of pH 8.5 [xvi] as electrolyte. The WE and CE were located in the same compartment. The measurement setup is depicted in **Figure 5**. Depending on the type of experiment, the electrolyte was purged with either nitrogen (for measurements under inert atmosphere), oxygen (for ORR experiments) or carbon dioxide [xvii] (for CO_2RR experiments). Then, three voltammograms were recorded from -1.2 to +1.0 V *vs.* SHE at scan rates of 20 mV s^{-1} without stirring at room temperature. All measurements were started at a potential of 0.0 V *vs.* SHE and an oxidative scanning direction. During CV measurements, the head space above the electrolyte was continued to be purged with inert gas or reactant gas. Data was not corrected for I•R compensation ("Ohmic drop") of the applied potential.

[xvi] For the preparation of the borate buffer, boric acid (3.09 g, 100 mM) and sodium hydroxide (0.50 g, 25 mM) were dissolved in 500 mL of 18 MΩ water. If necessary, the pH of the buffer was adjusted to 8.5 using sulphuric acid (1 M).

[xvii] The pH of the borate buffer was shifted to 6.2 upon purging with carbon dioxide for 30 minutes.

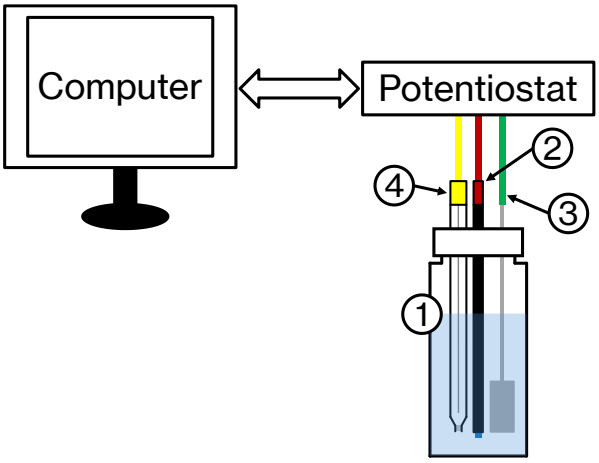

Figure 5. Schematic representation of the three-electrode setup utilised for CV measurements. The setup consisted of an electrolytic cell filled with a borate buffer of pH 8.5 (1), a GC disk WE with the drop cast MOF film (2), a platinum CE (3) and a Ag/AgCl (3 M KCl) RE (4).

3.3.3. Electrolysis experiments for ORR and hydrogen peroxide quantification

Electrolysis experiments were conducted in an H-cell with anode and cathode compartments separated by a Nafion 117 membrane. A borate buffer of pH 8.5 served as the electrolyte (45 mL were used as catholyte). The WE consisted of a GC plate electrode (total surface area of 4 cm^2), with 75 µL of MOF suspension (prepared as described in chapter 3.3.2., catalyst loading of 0.13 mg cm^{-2}) applied to each side. Both the WE and a Ag/AgCl (3 M KCl) RE were immersed in the catholyte, while a platinum CE was placed in the anode compartment. The catholyte was purged with oxygen for 30 minutes prior to electrolysis. Then, a potential of -0.4 V *vs.* SHE was applied for six hours. During the electrolysis, the catholyte was continued to be purged with oxygen. Samples of 200 µL were collected from the catholyte every hour for hydrogen peroxide quantification.

Hydrogen peroxide was quantified using a photometric method [60]. A carbonate buffer of pH 9.0 (150 mM sodium bicarbonate/sodium carbonate) and a *p*-nitrophenylboronic acid solution (4 mM in DMSO) were prepared. Equal volumes of both solutions were mixed and filtered through a syringe filter to yield the photometric reagent. 50 µL of the samples collected during electrolysis were mixed with 2 mL of the photometric reagent in a brown glass vial, which was then incubated in the dark for 30 minutes. During this period, the reaction depicted in **Scheme 11** occurred. While *p*-nitrophenylboronic acid absorbs in the UV region, the resulting *p*-nitrophenol shows an absorbance maximum at 411 nm. This shift in absorbance was utilised for photometric hydrogen peroxide quantification.

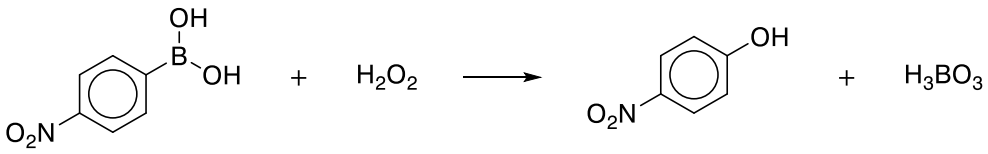

p-Nitrophenylboronic acid *p*-Nitrophenol

Scheme 11. Reaction utilised for photometric quantification of hydrogen peroxide. *p*-Nitrophenylboronic acid reacts in stoichiometric amounts with hydrogen peroxide, yielding *p*-nitrophenol. The accompanied shift of the absorbance maximum is harnessed for photometric quantification purposes.

Following the 30-minute incubation, three aliquots of 100 µL each were pipetted into microtitration plates. After an additional six minutes of light exposure, the absorbance of the samples was measured using a UV-Vis spectrophotometer (Thermo Fischer Multiskan Go Microplate Spectrophotometer). The absorbance data were used to calculate the amount of hydrogen peroxide. By integrating the current-time trace from chronoamperometry, the transferred charge was determined. **Equation 6** allowed to calculate the Faradaic efficiency from the substance amount of hydrogen peroxide ($n_{H_2O_2}$) and the transferred charge (Q) using z = 2.

$$\text{Faradaic efficiency} = \frac{zFn_{H_2O_2}}{Q} \quad \textbf{(6)}$$

3.3.4. Chronoamperometric deposition of Mn-7 and Zn-7 thin films on FTO substrates

Solutions of either zinc(II) nitrate hexahydrate (18.7 mg, 62.9 µmol, 6 eq.) or manganese(II) sulphate monohydrate (10.7 mg, 63.3 µmol, 6 eq.) in DMF (10 mL) and nitric acid (10 µL, 1 M) were prepared in a vial. Solid **7** (7.5 mg, 10.5 µmol, 1 eq.) was added and rapidly dissolved by means of shaking the vial. This MOF-precursor solution was added into a high-form vial containing *p*-benzoquinone (65 mg, 600 µmol) as well as tetrabutylammonium tetrafluoroborate (65 mg) as conducting salt and both solids were swiftly dissolved. A pre-assembled three-electrode setup was introduced into the electrolyte, consisting of a cleaned FTO substrate, a platinum electrode and a Ag/AgCl-coated silver wire as working, counter and quasi reference electrode, respectively. Prior to deposition, the Ag/AgCl quasi reference electrode was calibrated with ferrocene. Using a potentiostat (Ivium, V01218), negative potentials of -0.4 and -0.6 V *vs*. SHE were applied in the chronoamperometric mode each for 300 seconds. After deposition, the electrode was immersed in DMF for washing purposes and stored in DMF.

3.3.5. Spectroelectrochemical experiments with Mn-7- and Zn-7-thin films on FTO substrates

Spectroelectrochemical measurements were conducted on a UV-Vis spectrophotometer (Varian, Cary 50 Conc), whereby the FTO substrates were biased with a potentiostat (Ivium, V01218). Again, a three-electrode system was connected to the potentiostat using the **Mn-7**- and **Zn-7**-thin films on FTO substrates, a platinum wire and a Ag/AgCl wire as working, counter as well as reference electrode, respectively. The three-electrode system was placed in a spectroelectrochemical cuvette (path length of 10 mm, borosilicate glass) filled with a tetrabutylammonium tetrafluoroborate (60 mg) containing DMF (4 mL) electrolyte. The experimental setup is depicted in **Figure 6**. Measurements were conducted by applying increasingly cathodic potentials starting from +1.2 to -1.6 V *vs.* SHE in increments of 0.2 V in the chronoamperometric mode. Simultaneously, UV-Vis spectra were recorded at each potential step. During the measurement, care was taken that the electrodes did not touch each other to prevent short-circuiting of the system. Finally, the Ag/AgCl quasi reference electrode was calibrated with ferrocene.

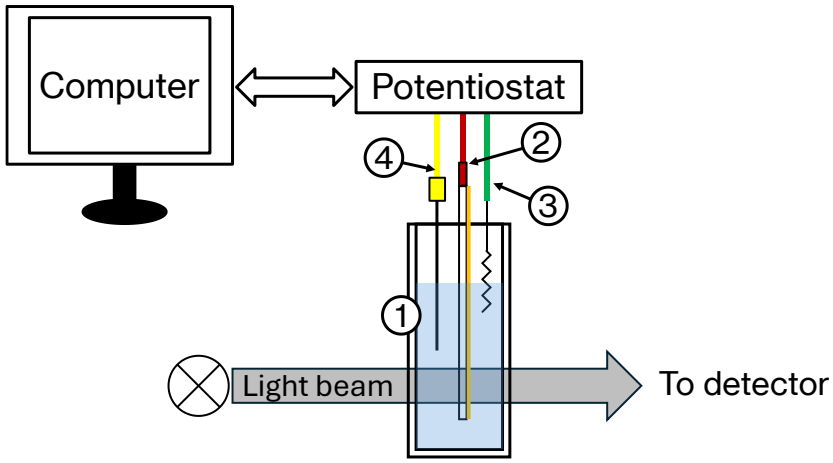

Figure 6. Schematic representation of the setup used for spectroelectrochemical measurements, showing the cuvette containing the electrolyte (1), the FTO substrate covered with MOF WE (2), the platinum CE (3) and the Ag/AgCl QRE.

3.3.6. Electrochemical impedance spectroscopy with Mn-7 and Zn-7 thin films on FTO substrates

To estimate the electrical conductivity of the prepared MOFs, EIS was performed with **Mn-7** and **Zn-7** thin films on FTO substrates. EIS measurements were conducted at the open circuit potential in a tetrabutylammonium tetrafluoroborate (60 mg) containing DMF (4 mL) electrolyte using a three-electrode setup (**Mn-7** or **Zn-7** on FTO as WE, Pt-CE and Ag/AgCl-QRE) connected to a potentiostat (Ivium, V01218). Data were recorded from 10^5 to 10^{-2} Hz.

4

Results and discussion

The results and discussion chapter adheres to the following structure: First, linker and MOF synthesis will be discussed, followed by the presentation of the results obtained during the electrocatalytic activity tests. This chapter will close with an explanation of the conductivity measurements of the MOFs. Synthesis will mainly focus on linker **D**, as outlined in the objectives. Besides linker **D**, attempts were initialised to synthesise linker **B** as well as a novel linker based on the dihydroxy analogue of linker **D**, called bis(di(benzene-3,3',4,4'-tetrahydroxy)-glyoximato)nickel(II) (linker **E**). The synthesis of linker **E** was motivated by the substitution of the carboxylate-groups of linker **D** with hydroxy-groups. The introduction of hydroxy-linkers (soft Lewis bases) should enhance the electrical conductivities of the resulting MOFs, as predicted by theory and outlined in the introduction. As shown in the fundamental reaction scheme (**Scheme 12**), the synthesis of linker **B** and **D** starts from a common reactant (methyl 4-formylbenzoate), whereas linker **E** is afforded from veratraldehyde. Owing difficulties encountered during synthesis, linker **D** was the only linker successfully afforded at the time this thesis was submitted.

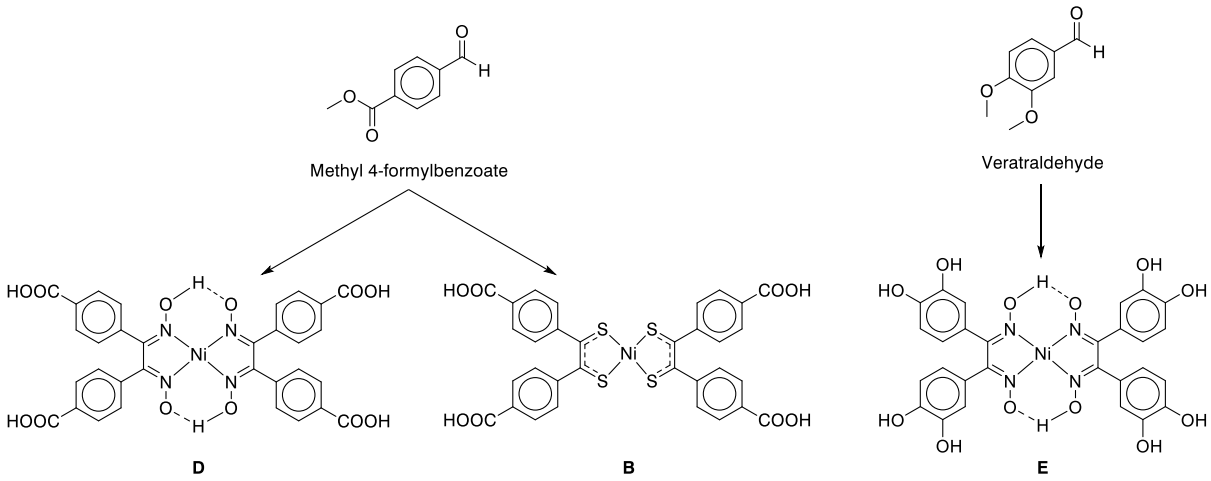

Scheme 12. Overview reaction scheme, indicating the reactants necessary to synthesise linkers **B**, **D** and **E**. The first two linkers originate from methyl 4-formylbenzoate, whereas the last is derived from veratraldehyde.

4.1. Synthesis and characterisation of linkers and MOFs

4.1.1. Synthesis of bis(dibenzoic acid glyoximato)nickel(II) (linker D)

Linker **D** was afforded by following a six-step synthesis route outlined in **Scheme 13**. Throughout the rest of this thesis, linker **D** will be denoted with the abbreviation **7**, due to its chronological order of being the seventh chemical structure in the synthesis sequence. Yields of each synthesis step exceeded typical literature values, resulting in an overall yield of 31 to 45 %, surpassing the 29 % reported previously [53]. Comprehensive synthetic procedures and references to literature protocols are elaborated in the experimental section, starting from page 20.

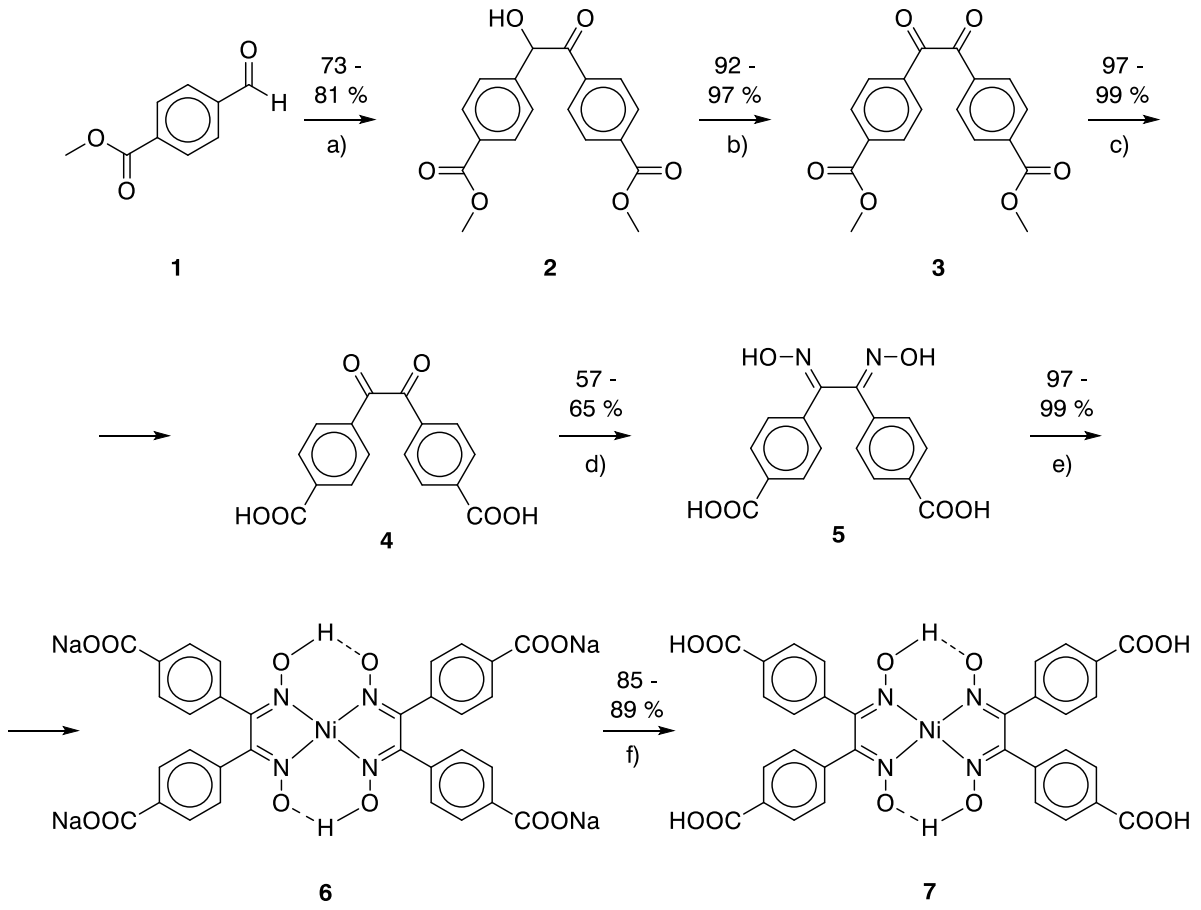

Scheme 13. Summarised reaction scheme for the synthesis of linker **7** from methyl 4-formylbenzoate (**1**). Numbers above reaction arrows indicate yields of the individual synthesis steps. Reaction conditions: **a)** KCN in catalytic amounts, $MeOH/H_2O$, RT; **b)** $Cu(OAc)_2$ in catalytic amounts, NH_4NO_3, $AcOH/H_2O$, reflux; **c)** $AcOH/H_2SO_4/H_2O$, reflux; **d)** NH_2OH, toluene, reflux; **e)** NaOH, then $Ni(OAc)_2 \cdot 4\ H_2O$; **f)** AcOH.

In the first synthesis step, benzoin condensation of methyl 4-formylbenzoate (**1**) with catalytic amounts of potassium cyanide afforded 4,4'-benzoindicarboxylic acid dimethyl ester (**2**). The benzoin condensation, often referred to as Liebig reaction, is regarded the first synthetic organocatalytic reaction discovered [61]. Despite the application of toxic potassium cyanide as a

catalyst [xviii], the ease with which the reaction is performed, makes it a valuable tool for C-C-bond formation. Opposite to the later discussed benzoin condensation of veratraldehyde, **1** required only mild reaction conditions (reaction temperature of 30 °C) and short reaction times. This finding may be attributed to the electron withdrawing ester group (R^1 = -$COOCH_3$, R^2 = -H) of **1** that stabilise the carbanion formed upon umpolung in the first step of the mechanism of the benzoin condensation as shown in **Scheme 14**. Contrary, the two *meta*- and *para*-positioned electron donating methoxy groups of veratraldehyde (R^1 = R^2 = -OCH_3) hinder the umpolung and destabilise the carbanionic intermediate necessary for the subsequent attack of a second aldehyde molecule [63]. Consequently, benzoin condensation of veratraldehyde required reflux conditions and prolonged reaction times.

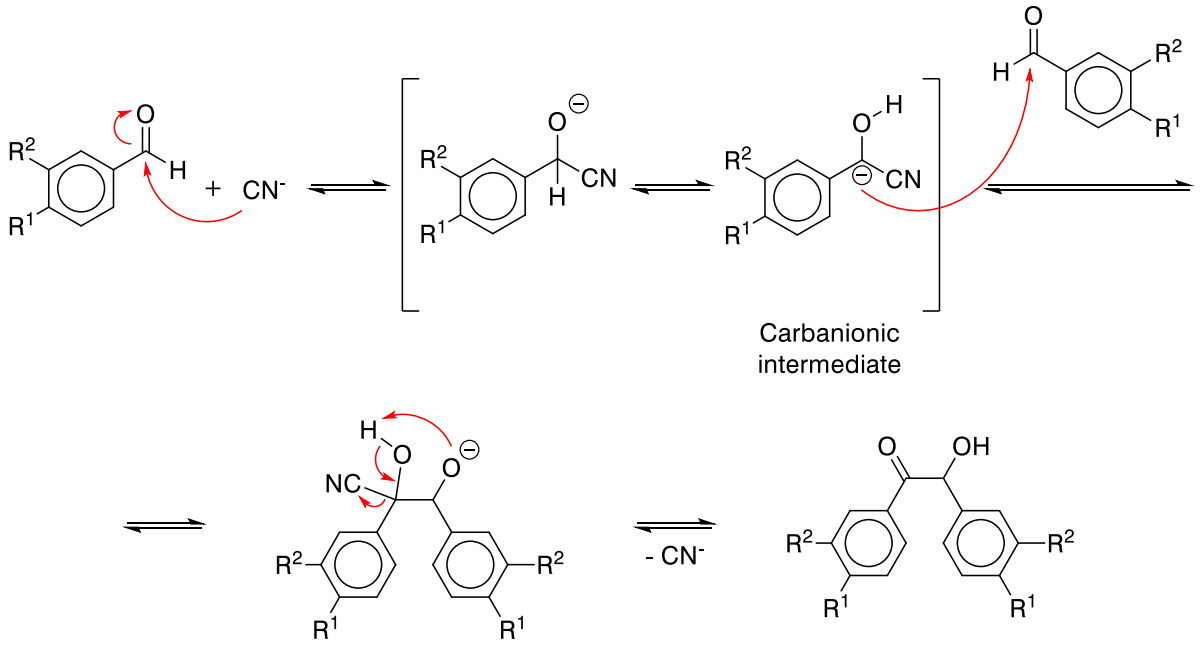

Scheme 14. Reaction mechanism for potassium cyanide-catalysed benzoin condensation of an aromatic aldehyde. The reaction rate is dictated by the stability of the carbanionic intermediate. Reactions proceeded fast at room temperature for methyl 4-formylbenzoate (R^1 = -$COOCH_3$, R^2 = -H). Slow reaction rates were observed in the case of veratraldehyde (R^1 = R^2 = -OCH_3), thus requiring reflux conditions, owing the electron donating methoxy substituents.

Next, **2** was oxidised *via* a copper-catalysed reaction under reflux conditions to yield 4,4'-benzildicarboxylic acid dimethyl ester (**3**). Thereby, the application of stoichiometric amounts of copper(II) oxidant is avoided as necessary in older literature [64,65]. In the mechanism of the catalysed reaction (**Scheme 15**), one molecule of **2** undergoes a single-electron transfer-type of oxidation by attack of two copper(II) ions, which in turn are reduced to copper(I) species. Due to

[xviii] Potassium cyanide may be replaced by non-toxic thiazolium salts, like the coenzyme thiamine [62], as a catalyst.

the presence of excess ammonium nitrate, reoxidation of copper(I) is afforded by reduction of nitrate to nitrite. Subsequently, nitrite and ammonium ions react in the acidic environment to afford dinitrogen. Evolution of gaseous dinitrogen is the driving force for this irreversible reaction, shifting the equilibrium towards the product side. **3** showed yellow-green fluorescence under UV light (365 nm) as depicted in **Figure 7 a**.

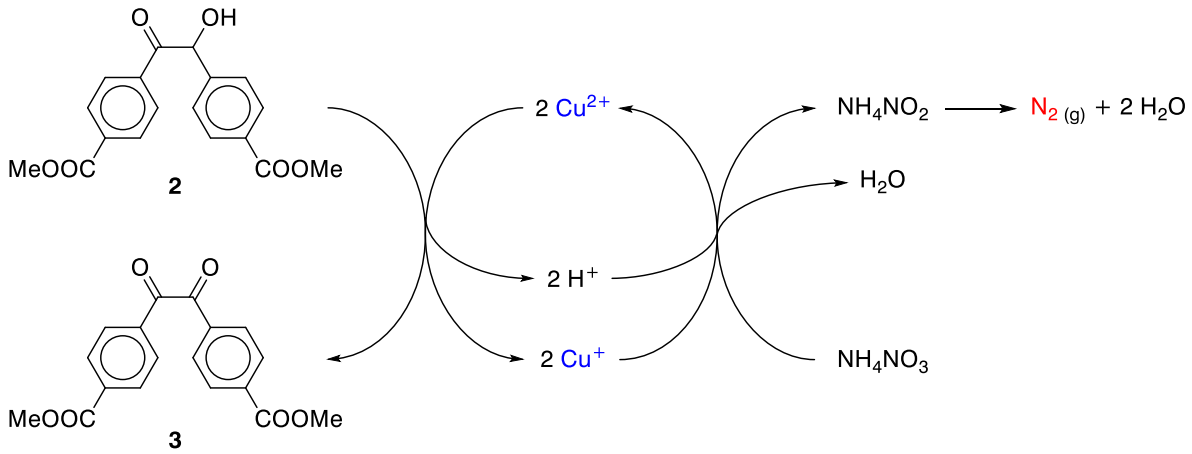

Scheme 15. Mechanism of the copper(II)-catalysed benzoin oxidation. The benzoin (**2**) undergoes single-electron-transfer-like oxidation to the benzil (**3**). Copper(I) species were re-oxidised by nitrate ions. Resulting nitrite ions reacted with ammonium ions to yield dinitrogen. Gas evolution of dinitrogen shifted the equilibrium of the overall reaction towards the product side.

Acidic deesterification of **3** afforded 4,4'-benzildicarboxylic acid (**4**). Deesterification must not be conducted under alkaline conditions, since **3** would undergo benzilic acid rearrangement [66]. Despite the possibility of (spectroscopic) characterisation, successful conversion of **3** to **4** may be assessed with a simple UV-lamp. Since, the carboxylic acid moieties of **4** quench the luminescence of **3**, the product of this reaction step must not show fluorescence (**Figure 7 b**).

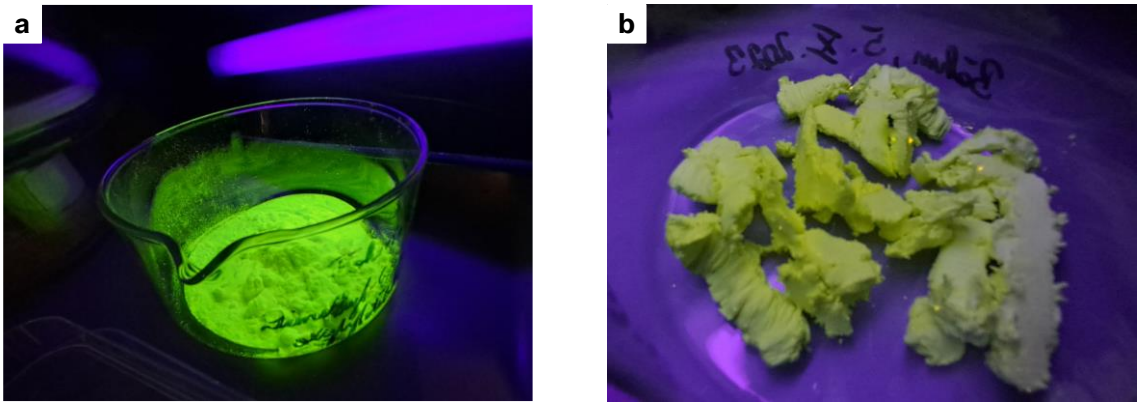

Figure 7. Photographic images of **a)** 4,4'-benzildicarboxylic acid dimethyl ester (**3**) and **b)** 4,4'-benzildicarboxylic acid (**4**) under UV irradiation.

Oximation of **4** to dibenzoic acid glyoxime (**5**) was first attempted with hydroxylamine hydrochloride (8 eq.) and sodium acetate (16 eq.) in toluene under reflux conditions for 14 hours. Working with hydroxylamine hydrochloride was preferred over the free base hydroxylamine due to it being a stable solid [67]. However, instead of a white powder, a greyish product was obtained showing a ^{1}H-NMR spectrum (recorded in DMSO-d_6) differing considerably from literature [51,53]. Attempts to afford **5** by varying the solvent (methanol, ethyl acetate), replacing sodium acetate by sodium hydroxide and shortening reaction times to ten and eight hours failed. Therefore, oximation was conducted with an aqueous hydroxylamine solution as described in literature [51,53], successfully yielding **5**.

Complexation of **5** with nickel(II) acetate monohydrate in an aqueous, alkaline solution afforded bis(dibenzoic acid glyoximato)nickel(II) tetrasodium salt (**6**), which was protonated in glacial acetic acid to finally yield the linker **7**. Unfortunately, **6** and **7** were not analysed by means of X-ray diffraction (XRD), to study their coordination geometry. In literature, both complexes are described to adopt a square-planar geometry, as predicted for d^8-metal complexes by the crystal field theory [68]. Since the glyoximate-ligands are medium to strong-field ligands according to the spectrochemical series [68], **6** and **7** are expected to adopt a square planar geometry in the low-spin configuration. ^{1}H-NMR spectra of **6** and **7** (**Figure 25** and **Figure 26**) support this finding, because they neither show peak broadening, atypical chemical shifts nor artefacts representative for paramagnetic complexes [69,70].

Reaction products **2** to **7** were characterised by means of optical appearance, ^{1}H-NMR, FT-IR and UV-Vis spectroscopy. Photographic images of **2** to **7** and the reactant **1** are depicted in **Figure 8 a**. ^{1}H-NMR as well as FT-IR spectra for each individual compound are presented in the appendix (**Figure 21** to **Figure 26**) and evaluated in the experimental section starting from page 20. Chemical shifts and integrals of the ^{1}H-NMR spectra were in accordance with previously published data for compounds **2** to **7** [51,53,71]. Unfortunately, no FT-IR data was provided by the authors of [51,53]. Consequently, vibrational peak assignment was conducted on the basis of IR spectra tables [72–74].

For a better comparison, the FT-IR spectra of **2** to **7** are summarised in **Figure 8 b**. The reaction progress of the six-step synthesis was followed by analysing the FT-IR spectra. The FT-IR spectrum of **2** contains a distinctive absorption band at 3462 cm^{-1} arising from the stretching mode of the hydroxyl group of the benzoin moiety [75]. The peaks at 3005 and 2955 cm^{-1} represent the stretching modes of the aromatic and methyl C-H bonds, respectively. Strong absorptions may be observed for the ester group from the stretching modes of the carbonyl group (1720 cm^{-1}) and the C-O bond (1275 and 1096 cm^{-1}). The stretching peak of the carbonyl group from the benzoin moiety may be observed at 1678 cm^{-1}, 42 cm^{-1} lower than the respective carbonyl peak of the ester. The absorption bands of aromatic ketones are typically shifted to lower wavenumbers, due to conjugation [76]. The spectrum of **2** served as reference points for subsequent transformations.

After the first synthetic step, **3** showed a disappearance of the hydroxyl band indicative for the formation of the benzil species. Additionally, the intensity of the absorption band at 1188 cm^{-1} increased notably. This band may be assigned to the C-C stretching mode of the benzil carbon backbone.

The deesterified product **4** exhibited a characteristic broad absorption band from 3200 to 2500 cm^{-1} as well as overtones and combination bands at 2822, 2669 and 2550 cm^{-1} originating from the hydroxyl stretching mode of the carboxylic acid. The absorption band of the carboxylic acid carbonyl group was shifted to a lower wavenumber (1688 cm^{-1}) and nearly completely merged with the band of the benzil carbonyl group. Furthermore, the C-O stretching mode of **3** just showed one single absorption band at 1296 cm^{-1}, again indicative for the successful deesterification.

Upon oximation, an additional band at 3277 cm^{-1} evolved, characteristic for the hydroxyl stretching mode of the oxime moiety. The carboxylic acid carbonyl stretching mode as well as the imine stretching mode merged to a peak at 1684 cm^{-1}. The peak at 999 cm^{-1} is originates from the N-O stretching mode of the oxime group.

Complexation and neutralisation of the carboxylic acid groups considerably changed the FT-IR spectrum. **6** showed a less pronounced absorption band from 3600 to 3000 cm^{-1} compared to **5**, because the band may be assigned solely to the stretching vibration of the bridged hydroxyl group of the oxime moiety. The contribution of the carboxylic acid groups disappeared. Consequently, the overtones and combination bands of the carboxylic acid also disappeared. A strong band appeared at 1391 cm^{-1} which can be attributed to the asymmetric stretching mode of the carboxylate.

The spectrum of the linker **7** again contained the hydroxyl stretching overtones from the carboxylic acid. The strong absorption at 1391 cm^{-1} disappeared, highlighting the successful protonation of **6**.

Figure 8 c depicts the solution UV-Vis absorbance spectra of compounds **2** to **7**, which coincide well with their observed colours. **2** and **5** did not show absorbance in the visible part of the spectrum and accordingly appeared as white solids. **3** and **4** exhibit absorbance maxima at 398 and 392 nm, respectively, whereby their absorbance bands are tailing off at 470 nm. Consequently, both substances were brightly yellow coloured. The absorbance maxima of the nickel(II) complexes **6** and **7** showed minor bathochromic shifts of 10 to 20 nm compared to compounds **3** and **4**. Additionally, their absorbance bands extended until 570 nm, causing the observed orange-red colour of both complexes.

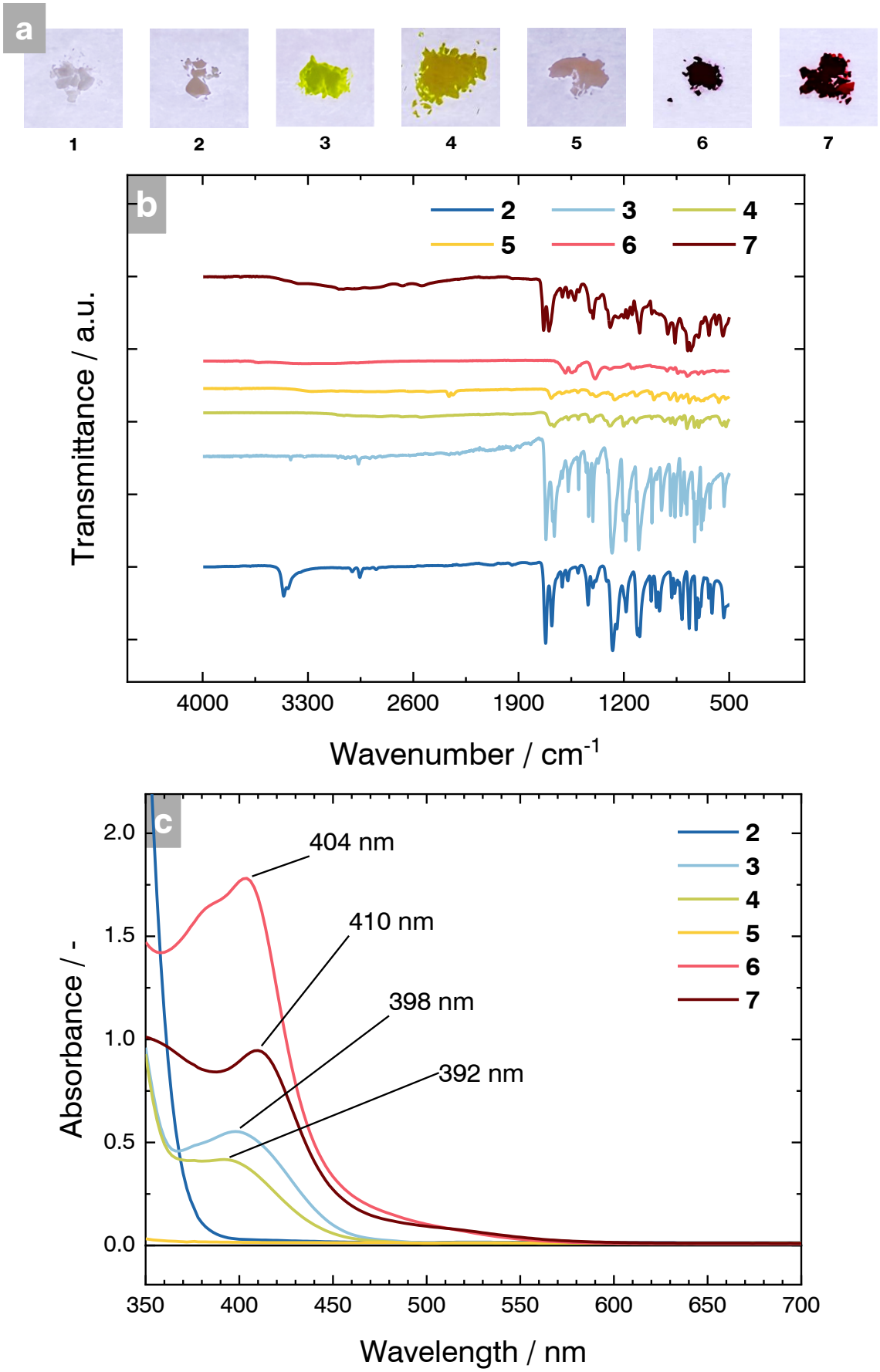

Figure 8. a) Photographic images of the reactant **1** as well as the reaction products **2** to **7**. **b)** IR spectra of **2** to **7** recorded from the solids in the ATR-mode. **c)** Solution UV-Vis absorption spectra of **2** to **7**.

4.1.2. Attempted synthesis of bis(dithiolene dibenzoic acid)nickel(II) (linker B)

Literature research revealed that **2** may also serve as starting material for the synthesis of linker **B** (**9**) *via* the intermediate bis(dithiolene dibenzoic acid dimethyl ester)nickel(II) (**8**) [50,71,77]. Although not part of the original task of this thesis, attempts to synthesise this dithiolene linker were initialised. Difficulties were encountered during the synthesis of this intermediate **8**. The synthesis of **8** from **2** consists of two individual steps in the same reaction flask. First, **2** is refluxed with phosphorous pentasulphide in dioxane. After some time, a nickel(II) salt is added to the refluxing reaction mixture to afford **8** *via* complexation (**Scheme 16**).

As a starting point, synthesis protocols [71,77] were followed but the crude product was afforded as a black-tarry material difficult to purify by the filtration method described therein. Since no precise reaction temperatures were reported, the influence of this parameter was investigated first. The reaction was conducted with 1.5 equivalents of phosphorous pentasulphide at temperatures of 90, 110 and 130 °C. The best results were obtained at 90 °C. There, small dark green to black needles crystallised from the black-tarry crude product upon cooling at 0 °C overnight. An attempt to separate the crude product *via* column chromatography failed. It was assumed that the problem of the reaction was bad selectivity towards formation of **8**, resulting in a high concentration of byproducts. Next, the effect of the addition of different equivalents of phosphorous pentasulphide (1.0, 1.2, 1.4, 1.6 and 1.8 eq.) on the reaction was studied at 90 °C. The best results were obtained with 1.0 and 1.2 equivalents of phosphorous pentasulphide, since there the most crystals were obtained upon cooling the crude product. However, again it was neither possible to separate these crystals by filtration from the black-tarry crude product nor to purify the crude product by means of column chromatography.

Studying the list of citations of [77], it was found that some publications claimed the addition of ammonium sulphate to the reaction mixture increases the yield of the reaction. Following [57], **2** was mixed with phosphorous pentasulphide (1.0 eq.) as well as a substoichiometric amount of ammonium sulphate and refluxed in dioxane at 90 °C for twelve hours. Upon evaporation of the solvent, a black solid crystallised, which could be finally purified *via* column chromatography to afford **8**. Even after intensive literature research, no answer was found why ammonium sulphate proves to be an advantageous additive for the synthesis of dithiolenes. Due to time constraints, synthesis of **9** and the derived MOFs was not possible anymore but is part of ongoing research.

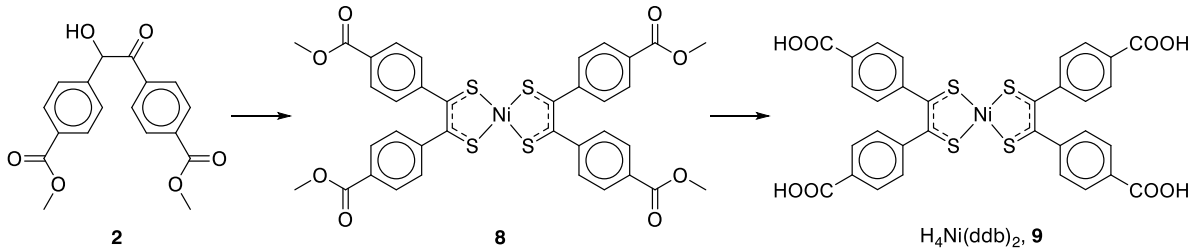

Scheme 16. Summarised reaction scheme for the synthesis of linker **9**, starting from **2**. Intermediate **8** was afforded and characterised, the synthesis of **9** is a matter of ongoing research.

Compound **8** was characterised by means of optical appearance, ^{1}H-NMR, FT-IR and UV-Vis spectroscopy. A photographic image of **8** shows its dark green to black colour (**Figure 9 a**). The ^{1}H-NMR of compound **8** (appendix, **Figure 27**) was in accordance with literature data [50,71,77]. As can be observed from the IR spectrum (**Figure 9 b**), **8** featured the typical asymmetric stretching modes of the methyl ester group C-H_3 (2949 cm^{-1}), the carbonyl C=O double bond (1717 cm^{-1}) as well as the C-O-C bond (1298 cm^{-1}). Due to appearing in the fingerprint region of the IR spectrum, the S=C=C=S stretching mode may only be tentatively assigned to the band at 883 cm^{-1} [78]. In the UV-Vis absorbance spectrum (**Figure 9 c**), compound **8** showed an intensive absorbance band in the NIR region (absorbance maximum at 844 nm) as well as a less pronounced but broad absorbance band at 594 nm. The intensive absorbance in the NIR region is a feature typically encountered for nickel bis(dithiolene) complexes, making them suitable candidates for applications as NIR dyes [79–81], absorber materials for novel medical imaging procedures [82] or light-induced drug release [83,84].

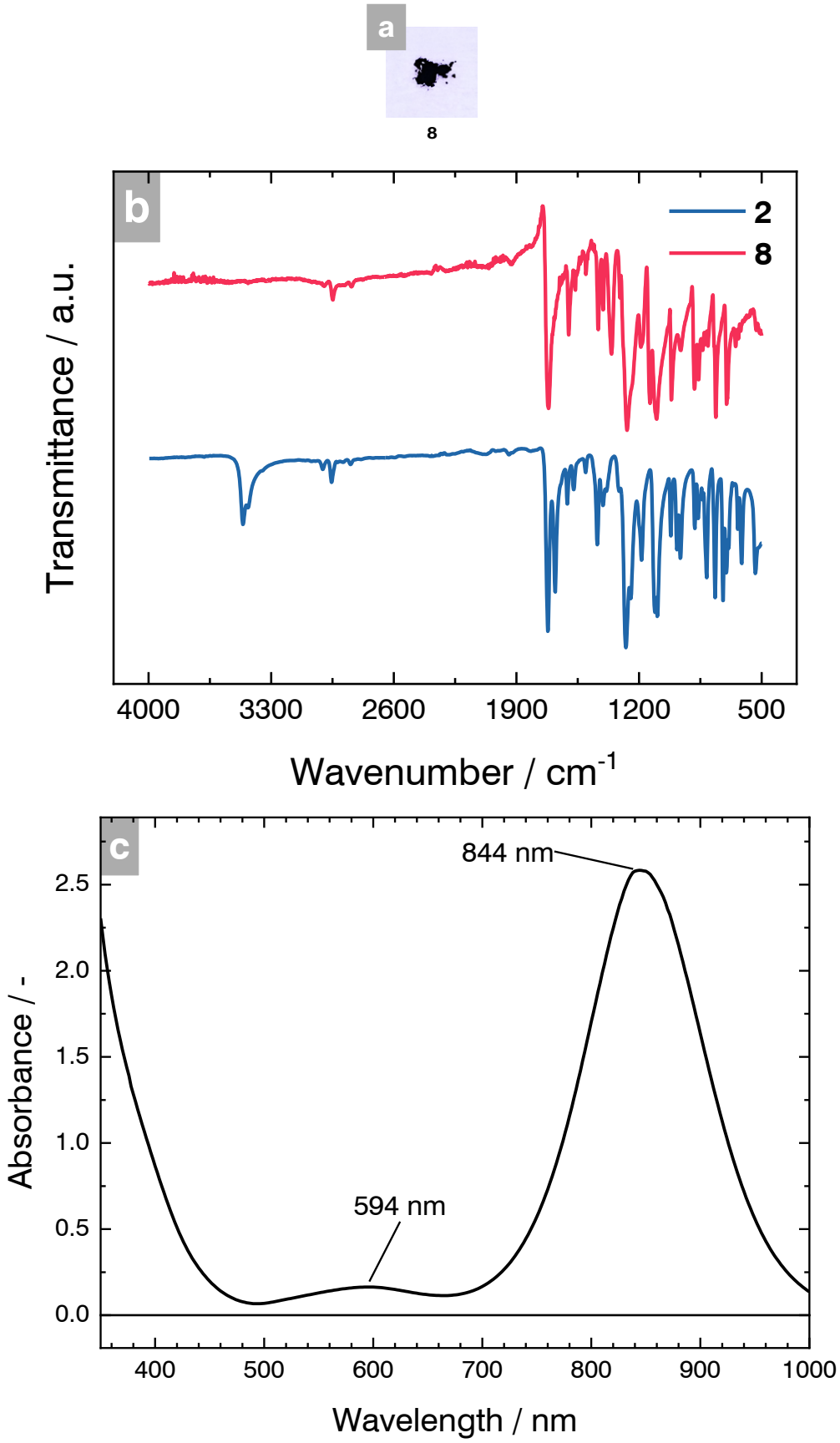

Figure 9. a) Photographic image of the reaction products **8**. **b)** IR spectra of **2** and **8** recorded from the solids in the ATR-mode. **c)** Solution UV-Vis absorption spectra of **8**.

4.1.3. Attempted synthesis of bis(di(benzene-3,3',4,4'-tetrahydroxy) glyoximato)nickel(II) (linker E)

An unexplored area in the field of MOFs involves the hydroxy-linker of **7**, named bis(di(3,4-dihydroxyphenyl)glyoximato)nickel(II), linker **E** (**14**). Synthesising MOFs comprising this linker is of particular interest due to the enhanced electrical conductivities, typically observed in hydroxy analogues derived from carboxyl linkers [44,46,47,49]. This thesis successfully established a foundational step by synthesising the intermediate veratril (**12**), the tetramethoxy analogue of **3**. Benzoin condensation of veratraldehyde (**10**) afforded veratroin (**11**), which was oxidised to yield **12**. Despite multiple attempts, the subsequent synthesis of pure 3,3',4,4'-tetrahydroxybenzil (**13**), a necessary precursor to **14**, was not achieved. **Scheme 17** offers an overview of the synthesis attempt. While literature provides some information on synthesising **13**, it is typically not purified, but instead the crude product is directly used further as a synthetic intermediate [58,85].

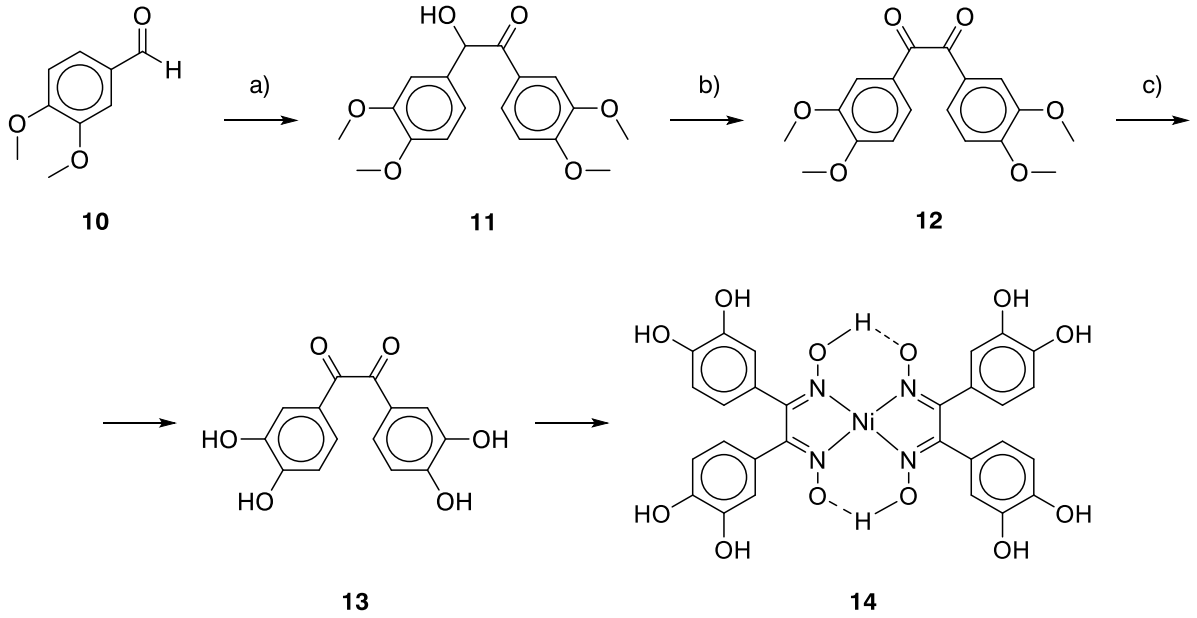

Scheme 17. Summarised reaction scheme for the synthesis of proposed linker **14**, starting from veratraldehyde (**10**). Intermediate **12** was purified and characterised, the synthesis of **13** and **14** is a matter of ongoing research. Reaction conditions: **a)** KCN in catalytic amounts, EtOH/H_2O, reflux; **b)** $CuSO_4 \cdot 5\ H_2O$, pyridine/water, reflux; **c)** HBr/H_2O, reflux.

An older study claims to have synthesised and purified **13** *via* deetherification of **12** in boiling hydrobromic acid followed by recrystallisation from water [86]. Several attempts were made to repeat this synthesis, varying the amount of hydrobromic acid, reaction temperatures and reaction durations. The reactions were conducted at temperatures of 95, 120 and 140 °C for periods of 12,

24 and 50 hours [xix]. All experiments conducted at 140 °C resulted in a black tarry mixture, from which no yellow solid precipitated upon water addition. Lower reaction temperatures combined with longer reaction times favoured the precipitation of a yellow solid when water was added to the concentrated reaction mixture. However, ^{1}H-NMR spectroscopy of the precipitated product revealed impurities that persisted even after recrystallisation from water.

Despite these challenges, evidence of at least partial deetherification was obtained. The IR spectrum of the deetherified product of **12** exhibited broad and strong bands around 3300 cm^{-1}, characteristic of the asymmetric stretching of free hydroxy groups. Additionally, prolonged exposure of the yellow solid to light and atmospheric conditions resulted in a colour change to brownish-black, a behaviour typical of catechol derivatives oxidising to their *o*-quinonoid derivatives under similar conditions [87].

To effectively isolate the deetherified product, it may be advantageous to protect the free hydroxy groups as easily cleavable ethers or esters, which can be subsequently deprotected to yield **13**. This approach would allow for more efficient purification *via* recrystallisation or column chromatography, due to a reduction of polarity. Potential protection strategies include etherification to form *p*-methoxybenzyl ethers, which can be mildly deprotected using 2,3-dichloro-5,6-dicyano-1,4-benzoquinone (DDQ) [88], or esterification with acetoxy groups, which can be deprotected under acidic reflux conditions [89].

12 appeared as a pale-yellow solid (**Figure 10 a**). Its ^{1}H-NMR spectrum (**Figure 28**) was in accordance with previously reported data [59]. Due to their similar chemical shifts, the two individual singlets of the *m*- and *p*-methoxy groups were overlapping. The IR spectra of **12** and crude **13** are shown in **Figure 10 b**. The IR spectrum of **12** exhibited the characteristic carbonyl stretching band from the benzil moiety at 1651 cm^{-1}. Furthermore, the ether C-O stretches are visible at 1265 (aromatic C-O stretch) and 1011 cm^{-1} (methyl C-O stretch). Upon deetherification, a broad band spanning from 3600 to 2900 cm^{-1} appeared, originating from the hydroxyl group O-H vibration. Additionally, the band at 1011 cm^{-1} was considerably reduced in intensity, indicating that deetherification was partially successful. Probably, the afforded product still contains considerable amounts of byproducts.

[xix] According to reaction monitoring *via* TLC, shorter reaction times than twelve hours did not indicate sufficient conversion of the reactant.

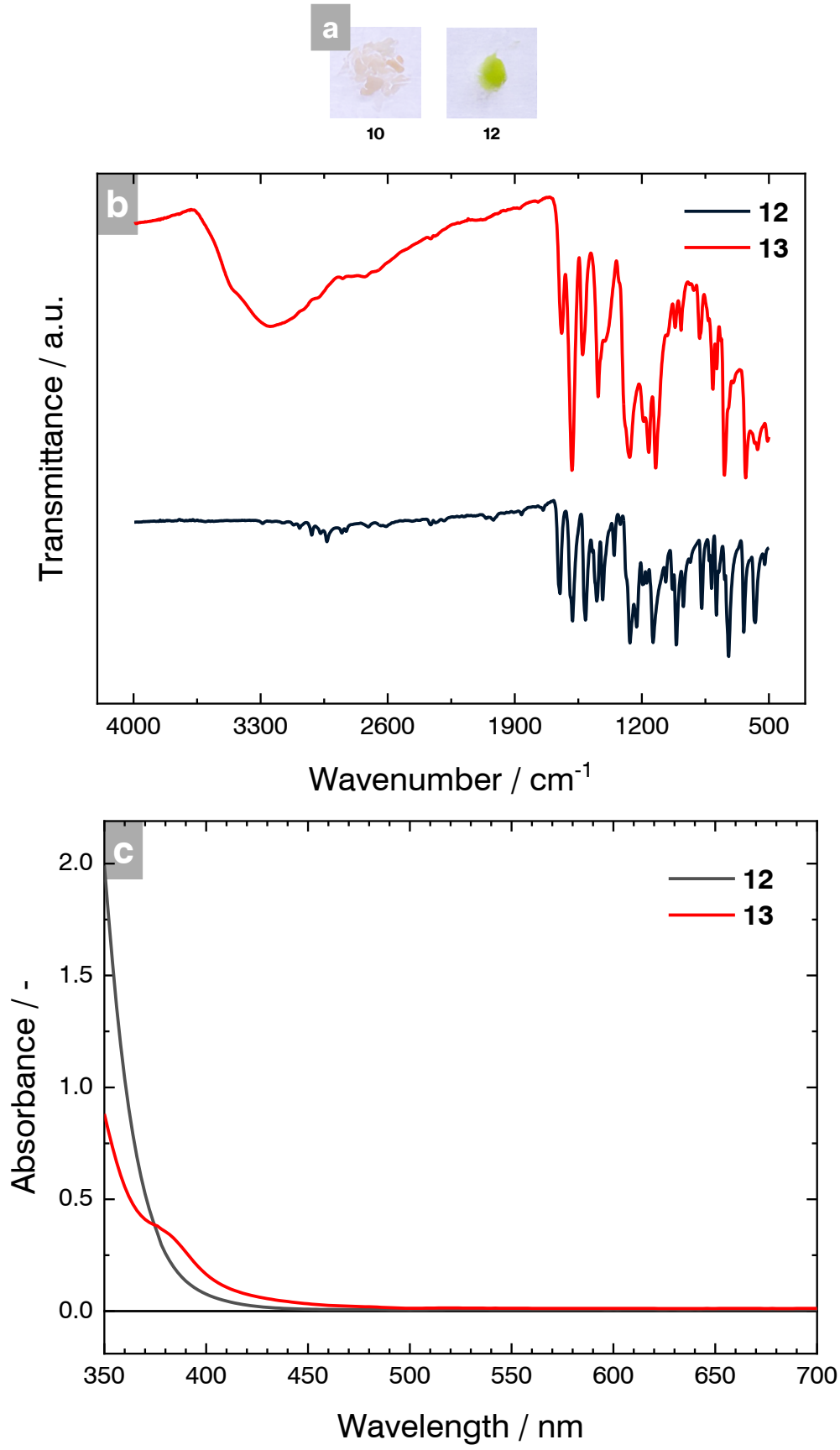

Figure 10. a) Photographic images of the reactant **10** as well as the reaction product **12**. **b)** IR spectra of **12** and crude **13** recorded from the solids in the ATR-mode. **c)** Solution UV-Vis absorption spectra of **12** and crude **13**.

4.1.4. Synthesis and characterisation of MOFs based on 7

MOFs based on **7** were prepared following a solvothermal protocol, outlined in the experimental section starting from page 30. Within this thesis, numerous different metal cations were applied to synthesise MOFs, including metal cations with varying oxidation states. In total, 21 MOFs derived from 20 different metal species (copper was used in the +I and +II oxidation state) were successfully afforded. Out of these 20 metal species, nine were main group metals, eight from the transition group and three from the lanthanoids. The applied metal cations as well as their oxidation states are highlighted in the periodic table presented in **Figure 11**. Red (+I), orange (+II), green (+III) and blue (+IV) colour fills denote the different oxidation states with which the metal ions were incorporated in the MOFs. All MOFs, except for **Mn-7** and **Zn-7**, are a novelty to literature and have been prepared the first time in the course of this work.

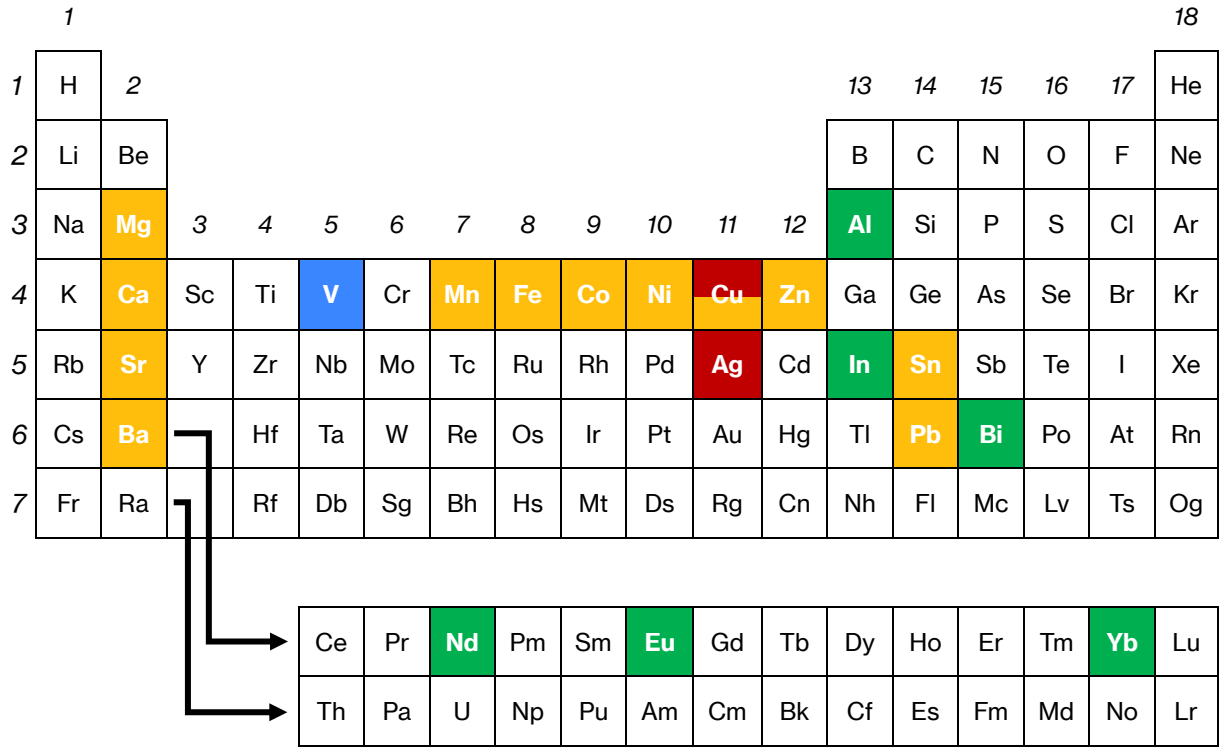

Figure 11. Representation of the periodic table of elements, highlighting the different metal cations utilised as SBUs for MOF synthesis. Colour fills denote the different oxidation states, with which the metals were incorporated into the MOFs: Red (+I), orange (+II), green (+III) and blue (+IV).

As can be seen from **Figure 12**, all MOFs showed intensive colours, spanning the whole visible spectrum, with exception of the violet and blue region.

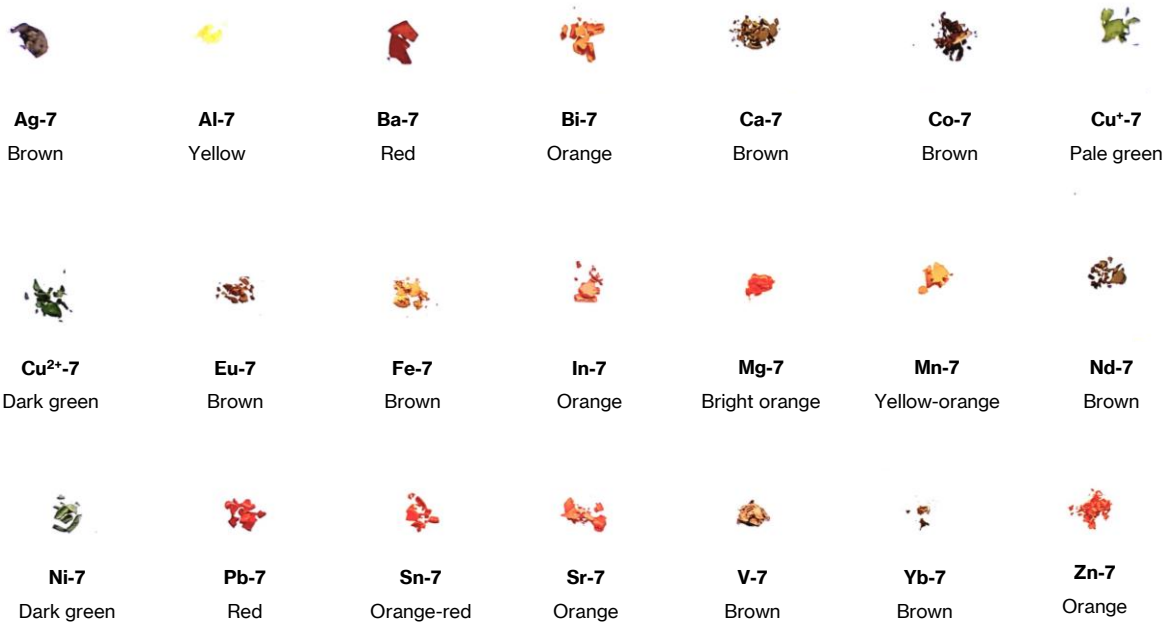

Figure 12. Photographic images of the pristine MOFs.

FT-IR spectra of the pristine MOFs were recorded in the ATR-mode to study their composition (**Figure 13**). The FT-IR spectra indicate that all MOFs contained the linker **7**. This is proven by the very dominant band at approximately 1400 cm^{-1}, originating from the asymmetric stretching mode of the carboxylate moieties of **7**. For a rigorous assessment of the solid-state structure of the MOFs, XRD studies are still required. Furthermore, Brunauer-Emmet-Teller (BET) gas adsorption studies are necessary to quantify the specific surface areas of the MOFs.

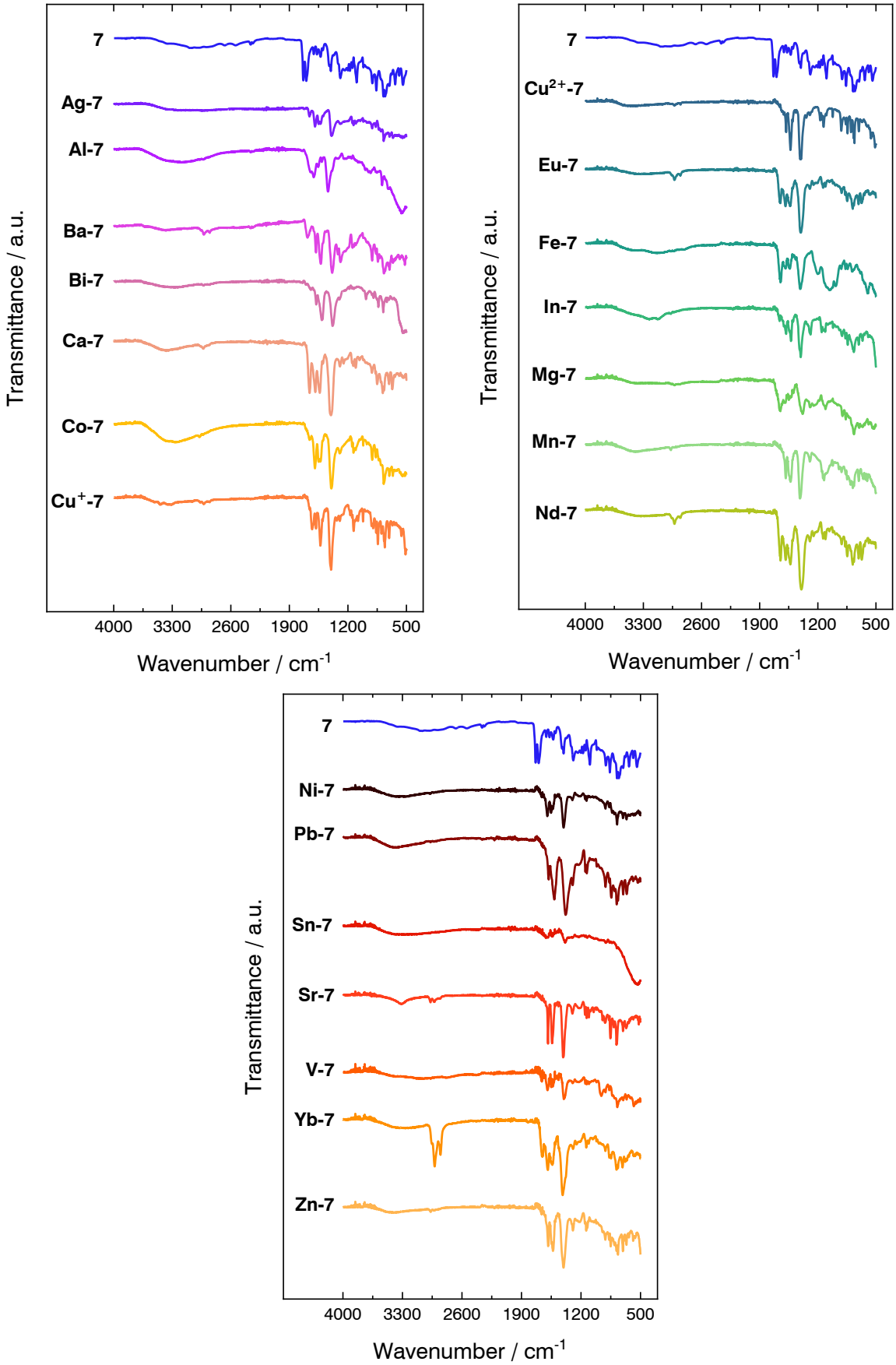

Figure 13. Summarised IR spectra of the pristine MOFs, recorded from the solids in the ATR-mode. The intensive bands at 1400 cm^{-1} are indicative for the carboxylate moieties of linker **7**. For comparative purposes, the IR spectrum of pristine **7** is shown as blue graph.

4.2. Electrochemical experiments

The electrocatalytic activity of MOFs was determined *via* CV. The CV-experiments were conducted with a standard three-electrode setup. The WE was comprised of a GC disk electrode, with a MOF-suspension (MOF suspended in ethanol with Nafion as a binder) drop cast onto it. Platinum as well as a Ag/AgCl (3 M KCl) electrode were used as CE and RE, respectively. All measurements were performed in a borate buffer electrolyte at pH 8.5. The electrolyte was purged with either nitrogen (blank measurements), carbon dioxide (for CO_2RR) or oxygen (for ORR) for 30 minutes. Uncatalysed reactions were performed with GC disk electrodes drop cast with Nafion only under carbon dioxide or oxygen. Upon purging with carbon dioxide, the pH of the borate buffer was shifted to 6.2. According to the carbonic acid speciation diagram, approximately 50 % of the dissolved carbon species is present in the form of free carbon dioxide at a pH of 6.2 [90].

Initially, a phosphate buffer of pH 7.0 was used as an electrolyte. However, many MOFs appeared to be unstable in the phosphate buffer. They readily dissolved and left a white coating on the GC disk electrodes behind, indicative for a pure Nafion-film. This issue comprised the MOFs containing the following SBUs: Ba, Bi, Ca, Co, Fe, Mg, Mn, Pb, Sr, V. After some studies it was found that this issue may be resolved by using a borate buffer of pH 8.5 as an electrolyte. The majority of the MOFs previously unstable in the phosphate buffer were stable in the borate buffer. Only **Ca-7**, **Mg-7** and **Mn-7** were still dissolving even in the borate buffer. The question arising was, why the MOFs instable in the phosphate buffer were suddenly stable in the borate buffer. The instability issue may not be attributed to the linker, *e.g.* disintegration of the oxime moiety of **7**. Firstly, in this case, the effect must have had affected every MOF. However, only certain MOFs showed the instability issue. Secondly, in a separate experiment, a film of pristine **7** was soaked in the phosphate buffer overnight without showing significant dissolution effects. Consequently, the instability issue may rather be attributed to the disintegration of the SBUs. Most probably, the phosphate buffer dissolved the SBUs of the MOFs by forming insoluble phosphates with them. Earth alkaline metals, for example, are known to form sparingly soluble phosphates.

As stated previously, the electrocatalytic activity of the MOFs was assessed using CV. In CV, a potential is ramped between two vertices at a defined scan rate whilst recording the current response. This technique is well suited for electrocatalytic activity tests, owing its high sensitivity to detect redox processes. A catalyst is active towards carbon dioxide or oxygen reduction, if its voltammogram shows distinct Faradaic currents in the cathodic scan, which are both absent during the blank measurement and the measurement performed without the catalyst. Most notably, only certain MOFs showed electrocatalytic effects, namely **Co-7**, **Fe-7** and **Ni-7** in the case of CO_2RR and **Ba-7**, **Cu^+-7**, **Eu-7**, **Ni-7**, **Pb-7**, **Sn-7** and **Yb-7** for ORR. All other MOFs showed no difference in the appearance of their CVs from the cases of purging with nitrogen or the blank measurements. Consequently, this implies catalytic effects are not solely dependent on the linker **7** alone but depend on the interaction between **7** and SBUs. In the following two chapters, the results of the

electroactivity studies of the MOFs are presented separately for CO_2RR and ORR. For didactic reasons, results from the ORR will be discussed first. It shall be noted that this study was only interested in a proof-of-concept, if the MOFs exhibit an electrocatalytic activity towards CO_2RR and ORR. Consequently, their activity was not quantified using the parameters introduced in chapter 2.1.1., but only roughly estimated based on their peak current densities.

4.2.1. Electrocatalytic activity tests of MOFs based on 7 towards oxygen reduction

Figure 14 presents the voltammograms of **Ba-7**, **Cu^{+}-7**, **Cu^{2+}-7**, **Eu-7**, **Ni-7**, **Pb-7**, **Sn-7** and **Yb-7** recorded for the ORR. Except for **Cu^{2+}-7**, the voltammograms recorded under oxygen (blue traces) exhibit distinct reduction signals absent both during blank measurements (green traces) and the uncatalysed experiments (violet traces). The MOFs exhibited irreversible reduction reactions, as indicated by the absence of re-oxidation signals. **Cu^{2+}-7** did not show an electrocatalytic effect towards ORR. Its voltammogram is presented for comparative purposes only. The current density trace of **Cu^{2+}-7** was smaller under oxygen than under nitrogen (**Figure 14 c**). This observation is noteworthy, because the only difference between **Cu^{+}-7** and **Cu^{2+}-7** is the oxidation state with which the SBU was incorporated into the MOF. Whereas **Cu^{+}-7** showed an electrocatalytic effect, **Cu^{2+}-7** did not. An explanation for this finding may be that both MOFs adopt different solid-state structures, which exert different catalytic properties.

Depending on the type of current density response, three cases may be differentiated:
(i) MOFs exhibiting the appearance of a distinctive diffusion-limited reduction peak under oxygen, with peak current densities larger than those recorded under nitrogen or during the blank measurements (**Ba-7**, **Eu-7**, **Ni-7**, **Sn-7** and **Yb-7**, depicted in **Figure 14 a**, **d**, **e**, **g**, **h**, respectively);
(ii) as for the case of **Cu^{+}-7** (**Figure 14 b**), a MOF showing no distinctive reduction peak under oxygen but a plateau current density, approximately 800 to 1000 µA cm^{-2} more cathodic than under nitrogen or during the blank measurement;
(iii) for **Pb-7** (**Figure 14 f**), a catalytic wave missing diffusion limitation;

Table 3 summarises performance data extracted from the voltammograms. Half-peak potentials are particularly valuable for comparing CV performance data, as they are less prone to shifts caused by changing scan rates. However, they could only be extracted for **Ba-7**, **Eu-7**, **Ni-7**, **Sn-7** and **Yb-7**, because these MOFs showed reduction peaks, contrary to **Cu^{+}-7** and **Pb-7**. To facilitate comparison, onset potentials were also reported.

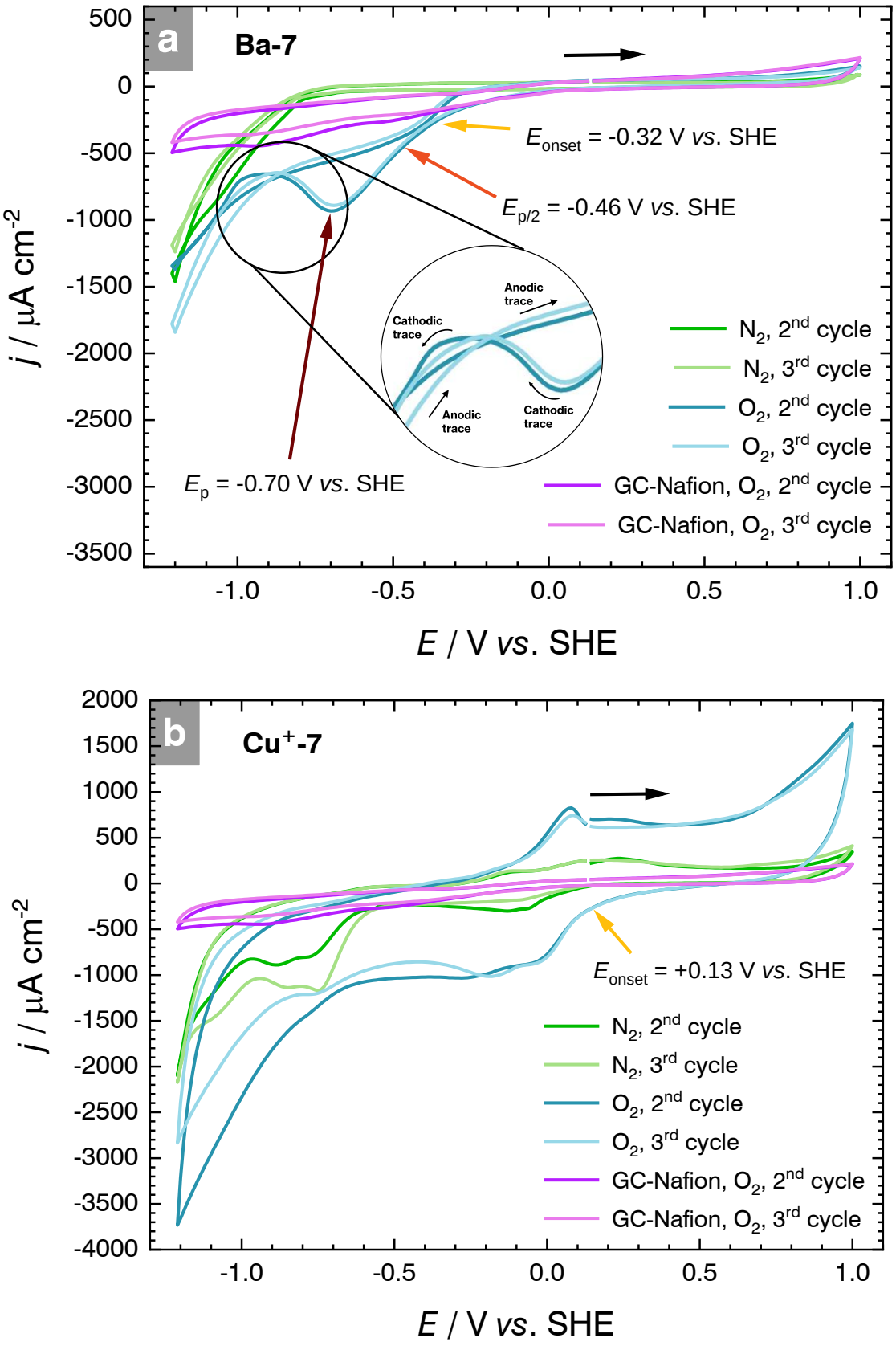

Figure 14. Voltammograms recorded for ORR at scan rates of 20 mV s^{-1}. **a) Ba-7** and **b) Cu$^+$-7**. Blue, green and violet traces denote measurements under oxygen, nitrogen and without catalyst, respectively.

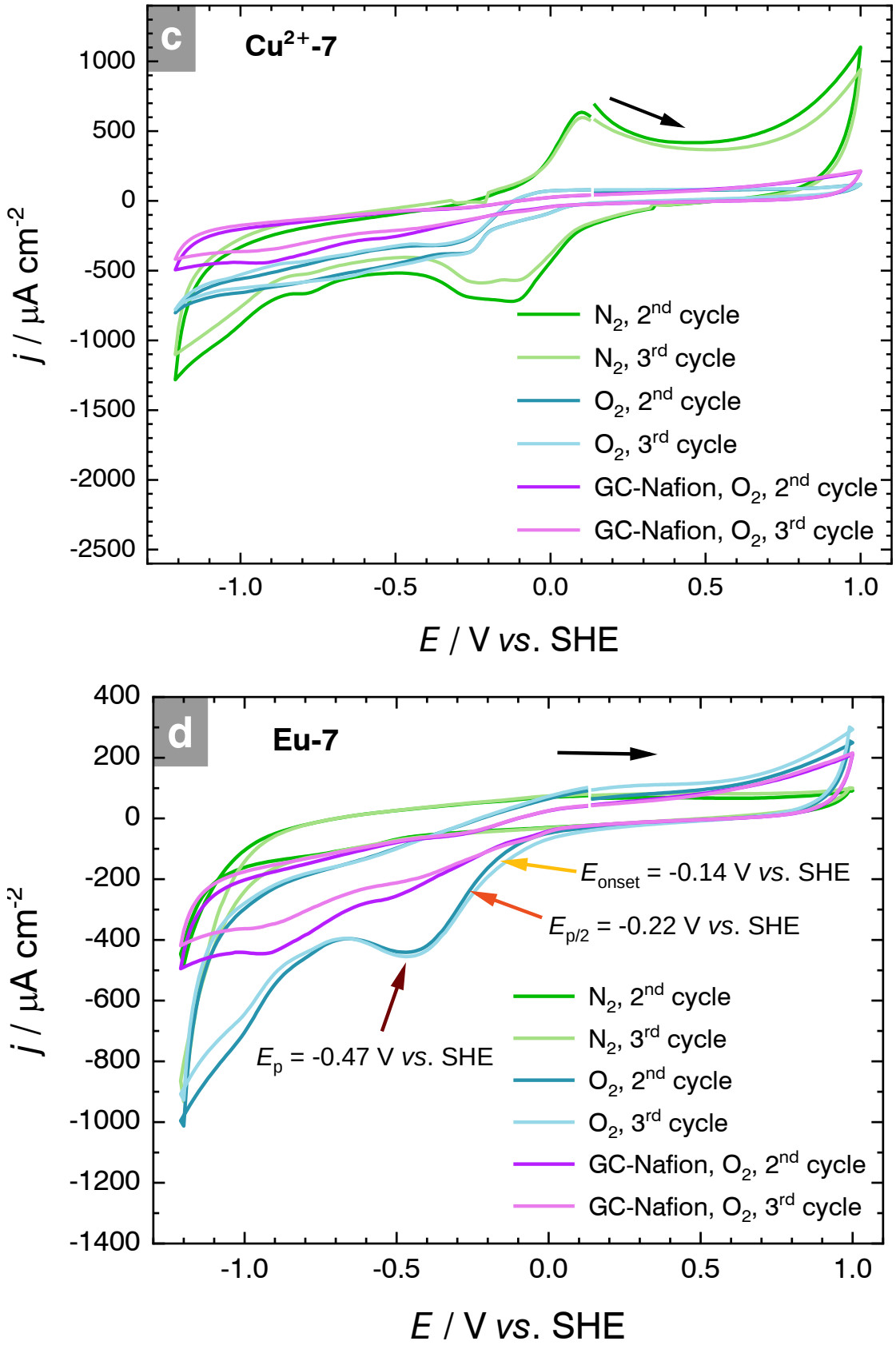

Continuation of **Figure 14.** Voltammograms recorded for ORR at scan rates of 20 mV s^{-1}. **c) Cu^{2+}-7** and **d) Eu-7**. Blue, green and violet traces denote measurements under oxygen, nitrogen and without catalyst, respectively.

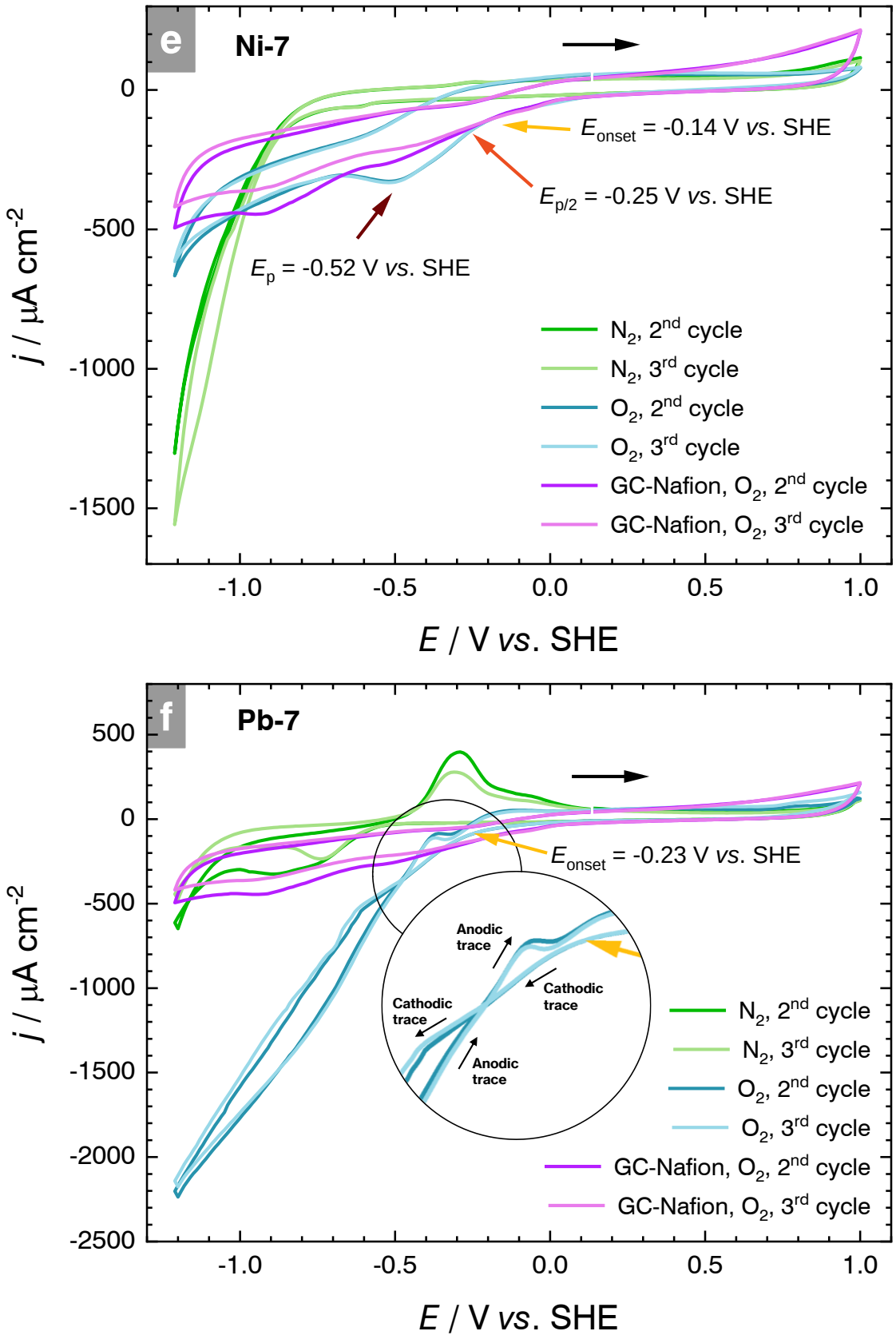

Continuation of **Figure 14.** Voltammograms recorded for ORR at scan rates of 20 mV s^{-1}. **e) Ni-7** and **f) Pb-7**. Blue, green and violet traces denote measurements under oxygen, nitrogen and without catalyst, respectively.

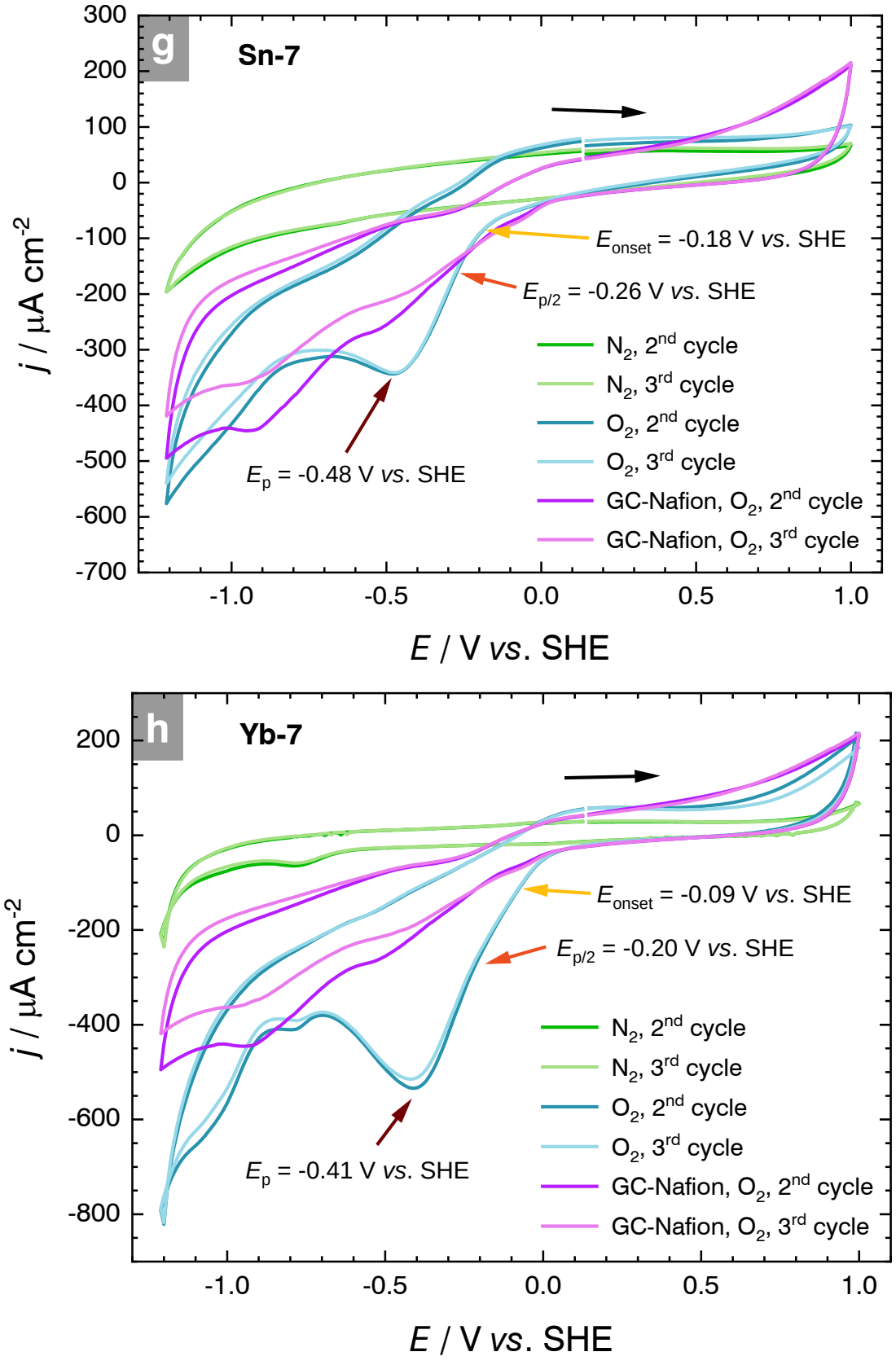

Continuation of **Figure 14.** Voltammograms recorded for ORR at scan rates of 20 mV s^{-1}. **g) Sn-7** and **h) Yb-7**. Blue, green and violet traces denote measurements under oxygen, nitrogen and without catalyst, respectively.

Cu⁺-7 showed an onset potential of +0.13 V *vs.* SHE, indicating the least overpotential for ORR among all MOFs. **Ba-7** exhibited the most negative onset potential of -0.32 V *vs.* SHE, but also the largest cathodic peak current density of -933 µA cm^{-2}, indicating high catalytic activity at the cost of high overpotential. **Ba-7** also exhibited the most negative half-peak potential. **Yb-7** displayed the least negative half-peak potential of -0.20 V *vs.* SHE, but only showed a moderate peak current density of -534 µA cm^{-2}. The smallest peak current density was observed for **Ni-7** (-332 µA cm^{-2}). **Pb-7** emerges as a superior MOF for ORR, owing its absence of mass-transfer limitations. It exhibited an onset potential of -0.23 V *vs.* SHE, approximately 5 to 10 mV more cathodic than most other MOFs. At a potential of -0.50 V *vs.* SHE (approximately the mean value of cathodic peak potentials of other MOFs), **Pb-7** showed a current density of -384 µA cm^{-2} which is on the order of the peak current density of **Sn-7**.

Table 3. Summarised performance data for electrocatalytic ORR experiments. Data were extracted from the voltammograms shown in **Figure 14**. E_{onset} ... Onset potential, $E_{p/2}$ ... Half-peak potential, E_p ... Peak potential, j_p ... Peak current density.

MOF	E_{onset} / V *vs.* SHE	$E_{p/2}$ / V *vs.* SHE	E_p / V *vs.* SHE	j_p / µA cm^{-2}
Ba-7	-0.32	-0.46	-0.70	-933
Cu⁺-7	+0.13	---	---	---
Eu-7	-0.14	-0.22	-0.47	-455
Ni-7	-0.14	-0.25	-0.52	-332
Pb-7	-0.23	---	---	---
Sn-7	-0.18	-0.26	-0.48	-341
Yb-7	-0.09	-0.20	-0.41	-534

Interestingly, **Ba-7** and **Pb-7** showed so-called *curve crossing* in their CVs, as highlighted by the inserts in **Figure 14 a** and **f**. Curve crossing may be observed, if the current density of the cathodic scan is smaller than that of the oxidative scan, indicative for an induction period. This suggests that the pristine MOFs act as precatalysts. The active catalysts are formed from this precatalysts whilst approaching cathodic potentials. This progressively increases the concentration of the active catalyst species, resulting in higher catalytic currents as the CV progresses.

4.2.2. Investigation of oxygen reduction during electrolysis experiments

To be able to draw at least limited conclusions on their productivity, Faradaic efficiency as well as stability of the electrocatalytically active MOFs, electrolysis experiments were conducted. Due to time constraints, only **Pb-7** was tested, as it demonstrated the most promising electrocatalytic activity in CV experiments, with no apparent mass-transfer limitations. Selectivity in

the oxygen reduction reaction is less of an issue, as the primary competing product to hydrogen peroxide (two-electron reduction) is water (four-electron reduction). Consequently, only hydrogen peroxide was quantified. Electrolysis experiments were conducted in an H-cell, with separate anolyte and catholyte compartments. The electrolyte solution consisted of a borate buffer at pH 8.5. The electrochemical setup utilised a standard three-electrode system, comprising a GC plate electrode drop-cast with the MOF suspension as WE, a platinum CE and a Ag/AgCl (3 M KCl) RE. The potential was maintained at -0.4 V *vs.* SHE under chronoamperometric conditions. Prior to electrolysis, the catholyte was purged with oxygen for 30 minutes. During electrolysis, oxygen purging of the catholyte was continued at a low rate. Samples were collected every hour and quantified for hydrogen peroxide using a standard photometric method.

Figure 15 illustrates both the productivity, measured as the substance amount of hydrogen peroxide generated (solid dots) and the Faradaic efficiency (open dots) as functions of electrolysis time. Both parameters increased with prolonged electrolysis time. The initial productivity was approximately 3 µmol cm^{-2} h^{-1} hydrogen peroxide, which increased to 8 µmol cm^{-2} h^{-1}, while the Faradaic efficiency improved from an initial value of approximately 30 to finally 60 %. This behaviour is atypical, as Faradaic efficiency usually decreases over time due to deactivation of catalytically active centres. These findings suggest that during electrolysis a possible surface activation process enhances the catalyst's activity resulting in an increase of both productivity and Faradaic efficiency. However, the duration of electrolysis was limited to six hours. It is possible that both productivity and Faradaic efficiency may eventually plateau or decrease after six hours. Visual inspection of the GC electrode post-electrolysis revealed no signs of degradation or delamination. This, along with the observed increase in Faradaic efficiency, indicates that **Pb-7** is a stable electrocatalyst for the ORR.

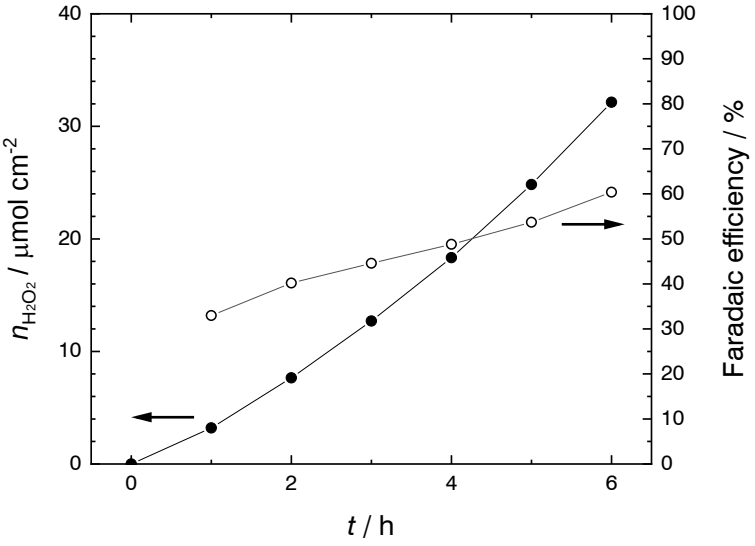

Figure 15. Plot of the hydrogen peroxide productivity (solid data points) as well as Faradaic efficiency (open data points) *versus* electrolysis time for electrolysis experiments performed with **Pb-7** drop cast onto GC plate electrodes (surface area of 4 cm^2).

It is important to note that the electrolysis conditions, including pH and applied potential, have not been optimised. It is reasonable to assume that further optimisation could enhance both productivity and Faradaic efficiency in future experiments. Other MOFs electroactive towards oxygen reduction have not yet been subjected to electrolysis tests and thus no additional results are available at this stage; this remains an area of ongoing research.

4.2.3. Electrocatalytic activity tests of MOFs based on 7 towards carbon dioxide reduction

Figure 16 presents the voltammograms of the CO_2RR experiments performed with **Co-7**, **Fe-7** and **Ni-7**. The voltammograms recorded under carbon dioxide (red traces) exhibit distinct reduction signals absent both during blank measurements (green traces) and the uncatalysed experiments (violet traces). All MOFs showed a re-oxidation peak during CO_2RR with a large peak-to-peak separation, implying a non-Nernstian response, *i.e.* hindered reversibility [91]. Owing this re-oxidation signal, it may be assumed that no gaseous species, like carbon monoxide, or methane, are produced during CO_2RR. Contrary to **Fe-7**, the current density response of **Co-7** and **Ni-7** displayed mass-transfer limitations. Both **Fe-7** and **Ni-7** showed curve crossing.

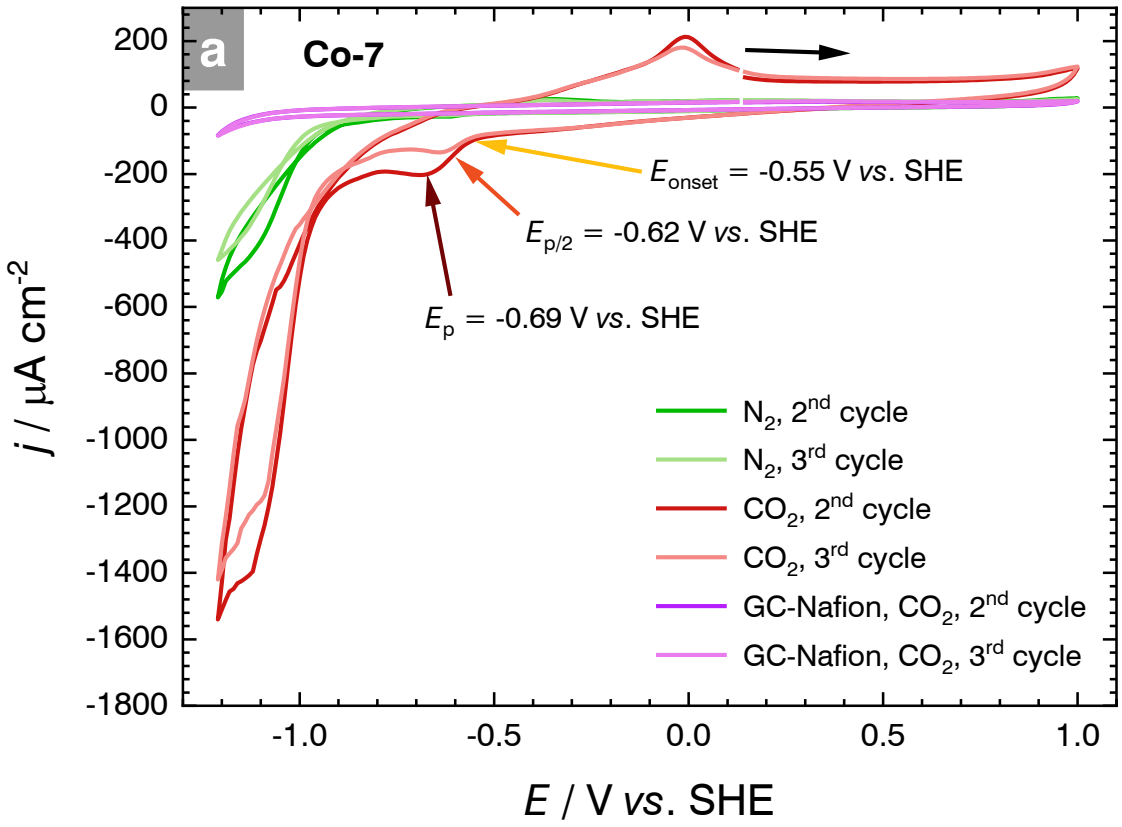

Figure 16. Voltammograms recorded for CO_2RR at scan rates of 20 mV s^{-1}. **a) Co-7**. Red, green and violet traces denote measurements under carbon dioxide, nitrogen and without catalyst, respectively.

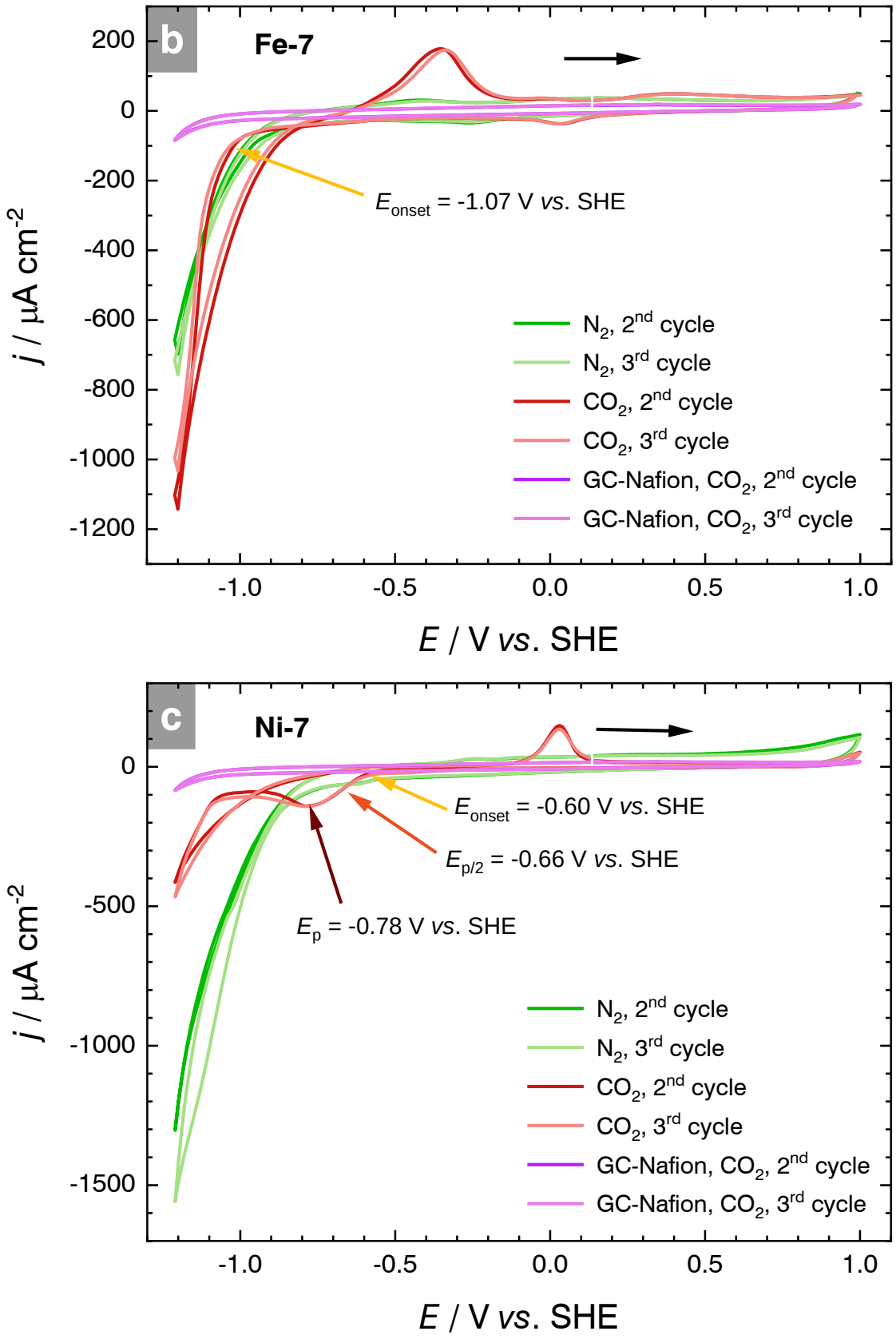

Continuation of **Figure 16.** Voltammograms recorded for CO_2RR at scan rates of 20 mV s^{-1}. **b) Fe-7** and **c) Ni-7**. Red, green and violet traces denote measurements under carbon dioxide, nitrogen and without catalyst, respectively.

The performance parameters of **Co-7**, **Fe-7** and **Ni-7** are summarised in **Table 4**. **Co-7** had the lowest onset potential (-0.55 V *vs.* SHE), followed by **Ni-7** (-0.60 V *vs.* SHE) and **Fe-7** (-1.07 V *vs.* SHE). Peak current densities ranged between -140 and -203 µA cm $^{-2}$, less than for ORR. The intensive cathodic current densities recorded below -1.0 V *vs.* SHE for **Co-7** and **Fe-7** may indicate that besides CO_2RR, considerable hydrogen evolution is occurring as a competing reaction. This would reduce the selectivity towards CO_2RR. Based on the observed small current densities of the MOFs towards the CO_2RR, it might be assumed that the synthesised MOFs are more active catalysts for the ORR than for CO_2RR. However, definitive conclusions cannot be drawn solely from the CV results. Comprehensive evaluations of all MOFs for their productivity and Faradaic efficiency during electrolysis experiments are required. Furthermore, an assessment of their product selectivity is necessary, as CO_2RR can yield multiple reaction products. These investigations are part of ongoing research.

Table 4. Summarised performance data for electrocatalytic CO_2RR experiments. Data were extracted from the voltammograms shown in **Figure 16**. E_{onset} ... Onset potential, $E_{p/2}$ ... Half-peak potential, E_p ... Peak potential, j_p ... Peak current density.

MOF	E_{onset} / V *vs.* SHE	$E_{p/2}$ / V *vs.* SHE	E_p / V *vs.* SHE	j_p / µA cm^{-2}
Co-7	-0.56	-0.62	-0.69	-203
Fe-7	-1.07	---	---	---
Ni-7	-0.60	-0.66	-0.78	-142

4.2.4. Electrochemical MOF deposition

The study aimed to investigate the conductivity of MOFs based on linker **7** using electrochemical impedance spectroscopy (EIS). This necessitated the preparation of MOF thin films on a conductive substrate. An electrochemical deposition route was employed for preparation of MOF thin films. It has already been shown previously that MOFs may be deposited on substrates by an electrochemical pH increase in the vicinity of the WE [92,93]. Therefore, redox reactions with proton-coupled electron transfer are utilised. Upon initialising a redox reaction, protons are consumed in the vicinity of the WE, elevating the local pH and initiating MOF precipitation. One of these redox pairs utilised in literature is the nitrate-nitrite couple. Upon reducing nitrate to nitrite, protons are consumed, initialising MOF precipitation on the WE. One issue encountered with this redox couple is that high overpotentials are required to efficiently drive MOF precipitation. Typically, potentials of -1.5 V *vs.* SHE are applied, restricting this technique to SBUs which are not reduced under these conditions [92,93]. Consequently, redox pairs exhibiting more anodic redox potentials are necessary to broaden the applicability of electrochemical MOF deposition. Here, the *p*-benzoquinone/hydroquinone couple is well suited. As shown in this thesis, it is possible to

efficiently drive electrochemical MOF deposition at potentials of -0.6 V *vs.* SHE. Upon reduction of *p*-benzoquinone, protons are consumed, elevating the local pH at the WE, initiating MOF deposition. Electrochemical MOF deposition was performed in the chronoamperometric mode, using a three-electrode setup and a DMF-based electrolyte with *p*-benzoquinone as redox active species. In a series of experiments, it was found, that a more homogeneous MOF film may be formed, if the potential is stepped consecutively from -0.4 V *vs.* SHE to -0.6 V *vs.* SHE, whereby each potential was held for 300 seconds. Due to the lower cathodic potentials required to drive electrochemical MOF deposition with *p*-benzoquinone, this method is applicable to a wider range of SBUs. An illustrative chronoamperometric trace of the deposition of **Zn-7** is shown in **Figure 17**. The initial large cathodic current density decreased asymptotically to reach a certain plateau value, indicating steady-state MOF growth conditions after initial MOF nucleation. Upon stepping the potential from -0.4 to -0.6 V *vs.* SHE at 300 seconds, the current density sharply increased before asymptotically decreasing again to a new steady-state value.

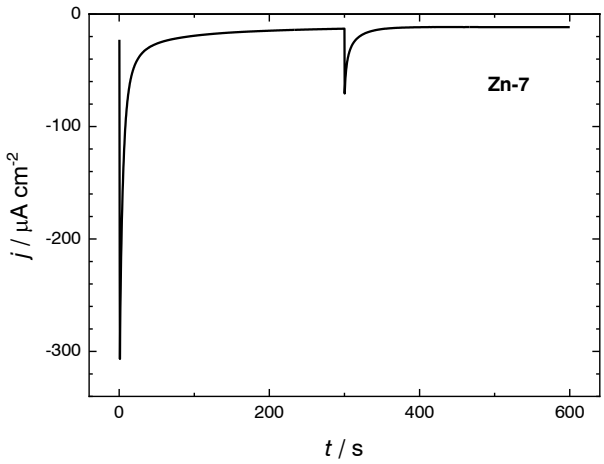

Figure 17. Chronoamperometric trace recorded upon electrochemical deposition of **Zn-7**. The deposition was performed at -0.4 and -0.6 V *vs.* SHE. Both potentials were held for 300 seconds each. The stepping from -0.4 to -0.6 V *vs.* SHE is indicated by the sharp current density increase at 300 seconds.

This novel electrochemical deposition technique with *p*-benzoquinone was successfully applied to prepare MOF thin films of **Mn-7** and **Zn-7** on fluorine-doped tin oxide (FTO) substrates. The colours of the deposited films were in accordance with the colours of the pristine MOFs (**Mn-7**: yellow, **Zn-7**: orange). To assess, if the deposited films consisted of the respective MOFs, IR spectra were recorded in the ATR mode and compared to IR spectra of the pristine MOFs. **Figure 18 a** and **c** show the IR spectra of **Mn-7** and **Zn-7**, respectively. **Figure 18 b** depicts an excerpt of the IR spectrum of **Mn-7** between 900 and 1700 cm^{-1}. A comparison between the IR spectra of the electrodeposited and the pristine MOFs indicates both species are identical. The electrodeposited films did not contain any residual *p*-benzoquinone. Most indicative are the matching bands at 1415 cm^{-1}, originating from the carboxylate moieties of the MOFs.

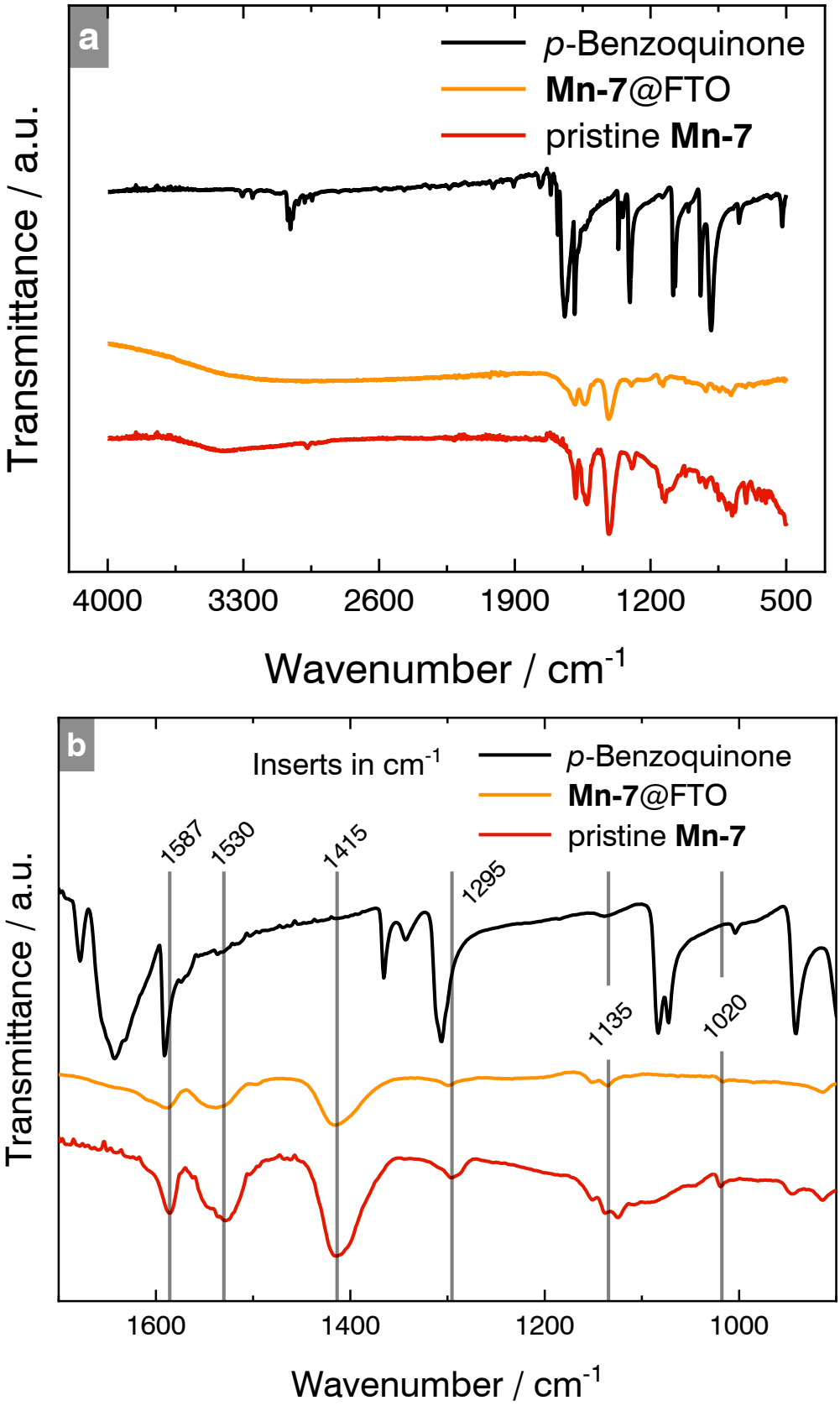

Figure 18. Comparison of the IR spectra recorded from the electrodeposited MOF thin films on FTO, the pristine MOFs and *p*-benzoquinone. All spectra were acquired from the solids in the ATR-mode. **a) Mn-7**, **b)** excerpt of the IR spectrum of **Mn-7** between 900 and 1700 cm^{-1}.

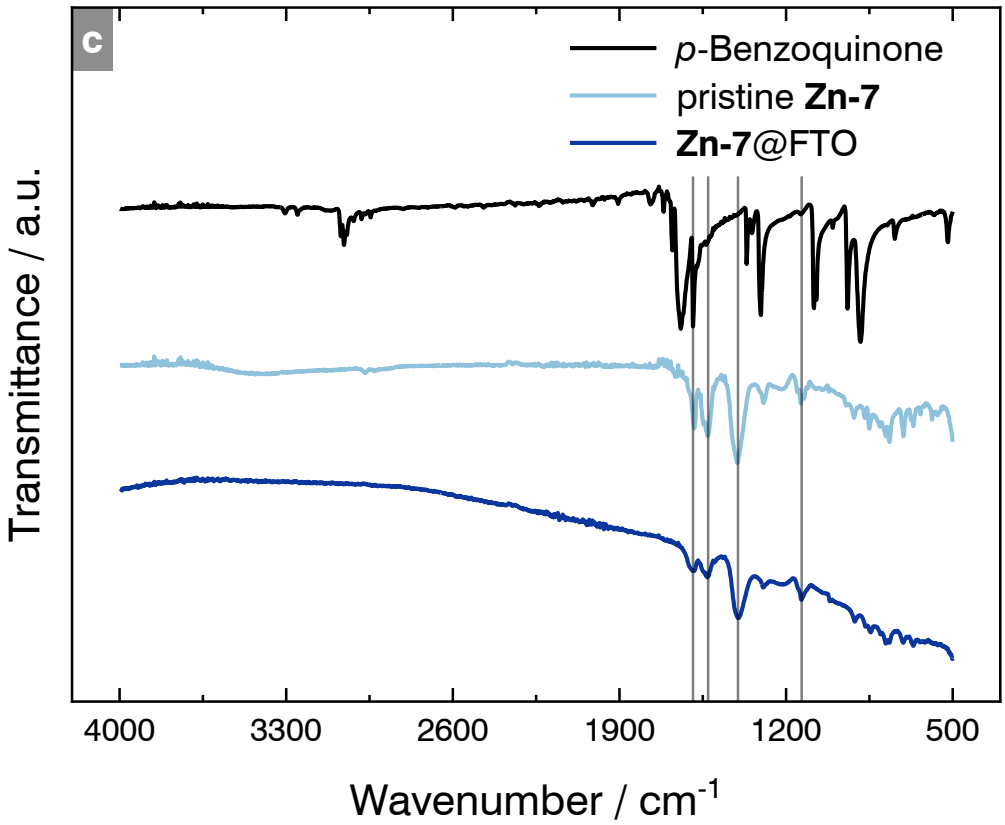

Continuation of **Figure 18.** Comparison of the IR spectra recorded from the electrodeposited MOF thin films on FTO, the pristine MOFs and *p*-benzoquinone. All spectra were acquired from the solids in the ATR-mode. **c) Zn-7**.

4.2.5. Attempted conductivity measurements

The conductivities of **Mn-7** and **Zn-7** thin films was attempted to be measured using EIS. Impedance spectra, shown in **Figure 19 a** and **b**, depict both impedance and phase shift as functions of frequency. Fitting the data to a simple Randles equivalent circuit model proved unsuccessful, particularly in the low-frequency region where significant deviations in phase shift were observed. Even advanced models considering electrode porosity [29] failed to resolve these discrepancies. Probably, the impedance was primarily measured from the underlying conducting FTO substrate and may not be attributed to MOF contributions. In future experiments, alternative conductivity measurement techniques should be explored, such as single-crystal conductivity measurements [94] or pressed-pellet conductivity measurements [95]. Given the anticipated low conductivities [xx], a two-point measurement setup should suffice [46].

[xx] Literature reports a conductivity of $2.0 \cdot 10^{-7}$ S cm^{-1} for **Mn-7** [53].

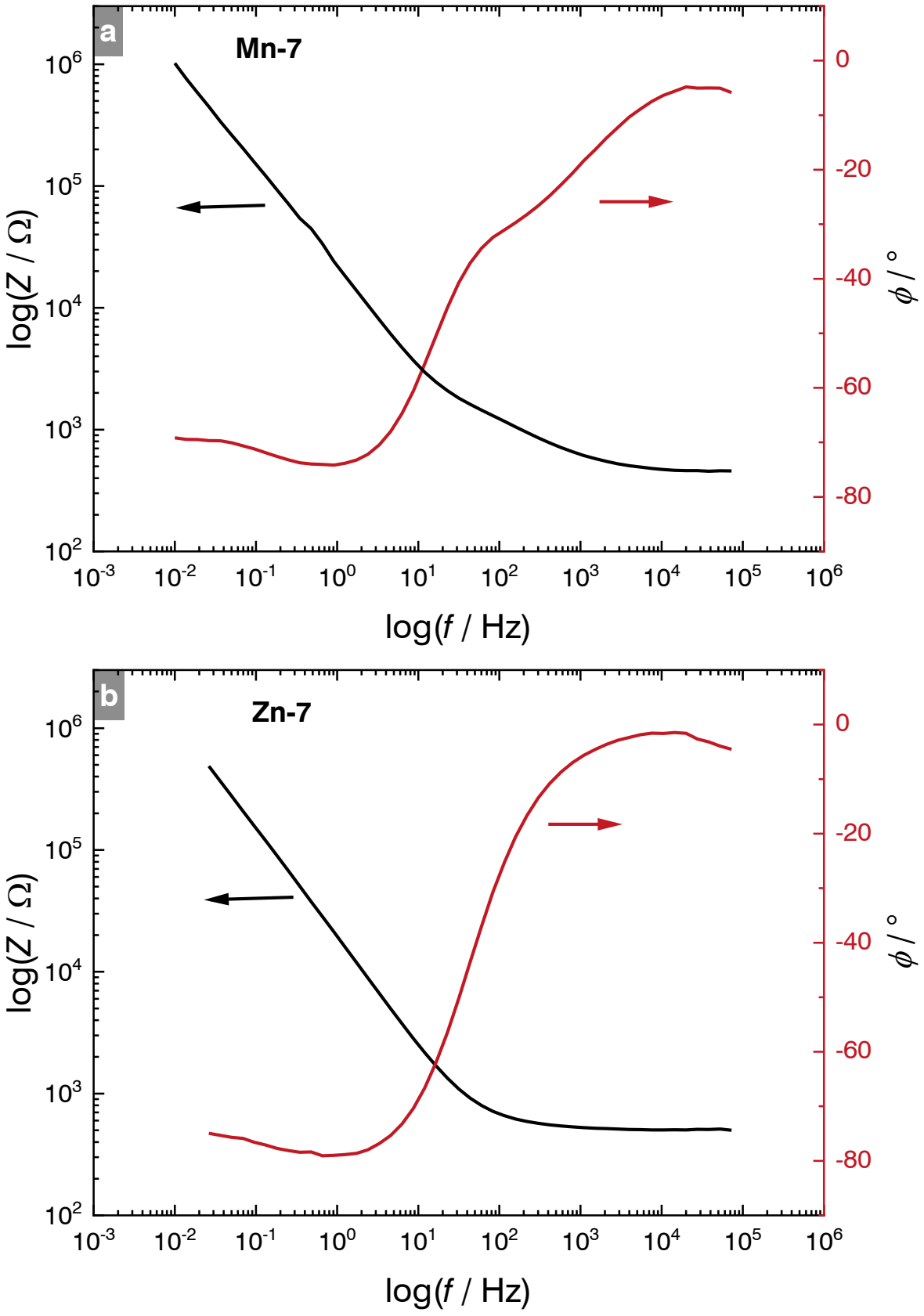

Figure 19. Electrochemical impedance spectra recorded from thin films of **a) Mn-7** and **b) Zn-7** electrodeposited onto FTO substrates. Black and red traces denote the impedance and phase shift responses, respectively. Impedance spectra are presented in the Bode plot format.

4.2.6. Spectroelectrochemical experiments with Mn-7 and Zn-7 thin films

Owing their transparency, thin films of **Mn-7** and **Zn-7** were subjected to spectroelectrochemical experiments. The spectra were recorded on a UV-Vis spectrophotometer with a three-electrode setup fitted inside a cuvette. **Figure 20 a** and **b** show the spectra of both **Mn-7** and **Zn-7**, respectively. Both **Mn-7** and **Zn-7** exhibited an absorbance band at approximately 420 nm, which decreased in intensity as more cathodic potentials were approached. This consistent behaviour in both MOFs suggests a reduction event occurring at the nickel(II) moiety of the linker. The exact oxidation state of nickel upon reduction is uncertain, as ionic oxidation states other than +II are rarely observed for nickel [96]. In **Mn-7**, the intensity of the absorbance band at 450 nm initially decreased upon increasing cathodic potentials. Beyond -0.65 V *vs.* SHE, the intensity of the band increased again. This observation may be assigned to a reduction of the manganese SBU. Manganese is a well-known redox-active species, readily undergoing redox reactions [97]. In **Zn-7**, the absorbance band with a maximum at 340 nm increased in intensity with increasing cathodic potentials. The specific redox event responsible for this change is uncertain, as both nickel and zinc are typically stable only in the +II ionic oxidation state [96,98].

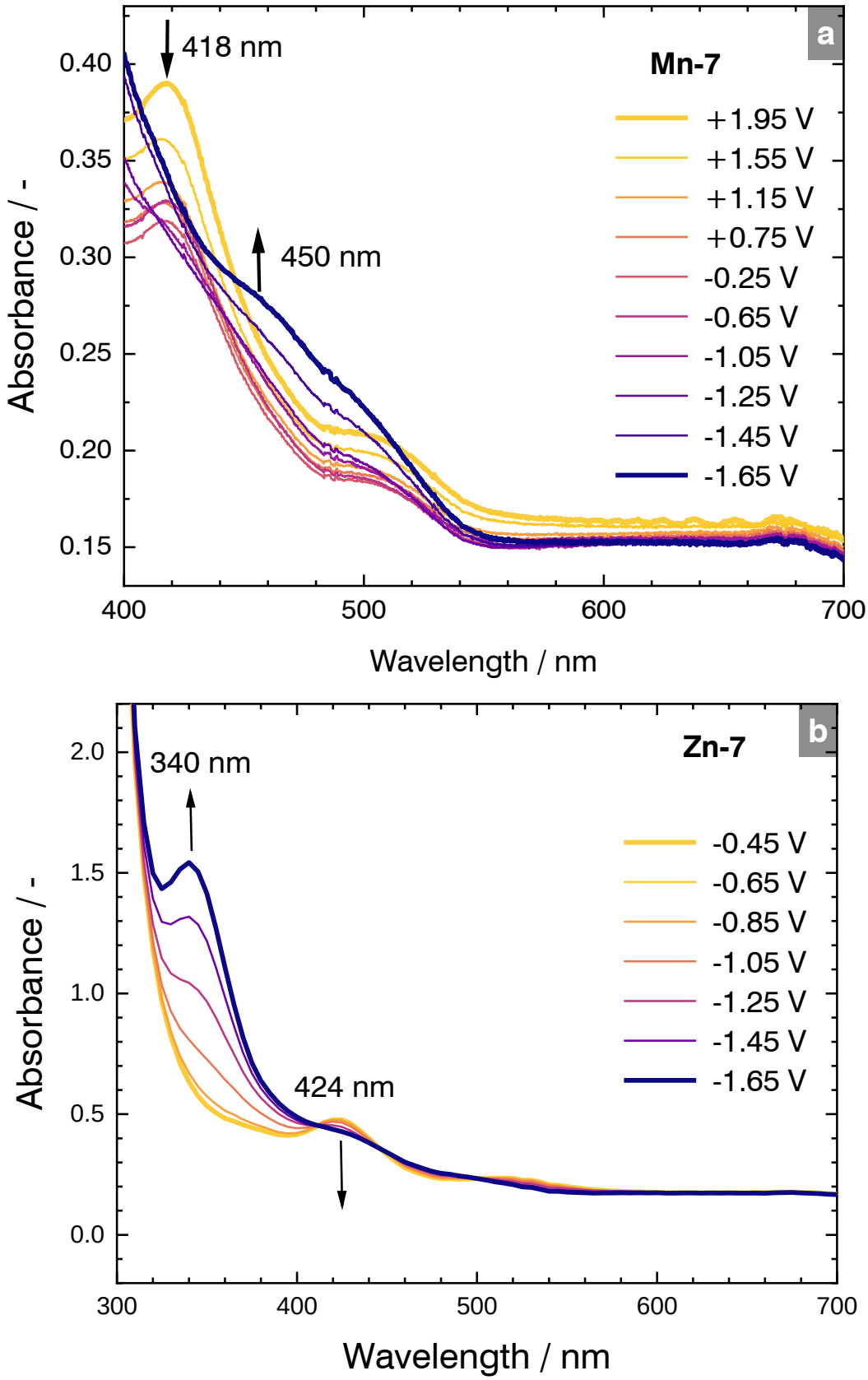

Figure 20. Graphs recorded during *in-situ* spectroelectrochemical experiments from **a) Mn-7** and **b) Zn-7**. Measurements were conducted from anodic towards cathodic potentials.

5

Conclusion and outlook

In conclusion, linker **7** and the corresponding MOFs were successfully synthesised. By optimising reaction conditions, recrystallisation and washing procedures, the total yield of the six-step synthesis was increased from 29% (as previously reported in the literature) to 45%. Among the 21 prepared MOFs, 19 are a novelty to literature. Further research is required to investigate their solid-state structures *via* X-ray techniques and their specific surface areas using BET isotherms. Future studies may also explore the synthesis of linkers **9** and **14**. While the synthesis of linker **9** is expected to be straightforward, the preparation of linker **14** will likely require purification strategies for the intermediate **13** using protection/deprotection methods.

This thesis served as a proof-of-concept that MOFs based on linker **7** are electrocatalytically active towards both CO_2RR and ORR. Specifically, **Co-7**, **Fe-7** and **Ni-7** were active towards CO_2RR, while **Ba-7**, **Cu^+-7**, **Eu-7**, **Ni-7**, **Pb-7**, **Sn-7** and **Yb-7** exhibited activity towards ORR. Electrocatalytic activities were assessed using CV techniques. Further investigations are necessary to determine kinetic parameters of the MOFs *via* the rotating ring-disk electrode method.

Preliminary conclusions may be drawn from electrolysis experiments for ORR, with **Pb-7** being the only MOF studied so far. **Pb-7** demonstrated Faradaic efficiencies of 60% after six hours of electrolysis and productivities of approximately 8 µmol cm^{-2} h^{-1}. **Pb-7** appeared to be stable under operating conditions, as no delamination events occurred and Faradaic efficiencies increased with increasing electrolysis time. Optimisation of electrolysis conditions, such as pH and applied potential, is expected to enhance both productivity and Faradaic efficiency. Further electrolysis experiments are required for all other MOFs, particularly for CO_2RR, to assess their productivity, selectivity and stability under operating conditions.

Additionally, a mild electrochemical MOF deposition method was developed and successfully applied to form thin films of **Mn-7** and **Zn-7** on FTO substrates. This novel method, which utilises relatively low cathodic potentials (maximum of -0.6 V *vs.* SHE), offers an advantage over existing protocols by being suitable for a variety of metal ion SBUs. Conductivity measurements *via* EIS were not successful due to data fitting problems. To accurately assess the conductivities of the prepared MOFs, techniques such as pressed-pellet probe or single-crystal conductivity measurements are likely to be more appropriate for future investigations.

6

Appendix

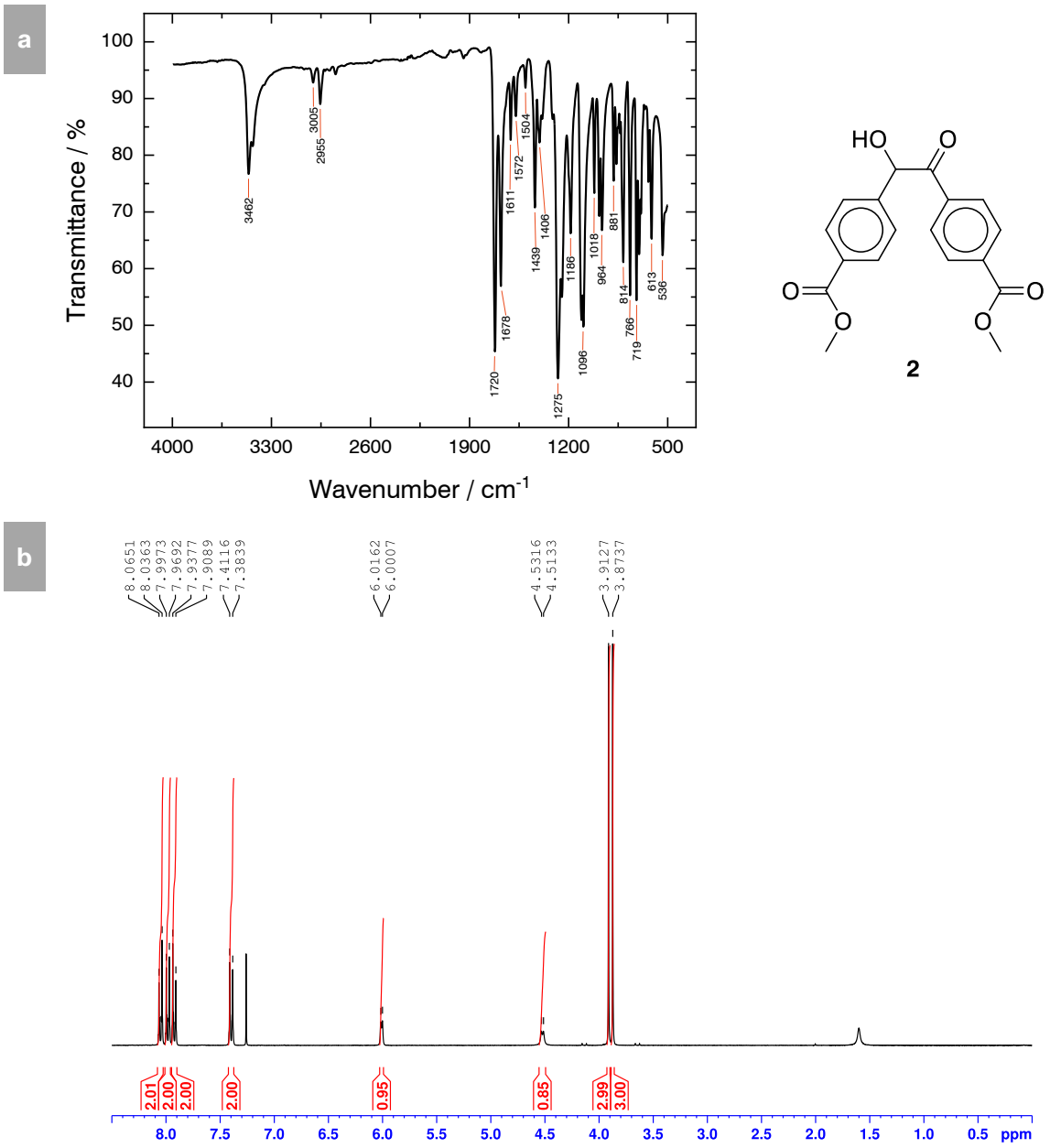

Figure 21. Spectroscopic characterisation of **2**. **a)** IR spectrum acquired from the solid sample in the ATR-mode. Inserts in cm^{-1}. **b)** ^{1}H-NMR recorded in $CDCl_3$ (300 MHz, 298 K).

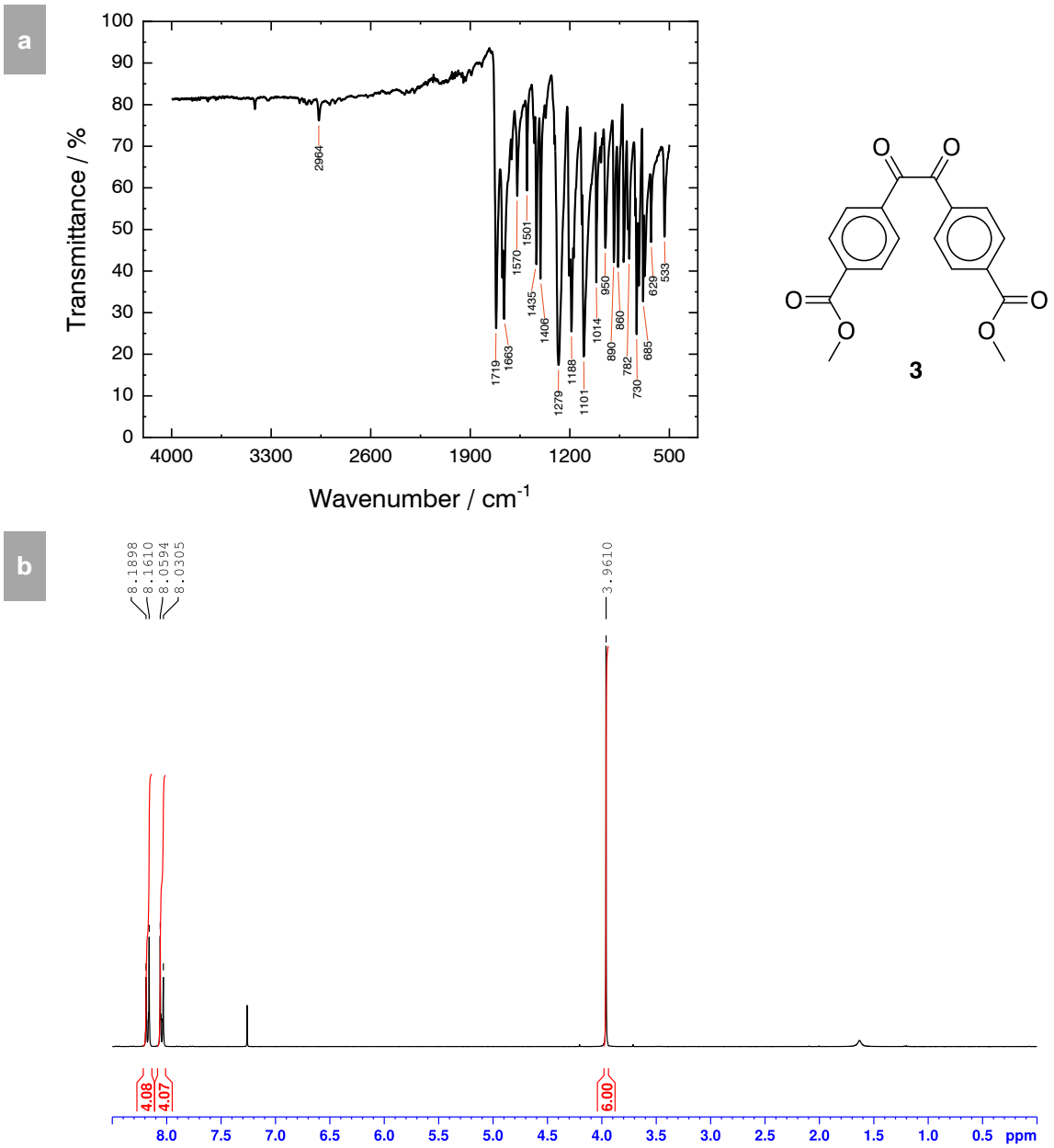

Figure 22. Spectroscopic characterisation of **3**. **a)** IR spectrum acquired from the solid sample in the ATR-mode. Inserts in cm^{-1}. **b)** ^{1}H-NMR recorded in $CDCl_3$ (300 MHz, 298 K).

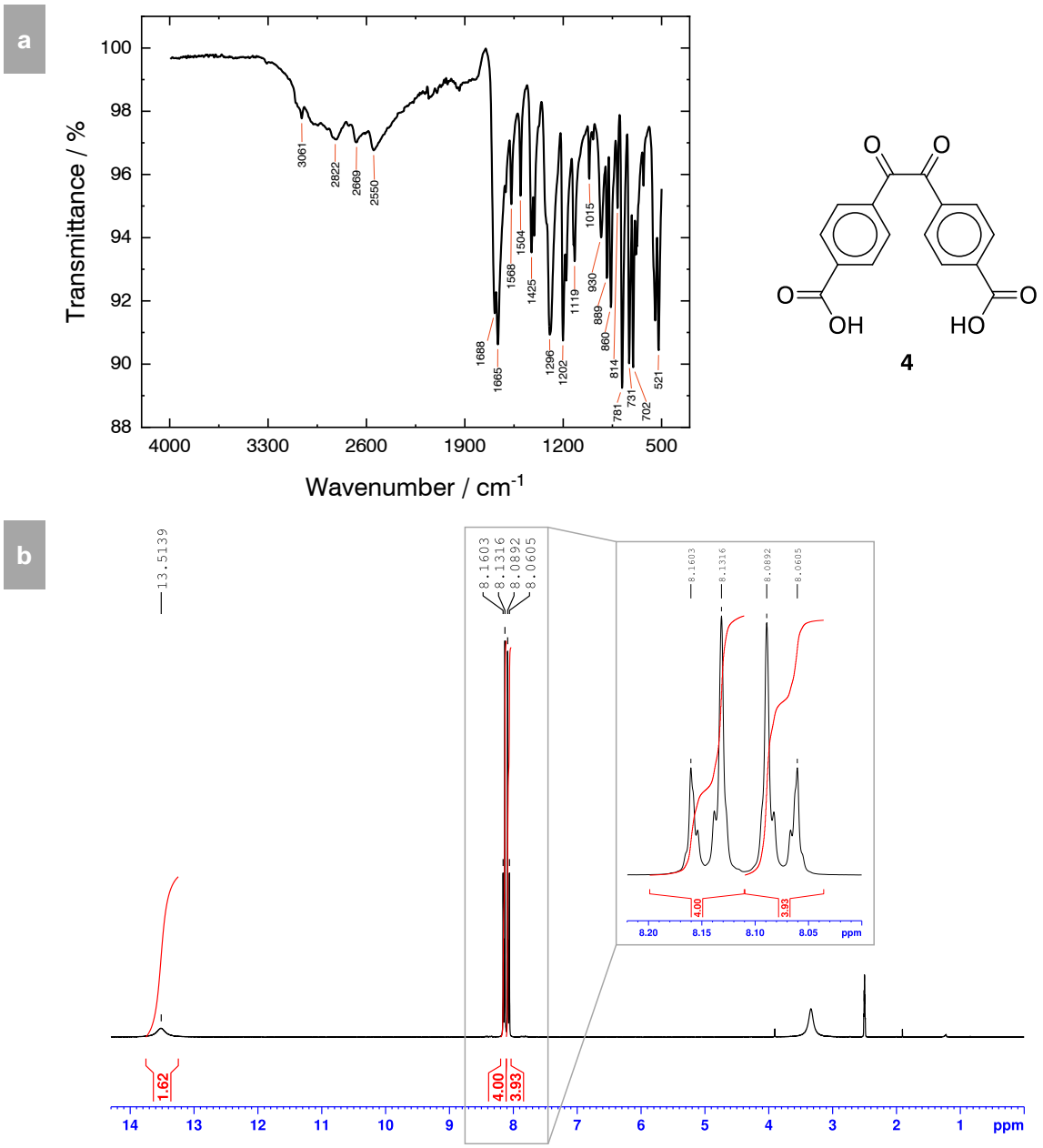

Figure 23. Spectroscopic characterisation of **4**. **a)** IR spectrum acquired from the solid sample in the ATR-mode. Inserts in cm^{-1}. **b)** ^{1}H-NMR recorded in DMSO-d_6 (300 MHz, 298 K).

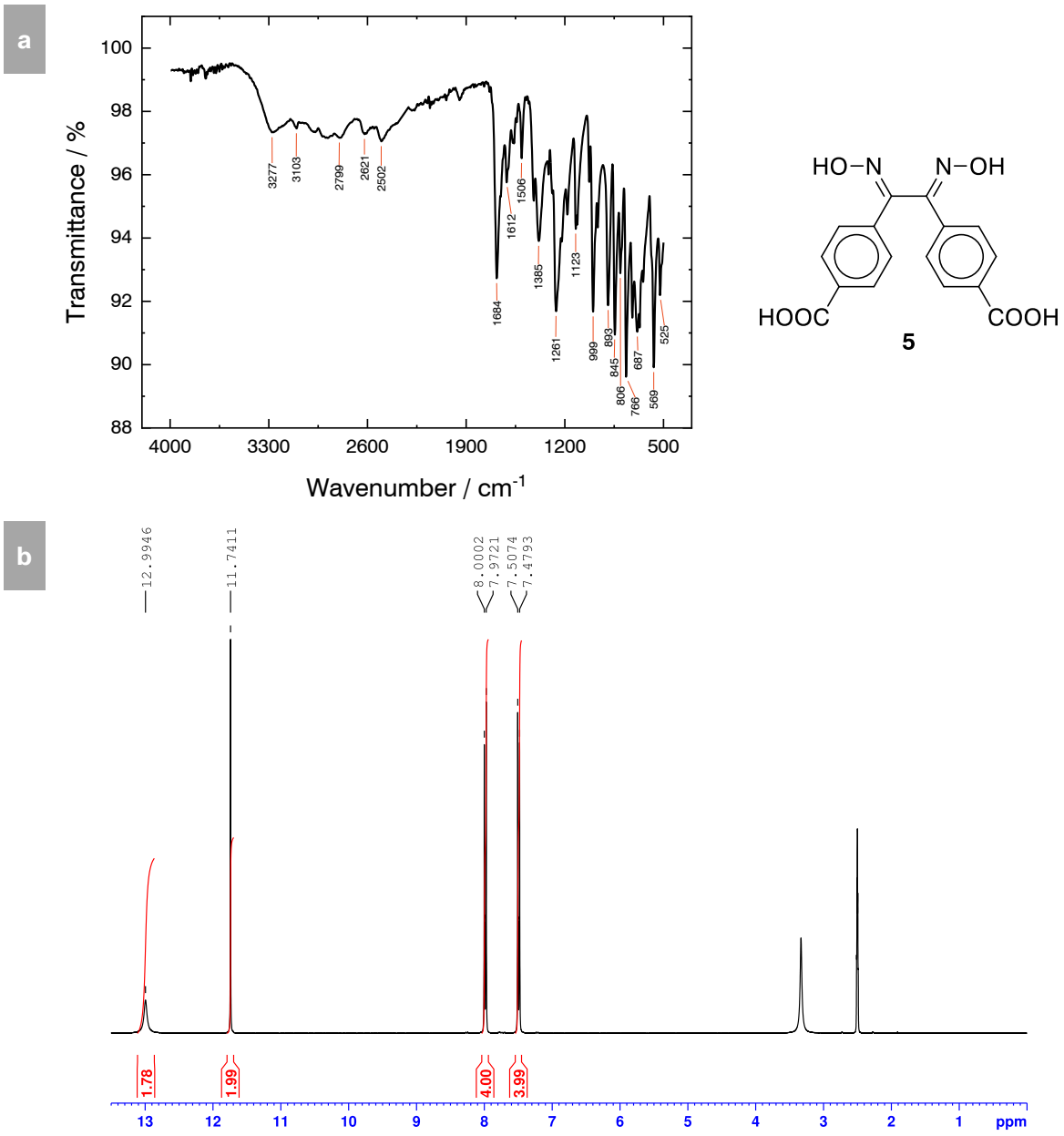

Figure 24. Spectroscopic characterisation of **5**. **a)** IR spectrum acquired from the solid sample in the ATR-mode. Inserts in cm^{-1}. **b)** ^{1}H-NMR recorded in DMSO-d_6 (300 MHz, 298 K).

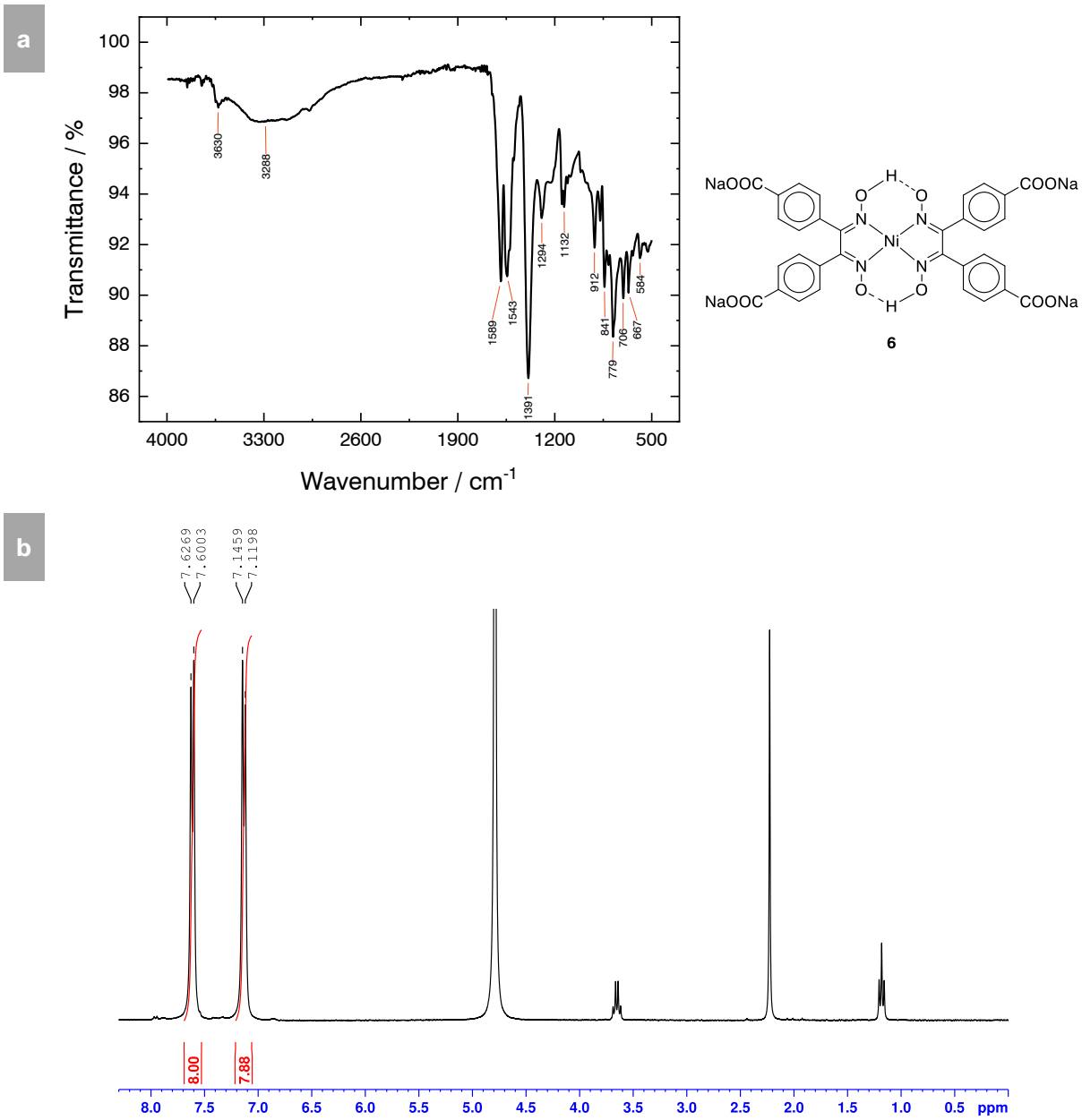

Figure 25. Spectroscopic characterisation of **6**. **a)** IR spectrum acquired from the solid sample in the ATR-mode. Inserts in cm^{-1}. **b)** ^{1}H-NMR recorded in D_2O (300 MHz, 298 K).

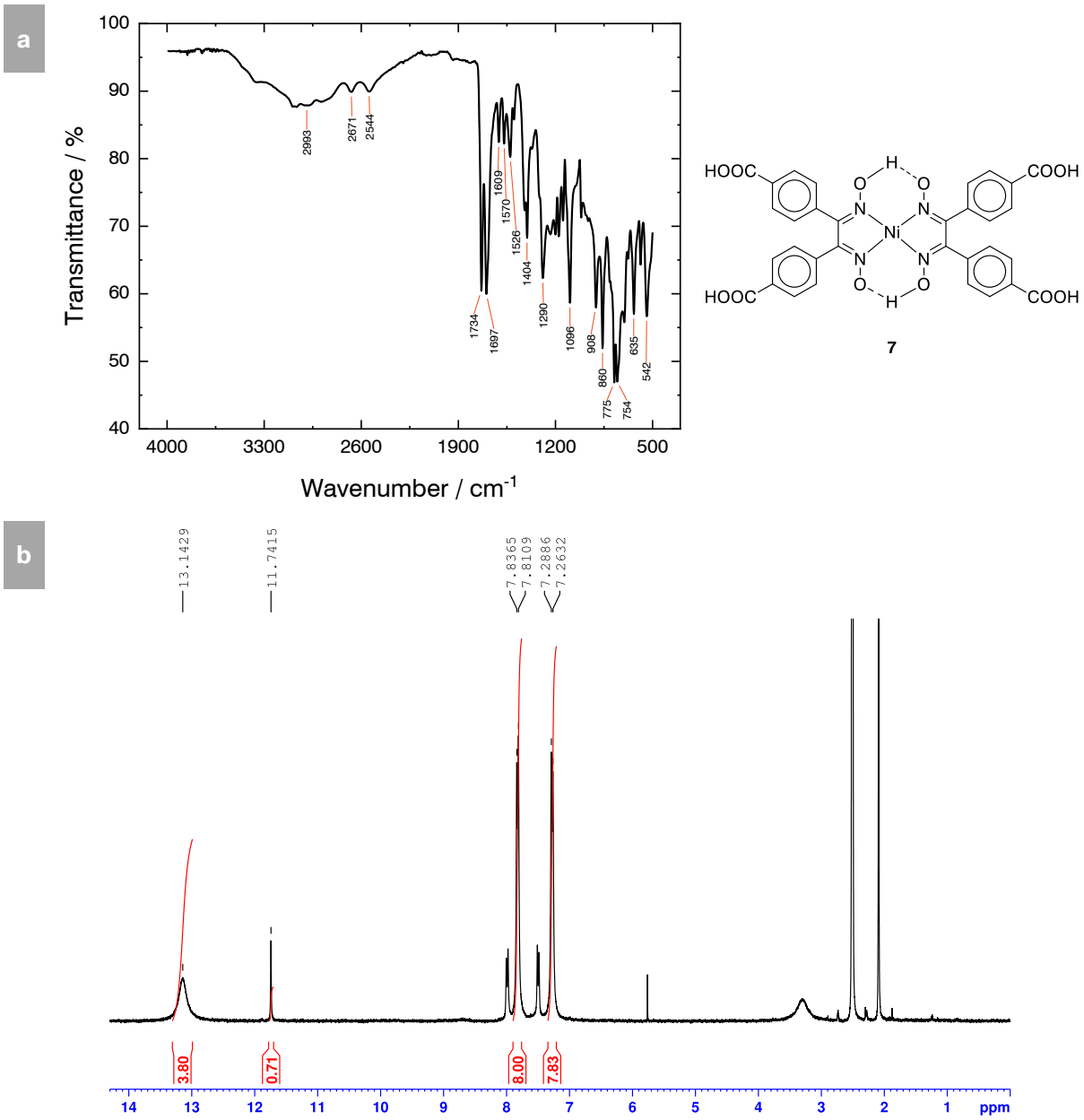

Figure 26. Spectroscopic characterisation of **7**. **a)** IR spectrum acquired from the solid sample in the ATR-mode. Inserts in cm^{-1}. **b)** ^{1}H-NMR recorded in DMSO-d_6 (300 MHz, 298 K).

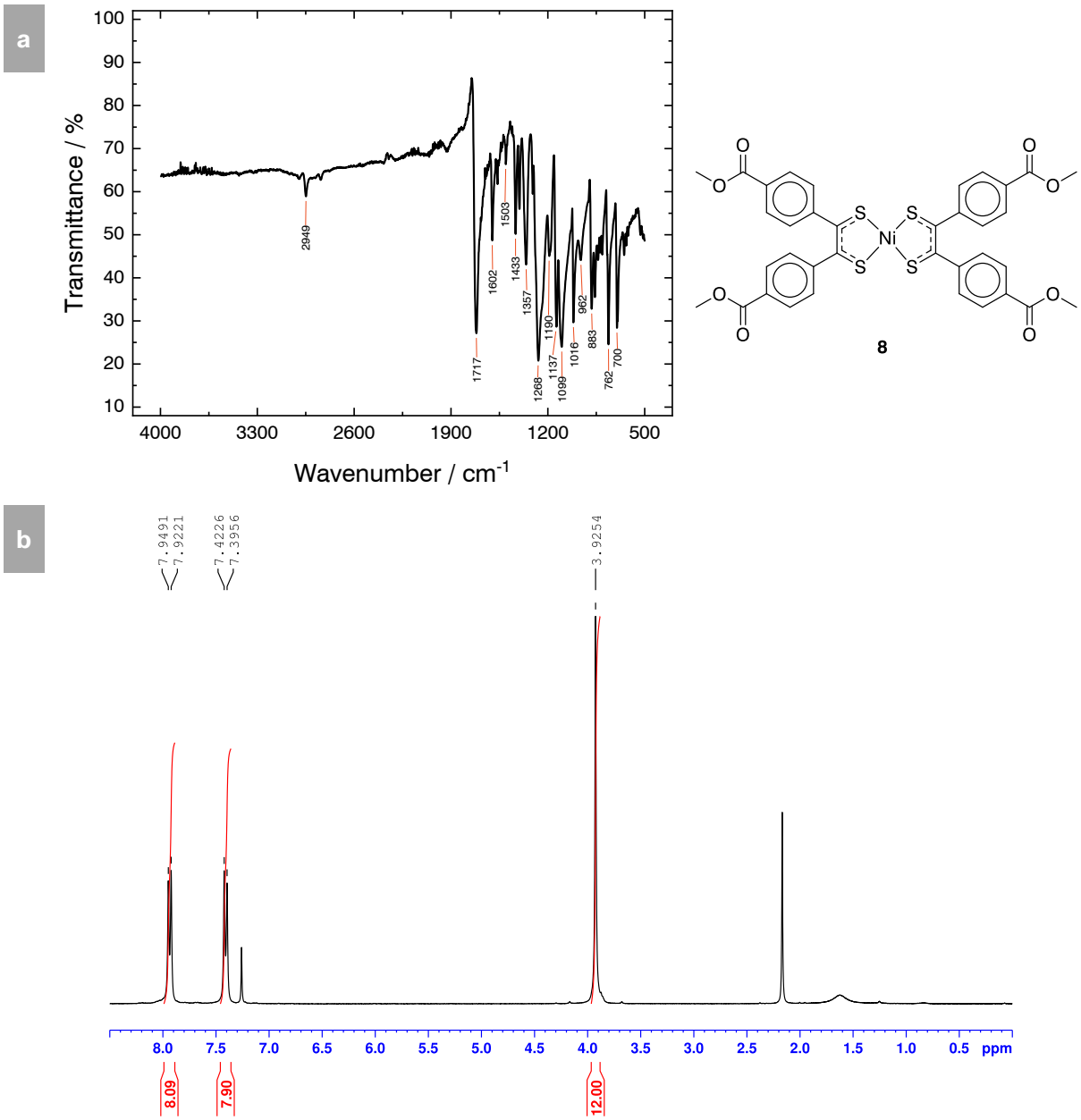

Figure 27. Spectroscopic characterisation of **8**. **a)** IR spectrum acquired from the solid sample in the ATR-mode. Inserts in cm^{-1}. **b)** ^{1}H-NMR recorded in $CDCl_3$ (300 MHz, 298 K).

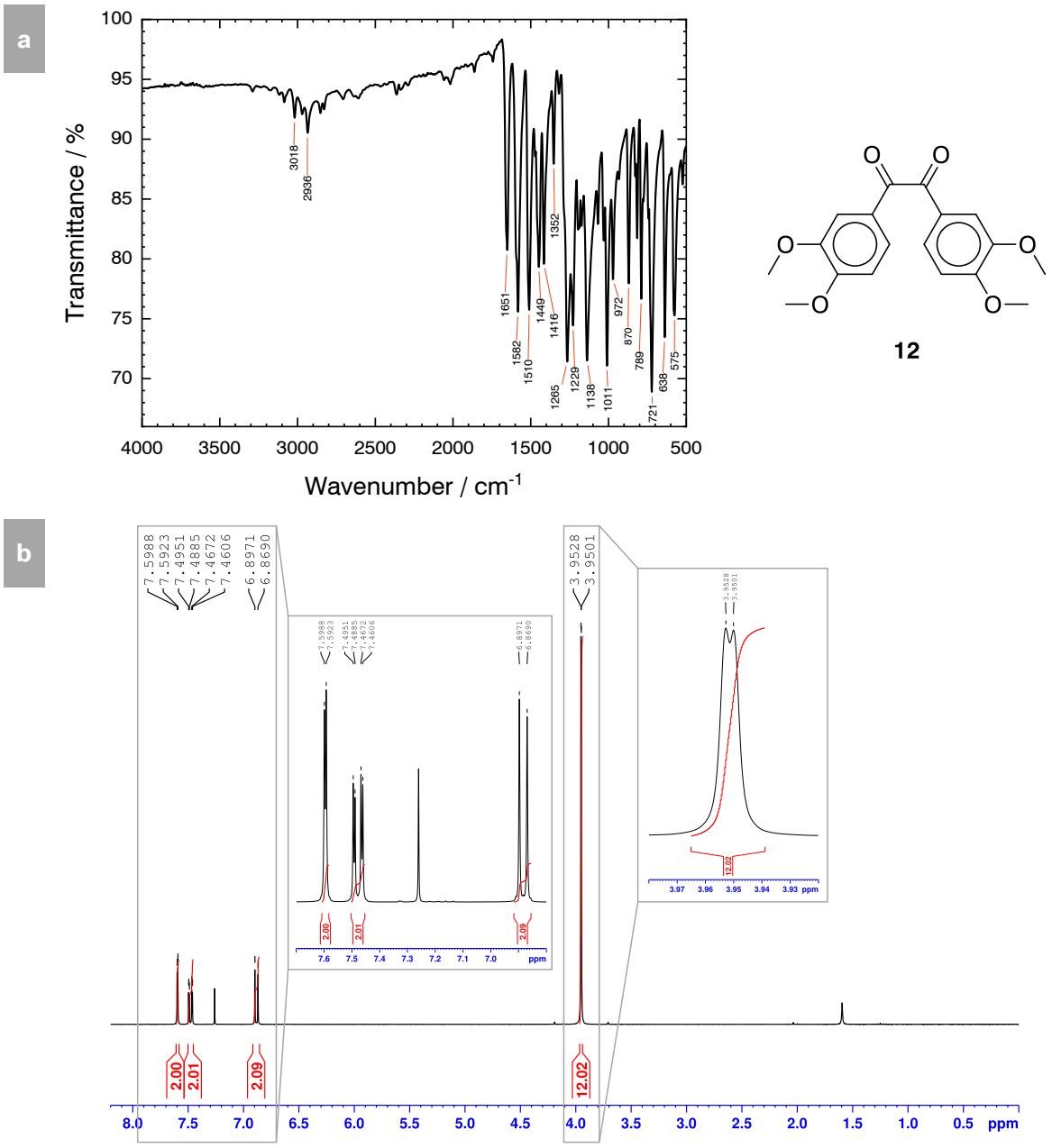

Figure 28. Spectroscopic characterisation of **12**. **a)** IR spectrum acquired from the solid sample in the ATR-mode. Inserts in cm^{-1}. **b)** ^{1}H-NMR recorded in $CDCl_3$ (300 MHz, 298 K).

References

[1] W. S. Broecker, "Climatic change: are we on the brink of a pronounced global warming?", *Science* **1975**, *189*(4201), 460 – 463.

[2] H. Lee, et al., "*IPCC, 2023: Climate Change 2023: Synthesis Report. Contribution of Working Groups I, II and III to the Sixth Assessment Report of the Intergovernmental Panel on Climate Change [Core Writing Team, H. Lee and J. Romero (eds.)]. IPCC, Geneva, Switzerland*, Intergovernmental Panel on Climate Change (IPCC) **2023**.

[3] G. Feulner, "Global Challenges: Climate Change", *Global challenges* **2017**, *1*(1), 5 – 6.

[4] S. Arrhenius, "On the Influence of Carbonic Acid in the Air upon the Temperature of the Ground", *Philos. Mag.* **1896**, *41*(5), 237 – 276.

[5] G. S. Callendar, "The artificial production of carbon dioxide and its influence on temperature", *Quart. J. Royal Meteoro. Soc.* **1938**, *64*(275), 223 – 240.

[6] T. R. Anderson, E. Hawkins, P. D. Jones, "CO2, the greenhouse effect and global warming: from the pioneering work of Arrhenius and Callendar to today's Earth System Models", *Endeavour* **2016**, *40*(3), 178 – 187.

[7] A. D. Chandler, "Industrial Revolutions and Institutional Arrangements", *Bulletin of the American Academy of Arts and Sciences* **1980**, *33*(8), 33 – 50.

[8] A. Fernihough, K. H. O'Rourke, "Coal and the European Industrial Revolution", *The Economic Journal* **2021**, *131*(635), 1135 – 1149.

[9] British Petroleum BP p.l.c., "*bp Statistical Review of World Energy 2021*, 70th ed., London **2021**.

[10] IEA, "*Electricity 2024- Analysis and forecast to 2026* **2024**.

[11] W. Wang, B. Yuan, Q. Sun, R. Wennersten, "Application of energy storage in integrated energy systems – A solution to fluctuation and uncertainty of renewable energy", *Journal of Energy Storage* **2022**, *52*, 104812.

[12] O. Smith, O. Cattell, E. Farcot, R. D. O'Dea, K. I. Hopcraft, "The effect of renewable energy incorporation on power grid stability and resilience", *Sci. Adv.* **2022**, *8*(9), eabj6734.

[13] W.-P. Schill, "Electricity Storage and the Renewable Energy Transition", *Joule* **2020**, *4*(10), 2059 – 2064.

[14] D. G. Jefferies, "Pumped storage: *Proceedings of the conference organized by the Institution of Civil Engineers at Imperial College of Science, Technology and Medicine, London on 2-4 April 1990*, 1st ed. (Eds: T. H. Douglas), Thomas Telford, London **1990**.

[15] L. Peng, D. L. Mauzerall, Y. D. Zhong, G. He, "Heterogeneous effects of battery storage deployment strategies on decarbonization of provincial power systems in China", *Nat. commun.* **2023**, *14*(1), 4858.

[16] M. Arbabzadeh, R. Sioshansi, J. X. Johnson, G. A. Keoleian, "The role of energy storage in deep decarbonization of electricity production", *Nat. commun.* **2019**, *10*(1), 3413.

[17] B. Dunn, H. Kamath, J.-M. Tarascon, "Electrical energy storage for the grid: a battery of choices", *Science* **2011**, *334*(6058), 928 – 935.

[18] M. R. Lukatskaya, B. Dunn, Y. Gogotsi, "Multidimensional materials and device architectures for future hybrid energy storage", *Nat. commun.* **2016**, *7*, 12647.

[19] S. P. S. Badwal, S. S. Giddey, C. Munnings, A. I. Bhatt, A. F. Hollenkamp, "Emerging electrochemical energy conversion and storage technologies", *Front. Chem.* **2014**, *2*, 79.

[20] B. You, Y. Sun, "Innovative Strategies for Electrocatalytic Water Splitting", *Acc. Chem. Res.* **2018**, *51*(7), 1571 – 1580.

[21] S. Anantharaj, S. Pitchaimuthu, S. Noda, "A review on recent developments in electrochemical hydrogen peroxide synthesis with a critical assessment of perspectives and strategies", *Adv. Colloid Interface Sci.* **2021**, *287*, 102331.

[22] A. Devlin, J. Kossen, H. Goldie-Jones, A. Yang, "Global green hydrogen-based steel opportunities surrounding high quality renewable energy and iron ore deposits", *Nat. commun.* **2023**, *14*(1), 2578.

[23] D. R. Nhuchhen, S. P. Sit, D. B. Layzell, "Decarbonization of cement production in a hydrogen economy", *Appl. Energy* **2022**, *317*, 119180.

[24] G. Goor, J. Glenneberg, S. Jacobi, J. Dadabhoy, E. Candido, "Ullmann's Encyclopedia of Industrial Chemistry: *Hydrogen Peroxide*, Vol. 8, Wiley, Weinheim **2000**.

[25] G. Qing, R. Ghazfar, S. T. Jackowski, F. Habibzadeh, M. M. Ashtiani, C.-P. Chen, M. R. Smith, T. W. Hamann, "Recent Advances and Challenges of Electrocatalytic N2 Reduction to Ammonia", *Chem. Rev.* **2020**, *120*(12), 5437 – 5516.

[26] M. Rahimi, A. Khurram, T. A. Hatton, B. Gallant, "Electrochemical carbon capture processes for mitigation of CO2 emissions", *Chem. Soc. Rev.* **2022**, *51*(20), 8676 – 8695.

[27] K. Shi, B. Guan, Z. Zhuang, J. Chen, Y. Chen, Z. Ma, C. Zhu, X. Hu, S. Zhao, H. Dang, J. Guo, L. Chen, K. Shu, Y. Li, Z. Guo, C. Yi, J. Hu, Z. Huang, "Perspectives and Outlook of E-fuels: Production, Cost Effectiveness, and Applications", *Energy Fuels* **2024**, *38*(9), 7665 – 7692.

[28] https://solid-state-chemistry-energy-lab.org/electrocatalysis/ (Accessed on June 10, 2024).

[29] G. Wittstock, "*Lehrbuch der Elektrochemie*", 12 - Elektrokatalyse, 1st ed., Wiley-VCH, Weinheim **2023**.

[30] K. Jackowska, P. Krysinski, "*Applied Electrochemistry*", 4 - Electrocatalysis, 1st ed., Walter de Gruyter, Berlin/Boston **2020**.

[31] G. Horányi, "Heterogeneous catalysis and electrocatalysis", *Catal. Today* **1994**, *19*(2), 285 – 311.

[32] J. Hagen, "*Industrial Catalysis*: *A Practical Approach*", Chapter 10 - Electrocatalytic Processes, 3rd ed., Wiley-VCH, Weinheim **2015**.

[33] H. Zhang, Q. Liang, K. Xie, "How to rationally design homogeneous catalysts for efficient CO2 electroreduction?", *iScience* **2024**, *27*(2), 108973.

[34] C. Yang, Y. Wang, L. Qian, A. M. Al-Enizi, L. Zhang, G. Zheng, "Heterogeneous Electrocatalysts for CO 2 Reduction", *ACS Appl. Energy Mater.* **2021**, *4*(2), 1034 – 1044.

[35] W. Grünert, W. Kleist, M. Muhler, "*Catalysis at Surfaces*", 4.9 - Structure and performance in electrocatalysis, 1st ed., Walter de Gruyter, Berlin/Boston **2023**.

[36] J. Masa, C. Andronescu, W. Schuhmann, "Elektrokatalyse als Nexus für nachhaltige erneuerbare Energien – der gordische Knoten aus Aktivität, Stabilität und Selektivität", *Angew. Chem.* **2020**, *132*(36), 15410 – 15426.

[37] A. S. Bandarenka, E. Ventosa, A. Maljusch, J. Masa, W. Schuhmann, "Techniques and methodologies in modern electrocatalysis: evaluation of activity, selectivity and stability of catalytic materials", *Analyst* **2014**, *139*(6), 1274 – 1291.

[38] Q. Wang, D. Astruc, "State of the Art and Prospects in Metal-Organic Framework (MOF)-Based and MOF-Derived Nanocatalysis", *Chem. Rev.* **2020**, *120*(2), 1438 – 1511.

[39] A. E. Baumann, D. A. Burns, B. Liu, V. S. Thoi, "Metal-organic framework functionalization and design strategies for advanced electrochemical energy storage devices", *Commun Chem* **2019**, *2*(1).

[40] A. K. Cheetham, C. N. R. Rao, R. K. Feller, "Structural diversity and chemical trends in hybrid inorganic-organic framework materials", *Chem. Commun.* **2006**(46), 4780 – 4795.

[41] O. M. Yaghi, M. J. Kalmutzki, C. S. Diercks, "*Introduction to Reticular Chemistry*", 1 - Emergence of Metal-Organic Frameworks, 1st ed., Wiley-VCH, Weinheim **2019**.

[42] H. Li, M. Eddaoudi, M. O'Keeffe, O. M. Yaghi, "Design and synthesis of an exceptionally stable and highly porous metal-organic framework", *Nature* **1999**, *402*(6759), 276 – 279.

[43] S. S. Kaye, A. Dailly, O. M. Yaghi, J. R. Long, "Impact of preparation and handling on the hydrogen storage properties of Zn4O(1,4-benzenedicarboxylate)3 (MOF-5)", *J. Am. Chem. Soc.* **2007**, *129*(46), 14176 – 14177.

[44] L. S. Xie, G. Skorupskii, M. Dincă, "Electrically Conductive Metal-Organic Frameworks", *Chem. Rev.* **2020**, *120*(16), 8536 – 8580.

[45] D. Y. Heo, H. H. Do, S. H. Ahn, S. Y. Kim, "Metal-Organic Framework Materials for Perovskite Solar Cells", *Polymers* **2020**, *12*(9), 2061.

[46] L. Sun, M. G. Campbell, M. Dincă, "Elektrisch leitfähige poröse Metall-organische Gerüstverbindungen", *Angew. Chem.* **2016**, *128*(11), 3628 – 3642.

[47] C. Li, H. Zhang, M. Liu, F.-F. Lang, J. Pang, X.-H. Bu, "Recent progress in metal–organic frameworks (MOFs) for electrocatalysis", *Ind. Chem. Mater.* **2023**, *1*(1), 9 – 38.

[48] X. Huang, P. Sheng, Z. Tu, F. Zhang, J. Wang, H. Geng, Y. Zou, C.-A. Di, Y. Yi, Y. Sun, W. Xu, D. Zhu, "A two-dimensional π-d conjugated coordination polymer with extremely high electrical conductivity and ambipolar transport behaviour", *Nat. commun.* **2015**, *6*, 7408.

[49] C. Li, L. Zhang, J. Chen, X. Li, J. Sun, J. Zhu, X. Wang, Y. Fu, "Recent development and applications of electrical conductive MOFs", *Nanoscale* **2021**, *13*(2), 485 – 509.

[50] Y. Zhou, S. Liu, Y. Gu, G.-H. Wen, J. Ma, J.-L. Zuo, M. Ding, "In(III) Metal-Organic Framework Incorporated with Enzyme-Mimicking Nickel Bis(dithiolene) Ligand for Highly Selective CO2 Electroreduction", *J. Am. Chem. Soc.* **2021**, *143*(35), 14071 – 14076.

[51] S. Roy, Z. Huang, A. Bhunia, A. Castner, A. K. Gupta, X. Zou, S. Ott, "Electrocatalytic Hydrogen Evolution from a Cobaloxime-Based Metal-Organic Framework Thin Film", *J. Am. Chem. Soc.* **2019**, *141*(40), 15942 – 15950.

[52] S. S. Park, E. R. Hontz, L. Sun, C. H. Hendon, A. Walsh, T. van Voorhis, M. Dincă, "Cation-dependent intrinsic electrical conductivity in isostructural tetrathiafulvalene-based microporous metal-organic frameworks", *J. Am. Chem. Soc.* **2015**, *137*(5), 1774 – 1777.

[53] L. S. Xie, S. S. Park, M. J. Chmielewski, H. Liu, R. A. Kharod, L. Yang, M. G. Campbell, M. Dincă, "Isoreticular Linker Substitution in Conductive Metal-Organic Frameworks with Through-Space Transport Pathways", *Angew. Chem. Int. Ed.* **2020**, *59*(44), 19623 – 19626.

[54] J. W. Verhoeven, "Glossary of terms used in photochemistry (IUPAC Recommendations 1996)", *Pure Appl. Chem.* **1996**, *68*(12), 2223 – 2286.

[55] B. Guo, F. Li, C. Wang, L. Zhang, D. Sun, "A rare (3,12)-connected zirconium metal–organic framework with efficient iodine adsorption capacity and pH sensing", *J. Mater. Chem. A* **2019**, *7*(21), 13173 – 13179.

[56] M. H. Petersen, S. A. Gevorgyan, F. C. Krebs, "Thermocleavable Low Band Gap Polymers and Solar Cells Therefrom with Remarkable Stability toward Oxygen", *Macromolecules* **2008**, *41*(23), 8986 – 8994.

[57] J. Chen, J. Yang, Y. Chen, J. Dong, R. Deng, L. Zhu, "Multiwalled carbon nanotubes modified with nickel-zinc bis(dithiolene) metal-organic frameworks for electrochemical detection of 5-hydroxytryptamine", *J. Electroanal. Chem.* **2023**, *949*, 117851.

[58] M. Ichihara, H. Suzuki, B. Mohr, K. Ohta, "Different disk structures in the hexagonal columnar mesophases of 2,3-dicyano-6,7,10,11-tetraalkoxy-1,4-diazatriphenylenes and 2,3-dicyano-6,7,10,11-tetraalkoxytriphenylenes", *Liq. Cryst.* **2007**, *34*(3), 401 – 410.

[59] K. Ohta, H. Hasebe, H. Ema, M. Moriya, T. Fujimoto, I. Yamamoto, "Discotic Liquid Crystals of Transition Metal Complexes 11 1 The First π-Acceptor in Discotic Columnar Liquid Crystals Obtained from Octasubstituted Bis(diphenylethane-1,2-dithiolene)nickel Complexes", *Mol. Cryst. Liq. Cryst.* **1991**, *208*(1), 21 – 32.

[60] D. H. Apaydin, H. Seelajaroen, O. Pengsakul, P. Thamyongkit, N. S. Sariciftci, J. Kunze-Liebhäuser, E. Portenkirchner, "Photoelectrocatalytic Synthesis of Hydrogen Peroxide by Molecular Copper-Porphyrin Supported on Titanium Dioxide Nanotubes", *ChemCatChem* **2018**, *10*(8), 1793 – 1797.

[61] F. Wöhler, J. Liebig, "Untersuchungen über das Radikal der Benzoesäure", *Ann. Pharm.* **1832**, *3*(3), 249 – 282.

[62] T. Ugai, R. Tanaka, T. Dokawa, "A new catalyst for acyloin condensation", *J. Pharm. Soc. Japan* **1943**, *63*, 296 – 300.

[63] W. S. Ide, J. S. Buck, "The Synthesis of Benzoins, In: *Organic Reactions*, Vol. 4, 1st ed. (Eds: R. Adams) **1948**.

[64] P. Depreux, G. Bethegnies, A. Marcincal-Lefebvre, "Synthesis of benzil from benzoin with copper(II) acetate", *J. Chem. Educ.* **1988**, *65*(6), 553.

[65] H. T. Clarke, E. E. Dreger, "Benzil", *Org. Synth.* **1926**, *6*, 6.

[66] J. Clayden, N. Greeves, S. Warren, "*Organic Chemistry*", Chapter 36 - Participation, rearrangement and fragmentation, 2nd ed., Oxford University Press, Oxford **2012**.

[67] J. Ritz, H. Fuchs, H. G. Perryman, "*Ullmann's Encyclopedia of Industrial Chemistry*: *Hydroxylamine*, 1st ed., Wiley, Weinheim **2000**.

[68] H.-J. Meyer, C. Janiak, D. Gudat, C. Schulze, "*Riedel - Moderne Anorganische Chemie*", 3.9.2 Kristallfeldtheorie (CF-Therorie), 6th ed., Walter de Gruyter, Berlin/Boston **2023**.

[69] C. L. I. Bertini", *Coord. Chem. Rev.* **1996**, *150*, 1 – 28.

[70] M. Lehr, T. Paschelke, E. Trumpf, A.-M. Vogt, C. Näther, F. D. Sönnichsen, A. J. McConnell, "Ein Methodenrepertoire für die paramagnetische NMR-Spektroskopie zur Charakterisierung von paramagnetischen/Spin-Crossover- Komplexen und Metall-organischen Käfigverbindungen", *Angew. Chem.* **2020**, *132*(43), 19508 – 19516.

[71] Q. Miao, J. Gao, Z. Wang, H. Yu, Y. Luo, T. Ma, "Syntheses and characterization of several nickel bis(dithiolene) complexes with strong and broad Near-IR absorption", *Inorg. Chim. Acta* **2011**, *376*(1), 619 – 627.

[72] N. B. Colthup, L. H. Daly, S. E. Wiberley, "*Introduction to Infrared and Raman Spectroscopy*, 1st ed., Academic Press, Inc., New York **1975**.

[73] D. C. Harris, M. D. Bertolucci, "*Symmetry and Spectroscopy*: *An Introduction to Vibrational and Electronic Spectroscopy*", 3-11. Functional Group Analysis, 1st ed., Oxford University Press, New York **1978**.

[74] N. B. Colthup, "Spectra-Structure Correlations in the Infra-Red Region", *J. Opt. Soc. Am.* **1950**, *40*(6), 397 – 400.

[75] B. C. Smith, "Alcohols - The Rest of the Story", *Spectroscopy* **2017**, *32*(4), 19 – 23.

[76] B. C. Smith, "The Carbonyl Group, Part I: Introduction", *Spectroscopy* **2017**, *32*(9), 31 – 36.

[77] Y. Zhou, Q. Hu, F. Yu, G.-Y. Ran, H.-Y. Wang, N. D. Shepherd, D. M. D'Alessandro, M. Kurmoo, J.-L. Zuo, "A Metal-Organic Framework Based on a Nickel Bis(dithiolene) Connector: Synthesis, Crystal Structure, and Application as an Electrochemical Glucose Sensor", *J. Am. Chem. Soc.* **2020**, *142*(48), 20313 – 20317.

[78] G. N. Schrauzer, V. P. Mayweg, "Preparation, Reactions, and Structure of Bisdithio-α-diketone Complexes of Nickel, Palladium, and Platinum", *J. Am. Chem. Soc.* **1965**, *87*(7), 1483 – 1489.

[79] A. Olubummo, L. Zhao, A. Hartman, H. Tom, Y. Zhao, K. Wycoff, "Photothermal bleaching of nickel dithiolene for bright multi-colored 3D printed parts", *Nat. commun.* **2023**, *14*(1), 586.

[80] J. Li, B. Deng, J. Ye, "Fluorescence-free bis(dithiolene)nickel dyes for surface-enhanced resonance Raman imaging in the second near-infrared window", *Biomaterials* **2023**, *300*, 122211.

[81] Y. Liu, Z. Zhang, X. Chen, S. Xu, S. Cao, "Near-infrared absorbing dyes at 1064 nm: Soluble dithiolene nickel complexes with alkylated electron-donating groups as Peripheral substituents", *Dyes Pigm.* **2016**, *128*, 179 – 189.

[82] B. Park, K. M. Lee, S. Park, M. Yun, H.-J. Choi, J. Kim, C. Lee, H. Kim, C. Kim, "Deep tissue photoacoustic imaging of nickel(II) dithiolene-containing polymeric nanoparticles in the second near-infrared window", *Theranostics* **2020**, *10*(6), 2509 – 2521.

[83] K. Mebrouk, M. Ciancone, T. Vives, S. Cammas-Marion, T. Benvegnu, C. Le Goff-Gaillard, Y. Arlot-Bonnemains, M. Fourmigué, F. Camerel, "Fine and Clean Photothermally Controlled NIR Drug Delivery from Biocompatible Nickel-bis(dithiolene)-Containing Liposomes", *ChemMedChem* **2017**, *12*(21), 1753 – 1758.

[84] M. Ciancone, K. Mebrouk, N. Bellec, C. Le Goff-Gaillard, Y. Arlot-Bonnemains, T. Benvegnu, M. Fourmigué, F. Camerel, S. Cammas-Marion, "Biocompatible nanoparticles containing hydrophobic nickel-bis(dithiolene) complexes for NIR-mediated doxorubicin release and photothermal therapy", *J. Mater. Chem. B* **2018**, *6*(12), 1744 – 1753.

[85] T.-T. Bui, O. Thiebaut, E. Grelet, M.-F. Achard, B. Garreau-de Bonneval, K. I. Moineau-Chane Ching, "Discotic Nickel Bis(dithiolene) Complexes – Synthesis, Optoelectrochemical and Mesomorphic Properties", *Eur. J. Inorg. Chem.* **2011**, *2011*(17), 2663 – 2676.

[86] I. A. Pearl, H. B. Faber Jr., W. C. Holman, "Reactions of Vanillin and Its Derived Compounds. XXIX. 3,3',4,4'-Tetrahydroxybenzil and Its Reduction", *J. Org. Chem.* **1960**, *25*(8), 1449 – 1450.

[87] A. Wollrab, "*Organische Chemie*: *Eine Einführung für Lehramts- und Nebenfachstudenten*", Chapter 11.5.3 - Die Oxidation von Phenolen, 4th ed., Springer-Verlag, Berlin, Heidelberg **2014**.

[88] M. A. Rahim, S. Matsumura, K. Toshima, "Deprotection of benzyl ethers using 2,3-dichloro-5,6-dicyano-p-benzoquinone (DDQ) under photoirradiation", *Tetrahedron Lett.* **2005**, *46*(43), 7307 – 7309.

[89] J. Quick, J. K. Crelling, "The acetyl function as a protecting group for phenols", *J. Org. Chem.* **1978**, *43*(1), 155 – 156.

[90] M. P. Rayaroth, G. Boczkaj, O. Aubry, U. K. Aravind, C. T. Aravindakumar, "Advanced Oxidation Processes for Degradation of Water Pollutants – Ambivalent Impact of Carbonate Species: A Review", *Water* **2023**, *15*(8), 1615.

[91] N. Elgrishi, K. J. Rountree, B. D. McCarthy, E. S. Rountree, T. T. Eisenhart, J. L. Dempsey, "A Practical Beginner's Guide to Cyclic Voltammetry", *J. Chem. Educ.* **2018**, *95*(2), 197 – 206.

[92] X. Zhang, K. Wan, P. Subramanian, M. Xu, J. Luo, J. Fransaer, "Electrochemical deposition of metal–organic framework films and their applications", *J. Mater. Chem. A* **2020**, *8*(16), 7569 – 7587.

[93] N. Campagnol, T. R. C. van Assche, M. Li, L. Stappers, M. Dincă, J. F. M. Denayer, K. Binnemans, D. E. de Vos, J. Fransaer, "On the electrochemical deposition of metal–organic frameworks", *J. Mater. Chem. A* **2016**, *4*(10), 3914 – 3925.

[94] R. K. Parashar, P. Jash, M. Zharnikov, P. C. Mondal, "Metal-organic Frameworks in Semiconductor Devices", *Angew. Chem. Int. Ed.* **2024**, *63*(15), e202317413.

[95] F. Wudl, M. R. Bryce, "Apparatus for two-probe conductivity measurements on compressed powders", *J. Chem. Educ.* **1990**, *67*(8), 717.

[96] A. Bismuto, P. Finkelstein, P. Müller, B. Morandi, "The Journey of Ni(I) Chemistry", *Helv. Chim. Acta* **2021**, *104*(12).

[97] K. S. Johnson, "Manganese redox chemistry revisited", *Science* **2006**, *313*(5795), 1896 – 1897.

[98] Y. Wang, B. Quillian, P. Wei, H. Wang, X.-J. Yang, Y. Xie, R. B. King, P. v. R. Schleyer, H. F. Schaefer, G. H. Robinson, "On the chemistry of Zn-Zn bonds, RZn-ZnR (R = {(2,6-Pri2C6H3)N(Me)C}2CH): synthesis, structure, and computations", *J. Am. Chem. Soc.* **2005**, *127*(34), 11944 – 11945.